Photonic applications based on the use of structured light

Carmelo G. Rosales Guzmán

Under the supervision of

Professor Juan P. Torres

A dissertation submitted in partial fulfillment of the requirements for the degree of

Doctor of Philosophy

ICFO - The Institute of Photonic Sciences
February 2015
Barcelona, Spain

ACKNOWLEDGMENTS

It is a pleasure to thank those who supported me along this journey. First of all I would like to thank Professor Juan P. Torres for giving me the opportunity to join his group and for all of his help and support throughout mi PhD. Professor Torres assisted me wisely in many ways, his passion for research, his dedication and deep involvement in every project has inspired me as a future scientist. It is also an honor to thank Professor Aniceto Belmonte from Universitat Politècnica de Catalunya with whom we actively collaborated and who advised in many aspects. My gratitude extend to former and current members of the Quantum Engineering of Light group, specially to Adam Vallés and Luis José Salazar for useful advice.

I would also like to show my gratitude to all ICFO's non-scientific members. Management, Administration, human resources & education, etc. do an amazing work to make every day easier. The combination of all ICFO members have created an encouraging and supporting place to pursue a scientific career.

I am heartily thankful to my parents Abel L. Rosales and Florentina Guzmán, as well as my brothers Miguel, Jesús and Martha who have always encouraged me to succeed. I owe my deepest gratitude to Valeria Rodríguez who has played an essential role during this four years of hard work. Last but not least, I offer my regards to all of those who supported me in any respect during the completion of my PhD.

Abstract

Structured light beams, this is, beams whose phase changes from point to point in the transverse plane, provides with an alternative tool to search for new applications, or simply to expand the capabilities of current applications where commonly used light beams have encountered physical limitations. Applications can be found not only in the field of optics but also in areas as diverse as astrophysics, telecommunications and quantum computing, to mention some. In this thesis we put forward three new applications in which the use of structured light beams plays a crucial role.

An exotic property on some beams is their ability to auto reconstruct upon propagation, when part of their intensity has been blocked. In this way, the first contribution we report in this thesis is the experimental observantion that Helico-conical beams self-heal. This beams were recently discovered and have gained special interest because their ability to trap and guide micro-particles along helicoidal trajectories. Our experiments are supported by numerical simulations suggesting the energy transport is responsible for the self reconstruction.

In the field of optical remote sensing, the Doppler effect is widely used to measure the component of the velocity along the line of sight, *i.e.*, the longitudinal component. The Doppler effect alone, does not allow to measure the transverse component. In this context, structured light beams provides with a tool that makes this possible: its structured phase. The main idea resides in the fact that this beams, reflected from transversally moving targets, are frequency shifted proportional to the velocity of the target. The information of the velocity can be extracted using interferometric methods, in a similar way to the longitudinal Doppler shift. In a first experiment we validated this theoretical concept for two particular cases: rotation and longitudinal motions along the transverse plane of illumination. The way in which we extract the velocity information does not enable to determine the direction on motion. Hence, we proposed a novel technique to overcome this drawback, which was demonstrated in a second experiment. This technique comprises the use of a structured light beam in which the phase is modulated in time. Finally, in a first attempt to demonstrate a system capable to measure the velocity components involved in a full 3-dimensional motion, we emulated experimentally a helical motion. By illuminating in a synchronised way with a Gaussian and a Laguerre-Gaussian beam, we were able to extract both velocity components: rotational and translational.

Some current existing techniques to measure small layer thicknesses are based on the use of common-pant interferometers. In particular the self-referencing type, in which both the reference and the signal beams are generated locally. A reflective surface is engineered in the form of a ridge or cliff, in such a way when illuminated with a Gaussian beam half of it is reflected from the top and the other half from the base. This two “new beams" acquire a phase difference that depends on the height of the ridge and the wavelength of the illuminating source. This phase variations are detected on-axis in the far filed as intensity changes. Hence, if we place a thick layer on top of the ridge, the change in intensity will immediately yield the height of the layer. This scheme becomes highly sensitive to small phase variations when the height of the ridge is $1/8$ of the wavelength, known as the quadrature condition. This restriction might unfortunately limit the use of this technique to specific cases, since

it highly depends on the construction of the ridge. To overcome this drawback we proposed and demonstrated experimentally a technique in which the quadrature condition is not needed a priori. Our approach is based on the use of spatial mode projection. For its implementation, we project the light reflected from the sample onto appropriately tailored spatial modes. The selection of mode depends on the geometry of the sample and can be efficiently made with diverse optical devices, such as computer-generated holograms in spatial light modulators (SLMs). In this way, the quadrature condition is passed onto the mode projection. With this technique, we were able to measured layer thicknesses as low as 9.7 nm.

Finally, we investigated theoretically the role that light endowed with Orbital Angular Momentum (OAM) might play for the discrimination of chiral molecules. Traditionally, this discrimination has been always related to Circularly Polarized Light (CPL), this is, to the Spin angular momentum of light. In this approach, the chiral response of molecules only depends on the properties of the same, and in many cases is very small. An approach to enhance this response was proposed very recently, in which the electromagnetic field that illuminates the molecule is properly tailored, in such a way the chiral response depends on both the molecular properties and the electromagnetic field. These types of electromagnetic fields have been termed "chiral fields" and are characterised through a quantity known as optical chirality (denoted as C). This quantity measures how contorted is the field at each point in space, the higher the value of C, the higher the chiral response. In our approach, we started from exact solutions to the Helmholtz equation. The high-order Bessel beams, characterised by a phase term $\exp[-i\ell\phi]$ that provides these beams with a well defined amount OAM. Where ϕ is the azimuthal angle of the cylindrical coordinates and ℓ is an integer number related to the OAM contained in the beam. In particular, the cases $\ell = 1$ and $\ell = -1$ shows an opposite value of C and a chiral response, which is similar to CPL. We found that a proper superposition of this two beams produces an on-axis, enhanced chiral response that can be several times larger compared to CPL.

Resumen

Los haces estructurados, es decir, haces cuya fase difiere de un punto a otro en el plano transversal, representan una herramienta alternativa para buscar nuevas aplicaciones, o simplemente para expandir las capacidades de las aplicaciones existentes en donde los haces comúnmente utilizados han encontrado limitaciones físicas. En la actualidad podemos encontrar encontrar aplicaciones no solo en el campo de la óptica sino ambién en áreas tan diversa como astrofísica, telecomunicaciones y computación cuántica por mencionar algunas. En esta tesis, introducimos tres nuevas aplicaciones, en las cuales el uso the haces estructurados juega un papel crucial.

Una propiedad exótica de un conjunto especifico de haces es su habilidad para reconstruirse así mismos al propagarse, cuando parte de su intensidad ha sido bloqueada. De esta forma, la primera contribución que reportamos es la demostración experimental de que los haces heli-conicos son capaces de auto-recostruirse. Estos haces fueron descubiertos recientemente y son de especial interés debido a su habilidad the atrapar y guiar micropartículas a lo largo de trayectorias helicoidales. Nuestros experimentos estan reforzados con simulaciones numéricas que sugieren como responsable de la auto-reconsrucción al transporte de energía.

In el campo de sensado remoto, el efecto Doppler es utilizado ampliamente para medir la componente de la velocidad a lo largo de la linea de visión, es decir, la componente longitudinal. El efecto Doppler por si solo, no permite medir la componente transversal. En este contexto, los haces estructurados proveen con una herramienta, su phase estructurada, mediante la cual se puede medir esta componente. La idea principal reside en el hecho de que la frecuencia de estos haces, cuando son reflejados de un objeto que se mueve trasversalmente, cambia de forma proporcional a la velocidad del objeto. La información de la velocidad puedes ser extraída utilizando métodos interferométricos, de forma similar al efecto Doppler longitudinal. En un primer experimento validamos este concepto teórico para dos casos particulares: rotación y translación longitudinal en el plano transversal al de iluminación. La forma en la que extraemos la información de la velocidad no permite determinar la dirección del movimiento. De esta forma, propusimos y demostramos experimentalmente una nueva técnica que permite determinar la dircción de movimiento. Esta técnica involucra el uso de un haz estructurado en el cual la fase es modulada temporalmente. Finalmente, en un primera propuesta por demostrar un sistema capaz de medir ambas componentes de la velocidad de un movimiento tridimensional, emulamos un movimiento helicoidal. Iluminado sincronizadamente con dos haces un Gaussiano y un Laguerre-Gauss, obtuvimos ambas componentes de la velocidad: rotación y traslación.

Algunas de las técnicas que existen actualmente para medir grosores están basadas en el uso de interferómetros de camino óptico común. En particular los autoreferenciados, en los cuales tanto el haz de referencia como el que lleva la información son generados localmente. Una superficie reflectante con forma de acantilado es diseñada, de tal forma que cuando es iluminada con un haz Gaussiano, una mitad es reflejada en la base y la otra en la cima. Estos dos “nuevos haces” adquieren una diferencia de fase que depende de la altura de del acantilado y de la longitud de onda del haz. Estas variaciones son detectadas en campo lejano a lo largo del eje de propagación como cambios

de intensidad. De esta forma, si colocamos una capa delgada sobre del acantilado, el cambio en la intensidad nos dará inmediatamente el grosor de la capa. Este esquema es muy sensible a cambios pequeños de fase cuando la altura del acantilado es $1/8$ de la longitud de onda, conocida como condición de cuadratura. Desafortunadamente, esta restricción puede limitar el uso de esta técnica a casos específicos, ya que depende en gran medida de la construcción apropiada del acantilado. Para solventar esta desventaja propusimos y demostramos experimentalmente una técnica en la cual la condición de cuadratura no es necesaria a priori. Nuestro metodo esta basado en la proyección espacial en modos. Para su implementación, proyectamos la luz reflejada por la muestra sobre modos espaciales diseñados apropiadamente. La selección de los modos depende de la geometría de la muestra y se puede llevar acabo eficientemente con varios dispositivos ópticos, como por ejemplo hologramas generados por computadora en moduladores espaciales de luz (SML, por sus siglas en ingles). De esta forma, la condición de cuadratura es codificada en la proyección de modos. Esta técnica nos permite medir grosores en el orden de 9.7 nm.

Finalmente, investigamos teóricamante el papel que los haces provistos con momento angular orbital (OAM por sus siglas en ingles) pueden desempeñar en la discriminacińon de moléculas quirales. Tradicionalmente, esta discriminación ha estado asociada a la luz circularmente polarizada (CPL por sus siglas en ingles), es decir, al momento angular espinorial. En esta aproximación, la respuesta chiral de las moléculas depende únicamente de las propiedades de la misma, que en muchos casos es muy pequeña. Una aproximación para incrementar esta respuesta conciste en el diseño apropiado del campo electromagnético que ilumina las moléculas, de esta forma la respuesta quiral depende no solo de las propiedades de la molécula sino también del campo electromagnético. Este tipo de campos electromagnéticos han sido denominados “campos quirales”, caracterizados mediante una cantidad conocida como quiralidad óptica (denotada con C). Esta cantidad mide cuan contorsionado esta el campo electromagnético en cada punto del espacio, cuan mayor sea C, mayor será la respuesta quiral. Nosotros abordamos el problema utilizando soluciones exactas a la ecuación de Helmholtz. Los haces Bessel de orden superior, caracterizados por una término de fase $\exp[-i\ell\phi]$ que provee a estos haces con una cantidad de OAM bien definid. En donde ϕ es el ángulo azimutal de las coordenadas cilíndricas y ℓ es un número entero relacionado a la cantidad de OAM contenida en el haz. En particular, los casos $\ell = 1$ and $\ell = -1$ muestran un valor de C opuesto y una respuesta quiral, que es muy similar a la de CPL. Más aún, descubrimos que una superposición adecuada de estos dos modos produce una respuesta quiral, a lo largo del eje de propagación, que puede ser varias veces mayor comparada con CPL.

Contents

1 Introduction **1**

References 5

2 The Angular Momentum of Light **9**

2.1 The Helmholtz equation 10

2.1.1 The vectorial Helmholtz equation 10

2.1.2 The paraxial wave equation 11

2.2 Solutions to the paraxial wave equation 13

2.2.1 Solutions in Cartesian coordinates 13

2.2.2 Solutions in cylindrical coordinates 15

2.3 Angular momentum of Light 19

2.3.1 Historical introduction 19

2.3.2 Mathematical description 20

2.4 Generation of structured light beams 24

2.4.1 Intracavity generation 24

2.4.2 Extracavity generation 25

References 30

3 A new type of self-healing beams **33**

3.1 Self-healing beams 33

3.1.1 Airy beams 34

3.1.2 Petal-like beams 34

3.1.3 Pearcy beams 35

3.2 Helico-conical Beams 36

3.2.1 Experimental observation of self-healing properties in HC beams 36

3.2.2 Energy flow in Helico-conical beams 38

References 40

4 Transverse Doppler shift with Structured light 41

4.1 Theoretical description of the transverse Doppler shift 42

4.1.1 The longitudinal Doppler shift 42

4.1.2 The transverse Doppler shift 42

4.2 Experimental detection of transverse particle movement with structured light 45

4.2.1 Experimental implementation 46

4.2.2 Experimental results and discussion 48

4.3 Direction sensitive transverse velocity measurement by phase modulated structured light 50

4.4 Measuring the translational and rotational velocities of particles in helical motion. . . 55

4.4.1 Theoretical framework 56

4.4.2 Experimental implementation 57

References 61

5 Nanostep height measurement via spatial mode projection 63

5.1 Common path interferometry 64

5.1.1 The quadrature condition 65

5.2 Spatial mode projection to measure layer thicknesses 66

5.3 Experimental demonstration 68

References 72

6 Optical Chirality 73

6.1 Polarization of light 73

6.2 Chirality 74

6.2.1 The role of circular polarization in chirality 74

6.2.2 Superchiral fields and optical chirality 75

6.3 The role of orbital angular momentum in chirality 77

6.3.1 Derivation of the generalized dissymmetry factor 77

6.3.2 Dissymmetry factor for Bessel beams 79

6.3.3 Enhanced dissymmetry factor with Bessel beams 81

References 84

7 Conclusions 87

List of Figures

2.1 The Gaussian beam is one of the simplest solutions to the paraxial wave equation. It represents a paraboloidal wave with wave front radius of curvature $R(z)$ and a beam width $W(z)$. 14

2.2 Theoretical phase and intensity plots of Hermite-Gaussian modes. 16

2.3 The transverse intensity profile of an LG beam with $p = 0$ for (a) $\ell = 1$ and (d) $\ell = 2$ winding numbers features a doughnut shaped intensity profile. (b) and (e) are their respective phases in the transverse plane. (c) and (f) represent their respective helicoidal wavefront upon propagation. 17

2.4 Theoretical phase and intensity plots of Laguerre-Gaussian modes. 18

2.5 Theoretical phase and intensity profiles of Bessel modes 19

2.6 In the immediate vicinity of a vortex, the azimuthal phase term produces an optical field with a helicoidal wave front 24

2.7 The direction of the OAM vector L of a beam propagating along the positive $\hat{\mathbf{z}}$ direction depends on the sign of the winding number ℓ. (a) For $\ell > 0$ both vectors have the same direction, where as for $\ell < 0$ they have opposite direction (b). If the beam changes its direction, for instance by being reflected by a perfect mirror, the direction of L remains the same (c) and (d). The interference of the OAM beam with a slightly tilted Gaussian beam produces a typical fork-like interference pattern that point up or down depending on the sign of the index ℓ. . . . 25

2.8 An HG_{nm} output of a conventional laser can be transformed by means of a cylindrical lens mode converter into an LG beam of radial number $p = min(n, m)$ and winding number $\ell = \pm|m - n|$, provide, that a separation between the cylindrical lenses is $\sqrt{2}f$. 25

2.9 (a)A spiral phase plate and (b) its phase distribution. 26

2.10 A collimated Gaussian beam can be transformed into a helical beam by inserting a spiral phase plate aligned with its optical axis. 27

2.11 Examples of blazed holograms that create vortex beams with (a) single and (b) double helical wave front. 27

2.12 (a) A forked hologram produced by the addition of a blaze grating and the spiraling phase is use to separate modulated light from un-modulated. (b) The use of fork holograms produce several diffracted orders 28

2.13 A beam with a flat phase impinging on a q-plate can be converted into a helically-phased beam carrying OAM. 29

3.1 (a) Phase mask encoded in an SLM to produce the AiryBeam. (b) Intensity profile of an Airy beam 34

3.2 Experimental intensity pattern and phase of Laguerre-Gaussian beams with winding numbers $\ell = 2$ [(a) and (d)] and $\ell = -2$ [(b) and (e)] and petal-like beam [(c) and (f)]. 35

3.3 (a) and (c) On-axis Holograms to generate $K = 0$ and $K = 1$ HC beams respectively. (b) and (d) Far field intensity pattern of $K = 0$ and $K = 1$ HC beams. 36

3.4 (a) Experimental setup. (b) Samples of unblocked (above) and blocked (below) holograms encoded onto a SLM. Lenses L1 and L2 expands and collimates the incoming beam while M1 and M2 mirrors for alignment; BS is beam splitter and CCD stands for Charge Coupled Device camera. 37

3.5 Experimental [(a) and (b)] and theoreticl [(c) and (d)] intensity profiles of Helico-conical beams, after 16cm propagation distance. In (a) $k = 0$ and in (b) $K = 1$. 37

3.6 A 0.38mm strip is placed at the path of a $\ell = 40$ HC beam. Top images are obtained right after the block while the bottom images are after 8 cm of propagation. (a) corresponds to $K = 0$ and (b) to $K = 1$, in both cases, first column are experimental images while second columns are simulations. 38

3.7 Numerical simulation of the energy flow with an obstruction (a) and without the obstruction (b). The energy flow is unaltered with the presence of the block, it always flows in a circulatory way, being this, responsible for the reconstruction of the intensity in HC beams. 39

4.1 (a) A particle moving in a light beam with structured linear phase gradient. (b) Variation in time $(t_1, t_2, t_3, ...)$ of the particle across the structured light beam induces a frequency shift $\Delta f = \gamma \mathrm{v}_\perp/2\pi$, scalable with γ 44

4.2 (a) A rotating particle being illuminated with an LG beam endowed with OAM. (b) Variation in time $(t_1, t_2, t_3, ...)$of the particle yields a frequency shift $\Delta f_\perp = |\ell\Omega|/2\pi$ to the reflected light that can be scaled with ℓ. $\Delta f_\perp$ regardless of the wavelength of the illuminating source. 44

4.3 A collimated Gaussian beam is divided by a beam splitter (BS) into a reference beam (green line) and a probe beam. The probe beam acquires the desired phase profile after impinging on the SLM. This structured light (blue line) is then made to shine onto a Digital Mirror Display (DMD). The DMD is controlled to mimic a moving particle. Light reflected by the particle (red line) is made to interfere with the reference beam at the photodetector (PD). 46

4.4 (a) Example of the holograms encoded in the SLM. (b) Reference beam. (c) Structured light beam (in this case, LG_0^6). (d) Interference of the Structured light beam with the reference beam. 47

4.5 (a) Digital Micromirror Device (DMD). 48

4.6 (a) Raw signals detected by the photodetector as acquired by the oscilloscope when the particle moving in a circular motion with $\Omega = 16.36\, s^{-1}$, is being illuminated by a beam with a helical phase $\phi = 2\pi\ell$ with topological charge $\ell = 4$. (b) Power spectra obtained with an FFT algorithm after being processed. The peaks in (c) and (d) correspond to the Doppler frequency shifts of $\ell\Omega/(2\pi) = 2.60 Hz$ and $10.41 Hz$, respectively. See text for further details. 49

4.7 Detected frequency shifts when the target moves in a rectilinear path. (a) The target is set to move at different rectilinear velocities when illuminated by a beam with a linear phase gradient of $\gamma = 17.92$ mm^{-1}. (b) The target moves under the illumination of a beam with different linear phase gradients γ at a constant linear velocity of $\mathrm{v} = 4.68\, mm/s$. 50

4.8 Detected frequency shifts when the target moves in a circular path. (a) The target is set to move at different circular velocities when illuminated by a beam with a helical phase of $\phi = 6\pi$, corresponding to $\ell = 3$. (b) The target moves at a constant circular velocity of $\Omega = 16.36\, s^{-1}$. The particle is illuminated with a phase gradient $\phi = 2\pi\ell$, where ℓ is the winding number. 50

4.9 (a) The illuminating beam's phase is rotated either clockwise or anti-clockwise with angular velocity Ω_s. The phase changes from zero (blue) to 2π (red) ten times around the azimuth. (b) Fork-like hologram displayed in the SLM to generate the LG_0^{10} mode. (c) Experimental intensity profile of the generated beam (4mm in diameter). The target, a 70 μm in diameter disk-like particle (shown here exaggerated for illustrative purposes) rotates around the LG_0^{10} beam in the region of maximum intensity. (d) Interference pattern between the LG_0^{10} and a Gaussian beam obtained in experiments. 52

4.10 Experimental setup to extract the rotation velocity and its sense of direction. PBS: polarizing beam splitter; M: mirror; L: lens; PD: photodetector; SLM: Spatial Light Modulator; SF: spatial filter; QWP: Quarter-Wave Plate; DMD: Digital Micro-mirror Device. *See text for details.* 53

4.11 Fourier spectrum obtained when an LG_0^{10} impinges on a particle rotating at an angular velocity $\Omega_t = 3.27s^{-1}$. On (a) the phase is static. From (b) to (d) the phase of the LG_0^{10} is rotated counterclockwise with increasing angular velocities. From (e) to (g) it is rotated clockwise, also with increasing angular velocities. 54

4.12 Frequency shift as function of the angular velocity of the phase gradient of the illuminating beam. The particle rotates clockwise (solid line) or anti-clockwise (dashed line). 55

4.13 (a) Intensity profile of the LG_0^{10} beam illuminating the Digital Micromirror Device (DMD). (b) Interference of the LG_0^{10} beam with the reference beam. The 10 lobes observed are due to the phase profile $\Psi = 10\phi$. (c) Schematic representation of the helical trajectory followed by particles. Z is the propagation axis of the beam. 56

4.14 (a) Experimental setup. (b) Raw signal after balanced detection. (c) Autocorrelation function of the signal. (d) Power spectral density. We only show the spectrum above the chopping frequency. PBS: polarizing beam splitter; M: mirror; L: lens; PD: photodetector; SLM: Spatial Light Modulator; SF: spatial filter; OCh: optical chopper; QWP: Quarter-Wave Plate; DMD: Digital Micromirror Device. *See text for details.* 58

4.15 Frequency shift measured under illumination with a Gaussian mode ($\ell = 0$) for any direction of translation ($v_z > 0$ and $v_z < 0$), and any sense of rotation ($\Omega > 0$ and ($\Omega < 0$). For the sake of comparison, the case with $\Omega = 0$ is also shown. 59

4.16 Frequency shift measured under illumination with a LG_0^{-10} mode for $v_z > 0$ and $v_z < 0$, and for $\Omega > 0$ and ($\Omega < 0$. 59

4.17 Frequency shift measured under illumination with a LG_0^{10} mode for $v_z > 0$ and $v_{H}z < 0$, and for $\Omega > 0$ and ($\Omega < 0$. 60

5.1 (a) By carefully selecting the focusing lens, a Gaussian beam can be made to straddle a ridge with half of the intensity impinging on the ridge and half on the land. (b) Far field interference pattern for the case h= $\lambda/4$. 64

5.2 (a) Far field intensity along the optical axis as function of the height h, a sinusoidal response can be observed. (b) Far field intensity for three specific heights: h= 0, h= $\lambda/8$ and h= $\lambda/4$. . . 65

5.3 (a) A sample of thickness d placed over a ridge of height h is illuminated with a Gaussian beam of waist W_0 for its analysis. (b) The far field intensity along the optical axis as function of the height h for three different values of d: d= 0, d= 10 and d= 40. As d increases, the sinusoidal intensity shifts to the right. 66

5.4 Change in intensity due to the addition of a layer of thickness d on top of the ridge. Three cases are shown: h= 0, h= $\lambda/8$ and h= $\lambda/4$. The highest intensity changes happens at h= $\lambda/8$. 66

5.5 (a) The sample is illuminated with a Gaussian beam in such a way half of the intensity is reflected from the sample whereas the other half from the land. (b) The reflected light is then projected onto an appropriately engineered mode where the quadrature condition is imposed via a phase discontinuity tailored according to the form of the sample.The phase discontinuity introduced by the sample must coincide with the phase discontinuity of the projection mode. . 67

5.6 The experimental setup. A He-Ne laser beam impinges perpendicularly over the sample. The reflection from the sample is projected onto a SLM where a desired phase is encoded. The resulting beam intensity is measured with a photodectector. 68

5.7 Normalized intensities for P when projected onto a mode of phases $\Delta\varphi$ and $-\Delta\varphi$ for different heights: (a) sample 1 (1.9 nm measured height, 0 nm profilometry measurement), (b) sample 2 (9.7 nm measured height, 8 nm profilometry measurement), and (c) sample 3 (29.0 nm measured height, 31 nm profilometry measurement). All measurements have standard error of ~0.2 nm. 69

5.8 Typical data for analysis. (a) Normalized power difference $P_{\Delta\varphi} - P_{-\Delta\varphi}$ as a function of $\Delta\varphi$. (b) The difference as a function of $\sin(\Delta\varphi)$ is linear as described by Eq. (5.11). Line fit is from the calculated height (dashed line) and from theoretical calculations (solid line). For all plots, the theoretical curve is calculated from a step height of 31 nm, which is independently measured with a profilometer. 70

5.9 Normalized differential signal $(P_1 - P_2)/P_0$ as a function of the sample height when the reflected signal is projected onto a Gaussian mode with phase step $\Delta\varphi$. The solid, dashed, and dashed-dotted (×10) lines correspond to $\Delta\varphi = 0, \pi/2, \pi/4$ respectively. 71

6.1 (a) The mirror image of a chiral object can not be brought into coincidence with itself. (b) A non-chiral object and its mirror image are exactly the same. 75

6.2 Representation of the interaction of (a) right- and (b) left-CPL with chiral molecules. The absorption in the amount of CPL by chiral molecules depends on the direction of rotation of CPL, in (b) the absorption is considerably higher compared to (b). 76

6.3 The helicoidal phase of two beams with opposite winding numbers (a) $\ell = -1$ and (b) $\ell = +1$ rotates in opposite direction, in a similar way to CPL. 77

6.4 Illustration of the expected response from chiral molecules upon interaction with an OAM beam with winding number (a) $\ell = 1$ and (b) $\ell = +1$. In (a) the transmitted intensity of the helical beam remains the same whereas in (b) part of it is absorbed by the molecule resulting in a decreasing of the transmitted intensity. 78

6.5 Dissymmetry factor. 81

6.6 Relative dissymmetry factor as function of the amplitude of the superimposed beams (A and B), for the case $k_t/k_z = 0.1$. 82

6.7 Relative dissymmetry factor as a function of the polarization angle ϕ for two values of the ratio $r = |B|/|A|$: $r = 0.95$ (red lines) and $r = 1.05$ (black lines), and three values of the angle ξ: 0^o (solid), 90^o (dashed) and 180^o (dotted). In all cases $k_t/k_z = 0.1$. 83

List of symbols

Symbol	**Meaning**
$\mathbb{D}$	Time-dependent electric displacement.
$\mathbb{E}$	Time-dependent electric field.
$\mathbb{B}$	Time-dependent magnetic field.
$\mathbb{H}$	Time-dependent magnetic field inside matter.
$\mathbb{J}$	Time-dependent electric current density.
ϱ	Time-dependent electric charge density.
$\mathbf{D}$	Time-independent electric displacement.
$\mathbf{E}$	Time-independent electric field.
$\mathbf{B}$	Time-independent magnetic field.
$\mathbf{H}$	Time-independent magnetic field inside matter.
$\mathbf{r}$	Vector position.
t	Time.
∇	Nabla operator.
∂	Partial derivative.
ϵ_0	Electric permittivity.
μ_0	Magnetic Permeability.
c	Speed of light.
ω	Angular frequency of light.
$\mathbf{k}$	Wave vector.
k	Magnitude of the wave vector.
λ	Wavelength of light.
$\mathbb{A}$	Time-dependent vector potential.
$\mathbf{A}$	Time-independent vector potential.
Φ	Time-dependent scalar potential.
ρ	Radial coordinate of cylindrical coordinates.
ϕ	Azimuthal coordinate of cylindrical coordinates.
z_R	Rayleigh Range.
ℓ	Winding number.
$J_m(x)$	Bessel polynomial.
$\mathbb{S}$	Time-dependent Poynting vector.
$\mathbf{p}$	Linear momentum density.
$\mathbf{j}$	angular momentum density.
$\hat{\mathbf{n}}$	Unitary polarization vector.
$\langle s \rangle$	Time average Poynting vector.
$\langle p \rangle$	Time average linear momentum.
$\langle j \rangle$	Time average angular momentum.
$\langle j_z \rangle$	Time average angular momentum directed along z.

Symbol	**Meaning**
α and β	Complex polarization components in the transversal plane.
s	Spin angular momentum.
S	Total spin angular momentum.
$\mathcal{W}$	Energy per unit time.
$\mathbf{E}$	Energy per unit volume.
l	Orbital angular momentum.
L	Total orbital angular momentum.
J_z	Total angular momentum, spin plus orbital, along the z direction.
n	Refraction index.
g	Dissymmetry factor.
g_{CPL}	Dissymmetry factor for circularly polarised light.
C	Optical chirality.
U_e	Local electric energy density.
R	Mirror reflectivity.
$A^{\pm}$	Absorption rate of circularly polarised light by molecules.
$A^{\pm\ell}$	Absorption rate of light endowed with orbital angular momentum by molecules .
G''	Electric-magnetic polarizability.
α''	Electric polarizability.
$\tilde{\mathbf{p}}$	Electric dipole moment.
$\tilde{\mathbf{m}}$	Magnetic dipole moment.
$\tilde{\mu}_E$	Electric polarizability.
$\tilde{\mu}_B$	Magnetic polarizability.
g_ℓ	Dissymmetry factor for light endowed with OAM.
k_t	Transversal component of the wave vector.
k_z	Longitudinal component of the wave vector.
C_B	Chirality for Bessel beams.
G_ℓ	Dissymmetry factor relative to circularly polarised light.
Θ	Time-varying phase.
Ψ	Spacial- varying phase.
$\mathbf{v}_\perp$	Velocity vector in the transversal plane.
$\mathrm{v}_\perp$	Magnitude of the vector velocity $\mathbf{v}_\perp$.
$\mathrm{v}_{\|}$	Velocity component along the line of sight.
f	Frequency of light.
Δf	Longitudinal Doppler Shift.
$\Delta f_\perp$	Transversal Doppler Shift.
Ω	Angular velocity of rotation.
R_0	Radial distance.
F	Lens focal length.
Ω_t	Angular velocity of a rotating phase.

List of acronyms

Acronym	**Meaning**
HG	Hermite-Gaussian beams.
LG	Laguerre-Gaussian beams.
BB	Bessel Beams.
SLM	Spatial Light Modulator.
SAM	Spin Angular Momentum.
OAM	Orbital Angular Momentum.
STOC	Spin-to-Orbital Conversion of angular momentum.
QP	q-Plates.
HC	Helico-conical beams.
CCD	Charge-Coupled Device camera.
CPL	Circularly Polarised Light.
CD	Circular Dicrhoism.
OC	Optical Chirality.
CW	Continious Wave.
CGH	Computed Generated Hologram.
DMD	Digital Micromirror Device .
LED	Light Emitting Diode.
He-Ne	Helium-Neon.
BS	Beam Splitter.
PBS	Polarizing Beam Splitter.
PD	Photodetector.
DO	Digital oscilloscope.
DFT	Discrete Fourier Transform.
FFT	Fast Fourier Transform.
H. c.	Hermitian conjugate.
QWP	Quarter-wave Plate.
HWP	Half-wave Plate.
SF	Spatial Filter.
OCh	Optical Choper.

1

Introduction

In the XVII century, the mechanical properties of light where already considered [1, 2]. Johannes Kepler believed that radiation pressure from sun's light caused the comet tails to point away from it, although at this early stage it was not possible to quantify these effects. It was only after the renowned Maxwell unification theory of electricity, magnetism and optics that the ideas of the electromagnetic field and its mechanical properties were first expressed in a clear and consistent form. In his treatise on electromagnetism, Maxwell quantified the radiation pressure at the earth surface due to sun light, yet, it contains little more on the mechanical properties of light. Few years later, in 1898, A.I. Sadovsky predicted that light with elliptic polarization will exert a rotatory action upon material objects [3]. However, it was only after Poynting's theory of electromagnetic radiation pressure and momentum density, that a clear manifestation of light's mechanical properties was plainly stablished [4]. Using a mechanical analogy, Poynting was able to show that Circularly Polarized Light (CPL) should carry angular momentum (AM). Moreover, he suggested that when CPL passes through a quarter wave plate, AM should be transferred to the waveplate. He even proposed an experiment to measure this quantity. Poynting's predictions were corroborated in 1936 in two independent experiments by Holbourn [5] and by Beth [6]. In a very clever way, Beth was able to quantify the AM of a single circularly polarized photon by measuring the mechanical torque exerted by a circularly polarized plane wave to a birefringent plate hanging from a torque balance. This form of AM is nowadays known as spin (or intrinsic) angular momentum (SAM).

In 1992 Allen *et al.* realized that, in addition to intrinsic AM, Laguerre-Gaussian (LG) laser modes carry another form of AM associated to their characteristic azimuthal varying phase $\exp[i\ell\phi]$. This type of AM is the Orbital (or extrinsic) Angular Momentum (OAM). This phase varies from zero to 2π in the plane perpendicular to the propagation direction, featuring an on-axis singularity. The term ℓ, known as the winding number or topological charge, accounts for the number of times the phase wraps around such singularity. Upon propagation, the phase evolves forming a helicoidal structure around a dislocation line known as optical vortex. For $\ell = 1$ the phase fronts resembles a simple screw thread, whereas for $\ell = 2$ they form a double helix. Along the dislocation line the amplitude is zero, giving as result a ring-shaped or doughnut intensity profile. Allen *et al.* also proposed an experiment to observe the transfer of the OAM associated with its optical vortex to a macroscopic object. In the experiment, a pair of cylindrical lenses suspended on a torsion fiber would reverse the helicity of a LG beam and suffer a reaction torque. However, this torque is very small for reasonable power beams, making its detection challenging in the macroscopic world. Nevertheless, such effects have been observed on a microscopic scale, in the context of optical trapping [7]. In general, the total AM cannot be separated into its spin and orbital contributions, but within the paraxial approximation this becomes possible.

The OAM of light couples mainly with material inhomogeneities characterized by a rotational asymmetry around the beam axis. This feature allows light beams endowed with OAM to have potential applications in a huge variety of fields. For example, as a sensing tool [8, 9], in optical microscopy [10, 11, 12, 13], optical tweezers [14], optical communications [15], astrophysics [16], quantum information [17, 18, 19], among others. Some of these applications will be reviewed next.

Optical tweezers were pioneered by Askin and co-workers in the 1980s [20]. The basic idea is to create a steep intensity gradient, so that dielectric particles immersed in a liquid medium experience a force towards the point of maximum intensity. Scattering, gravity and thermal forces are also involved in the trapping, hence the trap's stability depends on the balance between all of them. Unfortunately, in the presence of absorbing particles these optical tweezers are often unstable, mainly because they experience a much higher scattering force. In this context, the on-axis intensity minimum of ring-shaped beams provides with an alternative tool, not only to confine, but also to guide absorbing particles along the core of the ring shaped beams. This idea was first conceived by Ashkin in 1992, who used a small stop at the center of a Gaussian beam to create a doughnut-like beam [21]. In 1995 Rubinsztien-Dunlop and co-workers implemented for the first time an optical trap capable to held particles at the dark centre of the beam [22]. Interestingly, they observed that the associated OAM of the beam induced a rotation on the particle, confirming that the OAM of light could be coupled to a mechanical system. Along the same line, in 2002, Padgett and co-workers where able to confine small silica particles around the bright ring of a large Laguerre-Gaussian beam [14]. Many other works related to the use of OAM beams in optical tweezers have been published since then, see for instance [23, 24] and references therein. The field of optical manipulation has been dramatically transformed since the advent of Spatial Light Modulators (SLM), that provide with an easy and flexible way to create structures light beams [25, 26]. The great potential of SLMs has allowed for the implementation of multiple-trap optical tweezers, known as "holographic optical tweezers" [27, 28, 29], or the creation of exotic beams capable of trap and guide microparticles along parabolic or helical trajectories [30, 31, 32].

Optical microscopy is a fascinating field. Since its invention in the seventeen century it has allow for great discoveries and scientific advances. However, its resolution is naturally limited by the diffractive properties of light, in such a way optical microscopes are not capable to distinguish structural details finer than roughly $\lambda/2$ (about 200 nm). In the 1990s, super-resolution techniques to overcome such limitation started to emerge. Among these, Stimulated Emission Depletion (STED) has stand out because it is a purely optical method that does not require any additional image processing or mathematical manipulation [11, 12]. This technique is capable of 20 nanometer (or better) lateral resolution and 40 to 50 nanometer axial resolution by using structured light beams in combination with fluorophores. The idea behind STED is to illuminate the sample with two beams, where an excitation laser pulse is closely followed by a doughnut-shaped pulse termed the STED beam. Even tough both laser beams are diffraction limited, the key point is the STED pulse features a zero intensity point at its centre and a strong intensity at its periphery. In this way, the first pulse excites the fluorophores inside the illuminated region and the second pulse returns those within the ring-shaped area to the ground state by means of stimulated emission. Therefore, only molecules in the centre of the STED beam will fluoresce [13]. As consequence, the point spread function narrows, highly increasing the resolution beyond the diffraction limit.

In recent years quantum information has attracted a lot of attention because its promising applications in quantum communications and criptography [33, 34, 35]. Quantum information technologies rely on transmitting and processing data encoded in physical systems. Tipically, the unit of information is a two-level system, known as a quantum bit or qubit, that exhibits uniquely quantum mechanical properties [36, 37, 38]. Interestingly, qubits allow for the transfer of more information than the classical boolean alphabet. Moreover, the quantumness of qubit systems ensure high level of security in communication processing [39]. In this context, photons are very promising as qubits because of their high speed of transmission, ease of manipulation at the single qubit level, low noise properties and availability of multiple degrees of freedom for encoding [40]. The need for more secure and faster information transfer, has ignited the search for higher dimensional systems to encode and manipulate quantum information. Another advantage of increasing the information content per photon is the substantial depletion of noise and losses. Some schemes to perform quantum computation in higher dimensional systems have been already suggested [41]. The orbital angular momentum, defined in an infinite dimensional Hilbert space, provides a natural orthogonal basis that can be used as the 'letters' (qudits) of a higher dimensional quantum information alphabet [42, 43]. Among the tools needed to produce secure quantum communications and quantum information processing are: the generation of entangled orbital angular momentum states, the controlled superpositions of orbital angular momentum states and the detection of these states [17, 18, 19]. Up to now, most of the experiments have implemented only a small number of different orbital angular momentum states. Increasing this number remains a technical challenge.

The realisation that light beams can also carry OAM has ignited new lines of research, both in fundamental aspects and in the search for new applications [44, 45, 46]. Within this context, during the past four years we have worked in the development of new tools involving the use of structured light. In this thesis, the term structured light is applied to all light beams with a transversally varying phase, this is, different points in the transverse plane can be associated with different values of the phase, as in Laguerre-Gaussian, Bessel, Airy, Helico-conical, Mathieu or Weber beams.

The content of this thesis is as follow. First, in chapter 2 we establish the theoretical basis for the subsequent chapters. This chapter is divided into four sections. We start by rewriting Maxwell equations in free space, and from these we derive the paraxial wave equation using the potential vector approach and the Lorentz gauge (Section 2.1). Later, in Section 2.2, we present some of the most common solutions to the paraxial wave equation, emphasizing in those endowed with OAM. Section 2.3.2 is devoted to the mathematical description of the angular momentum of light within the paraxial regime, where it can be separated into spin and orbital angular momentum. In the last section of this chapter (Section 2.4), we describe some of the current techniques used to produce structured light beams, being optical vortices an special case.

In chapter 3 we report our first contribution in the area of fundamental aspects of structured light: the self-healing properties of Helico-conical (HC) beams [47]. On the one hand, self-healing beams are of special interest because they have the ability to self-reconstruct their intensity profile after being disturbed by an obstacle placed in its propagation path. This property is of special interest mainly because it amplifies their range of applications, for example in turbulent media. On the other hand, HC beams being the product of a conical and a helical phase [48], are unique in the sense that both their intensity profile and phase are helicoidal. Their far field projection (a spiral) is of great interest because it maintains a high concentration of photons, even for large values of OAM. The chapter contains two sections, in the first one (Section 3.1) we describe some of the beams that are known to self-heal: Airy, Mathieu, petal-like and Pearcy beams. In this section we also describe, in an intuitive way, the fundamental role that energy transport plays in the self healing process. The second section (Section 3.2) is entirely devoted to HC beams. First we briefly describe how they can be created in the lab and some of their properties. Then we describes in detail the experimental observation of the self-healing properties of these beams. We also present some numerical simulations to corroborate our results. Not surprisingly, our simulations show that the transport of energy from unblocked areas to blocked areas is indeed responsible for the self-reconstruction of the intensity profile.

Chapter 4 describe a novel technique, first proposed by A. Belmonte and J. P. Torres [49], based on the use of structured light to measure in a direct way the transverse component of velocity. The chapter is divided into four sections. In the first section we discuss the theoretical aspects that are the basis for this technique (4.1). In essence, a moving target is illuminated with an structured light beam. In this way, the target scatters back light with a transverse position-dependent phase. For example, let us consider the case of a particle that rotates around certain axis. In order to measure its angular velocity, one can use an optical beam with an azimuthal dependent phase that propagates along the particle axis of rotation, *i.e.*, perpendicularly to its plane of rotation. As the particle rotates, it will scatter back a portion of the incident light whose phase changes according to the speed of the particle. Hence, when this light is interfered with a reference beam (which for simplicity can be a Gaussian), a beating signal will be produced. The Fourier transform of such signal yields a unique frequency peak proportional to the angular velocity of the particle. The experimental demonstration of this technique is described in Section 4.2, applied to two simple types of motion: rotational and translational [50]. Since we are able to measure only intensity changes, this technique is not sensitive to the direction of motion, even though in many cases this information is of great relevance. There are several ways to retrieve this information, most of them require the use of additional devices (for example acousto-optic or electro-optic modulators or rotating optical devices). We propose a technique (described in Section 4.3) which does not requires additional elements other than the one that generates the structured light beam. The key point is the use of dynamic phases rather that static. For instance, for the case of a rotating target, the use of a beam whose phase rotates in a know direction will allow to discriminate the sense of rotation of the target [51]. Finally in the last section (Section4.4) we extend this technique to more complex movements, as is the case of particles moving in 3-dimentions. In particular, we analysed the case of helical motion [52], which is interesting because most of the aquatic microorganisms smaller than 0.5 mm exhibit this kind of motion when searching for food, to move toward appropriate temperature or pH, or simply to escape from predators.

Chapter 5 describes our results regarding the use of structured light for the measurement of layer thicknesses with high accuracy. This chapter consist of tree sections. In Section 5.1 we briefly introduce the concept of common path interferometry (CPI). In CPI, an unperturbed part of the beams is used as reference and travels the same path as the signal beam, making this scheme very useful for the measurement of phase changes, especially when it is locked to the so called quadrature condition (this is, when the reference beam is forced to be $\pi/2$ out of phase with respect to the signal beam). At this condition, the system becomes very sensitive and allows for the detection of small phase changes. CPI at quadrature condition have been very useful in the bio-CD technology, where thin layers of molecules are attached to a compact disk for its analysis [53, 54, 55]. In this case, the quadrature condition is imposed by placing the sample over a ridge of height h= $1/4$ of the wave- length. Unfortunately, this way of imposing the quadrature condition might restrict the use of this technique to the technology available for the construction of the ridges. This limitation can be overcomed by using mode projections. In essence, the quadrature condition is passed on to the reflected beam by projecting it onto an appropriately tailored mode. The principle of mode projection is introduced in Section 5.2, where we also state the mathematical relations that allow us to implement experimentally the quadrature condition without the need to fabricate a ridge. The principle was demonstrated in an experiment reported in [56] and fully described in Section 5.3.

Finally, in chapter 6 we report our theoretical results regarding the use of beams endowed with OAM for the discrimination of chiral molecules. Chirality is of great relevance because some of the most important building blocks of life (aminoacids and sugars) are chiral. This property is also of great interest in the drug industry because enantiomers (a pair of molecules one being the mirror image of the other) are identical in most regards but can have very different physiological effects [57]. In general, chiral objects interact in different ways with other chiral objects. For example, the rate of absorption of Circularly Polarized Light (CPL) by chiral molecules is different depending on the sense of rotation of the polarization vector. In many cases, the difference of absorption is very week and huge efforts have been made trying to enhance this response. Within this line, we investigated the role that helical beams endowed with OAM might play. We start this chapter with a brief historical introduction to polarization (Section 6.1) followed by an introductory section to chirality and the important role CPL plays in discriminating enantiomers (Section 6.2). In this section, we also discuss about chiral fields and how they can be used to produce a chiral response [58, 59]. In Section 6.3 we report on the use of helical beams to induce an enhanced chiral response [60].

References

[1] J. Kepler, “Ad vitellionem parali pomena,” Frankfort (1619).

[2] J. Keppler, “De cometis liballi tres,” Augsburg (1619).

[3] A. Sadowsky, “Acta et Commentationes,” Imp. Universitatis Jurievensis **7**, 1–3 (1899).

[4] J. H. Poynting, “The wave motion of a revolving shaft, and a sugesstion as to the angular momentum in a beam of circularly polarised light,” Proc. Roy. Soc. London **Ser. A 82**, 560–567 (1909).

[5] A. H. S. Holbourn, “Angular momentum of circularly polarised light,” Nature **137**, 31 (1936).

[6] R. A. Beth, “Mechanical detection and measurement of the angular momentum of light,” Phys. Rev. **50**, 115–125 (1936).

[7] H. He, M. E. J. Friese, N. R. Heckenberg, and H. Rubinsztein-Dunlop, “Diret Observation of the Transfer of Angular Momentum to Absorptive Particles from a Laser Beam with a Phase Singularity,” Phys. Rev . Lett. **75**, 826–829 (1995).

[8] S. Moed, R. L., J. P. Torres, L. Torner, and S. Carrasco, “Probing canonical geometrical objects by digital spiral imaging.” J. Europ. Opt. Soc. Rap. Public **2** (2007).

[9] L. Torner, J. Torres, and S. Carrasco, “Digital spiral imaging,” Opt. Express **13**, 873–881 (2005).

[10] F. Tambutini, G. Anzolin, G. Umbriaco, A. Bianchini, and C. Barbieri, “Overcoming the Rayleigh criterion limit with optical vortices.” Phys. Rev . Lett. **97**, 163903 (2006).

[11] S. W. Hell and J. Wichman, “Breaking the diffraction resolution limit by stimulated emission: stimulated-emission-depletion fluorescence microscopy,” Opt. Lett. **19**, 780–782 (1994).

[12] S. W. Hell and M. Kroug, “Ground-state depletion fluorescence microscopy, a concept for breaking the diffraction resolution limit,” Appl. Phys. B **60**, 495–497 (1995).

[13] S. W. Hell, “Far-field optical nanoscopy,” Science **316**, 1153–1158 (2007).

[14] A. O’Neil, I. MacVicar, L. Allen, and M. Padgett, “Intrinsic and extrinsic nature of the orbital angular momentum of a light beam.” Phys. Rev. Lett. **88**, 053601 (2002).

[15] N. Bozinivic, Y. Y., Y. Ren, M. Tur, P. Kristensn, H. Huang, Willner, and S. Ramachandran, “Terabit-scale orbital angular momentum mode division multiplexing in fibers.” Science **340** (2013).

[16] F. Tambutini, T. Bo, G. Molina-Terriza, and G. Anzolin, “Twisting of light around rotating black holes,” Nature Phys. **7** (2011).

[17] G. Molina-Terriza, J. P. Torres, and L. Torner, “Management of the Angular Momentum of Light: Preparation of Photons in Multidimensional Vector States of Angular Momentum,” Phys. Rev . Lett. **88**, 013601 (2002).

[18] A. Vaziri, G. Weihs, and A. Zeilinger, “Experimental Two-Photon, Three-Dimensional Entanglement for Quantum Communication.” Phys. Rev . Lett. **89**, 240401 (2002).

[19] J. P. Torres, Y. Deyanova, L. Torner, and G. M. Terriza, “Preparation of engineered two-photon entangled states for multidimensional quantum information,” Phys. Rev. A **67**, 052313 (2003).

[20] A. Ashkin, J. Dziedzic, J. Bjorkholm, and S. Chu, “Observation of a single-beam gradient force optical trap for dielectric particles.” Opt. Lett. **11**, 288–290 (1986).

[21] A. Ashkin, “Forces of a single-beam gradient laser trap on a dielectric sphere in the ray optics regime.” Biophys. J. **61**, 569–582 (1992).

[22] H. He, N. R. Heckenberg, and H. Rubinsztein-Dunlop, “Optical particle trapping with higher-order doughnut beams produced using high efficiency computer generated holograms,” J. Mod. Opt. **424**, 217–223 (1195).

[23] M. Padgett and R. Bowman, “Tweezers with a twist.” Nature Photonics **5**, 343–348 (2011).

[24] M. Babiker and D. L. Andrews, “Optical Manipulation of Atoms and Molecules Using Structured Light,” African Physical Review **1**, 18–33 (2007).

[25] Y. Hayasaki, M. Itoh, T. Yatagai, and N. Nisida, “Nonmechanical optical manipulation of microparticle using spatial light modulator.” Opt. Rev. **6**, 24–27 (1999).

[26] M. Reicherter, T. Haist, E. Wagemann, and H. Tiziani, “Optical particle trapping with computer-generated holograms written on a liquid-crystal display,” Opt. Lett. **24**, 608–610 (1999).

[27] J. Liesener, M. Reicherter, T. Haist, and H. Tiziani, “Multi-functional optical tweezers using computer-generated holograms,” Opt. Commun. **185**, 77–82 (2000).

[28] J. Curtis, B. Koss, and D. Grier, “Dynamic holographic optical tweezers,” Opt. Commun. **207**, 169–175 (2002).

[29] D. Grier, “A revolution in optical manipulation,” Nature **424**, 810–816 (2003).

[30] J. Baumgartl, M. Mazilu, and K. Dholakia, “Optically mediated particle clearing using Airy wavepackets,” Nature Photonics **2**, 675–678 (2008).

[31] S. Lee, Y. Roichman, and D. Grier, “Optical solenoid beams,” Opt. Express **18**, 6988–6993 (2010).

[32] V. R. Daria, D. Z. Palima, and J. Glückstadckstad, “Optical twists in phase and amplitude,” Opt. Express **19**, 476–481 (2011).

[33] N. J. Cerf, M. Bourennane, A. Karlsson, and N. Gisin, “Security of quantum key distribution using d-level systems,” Phys. Rev . Lett. **88**, 127902 (2002).

[34] B. P. Lanyon, M. Barbieri, M. P. Almeida, T. Jennewein, T. C. Ralph, K. J. Resch, G. J. Pryde, J. L. O’Brien, A. Gilchrist, and A. G. White, “Simplifying quantum logic using higher-dimensional hilbert spaces,” Nature Phys. **7**, 134 (2009).

[35] L. Aolita and S. P. Walborn, “Quantum Communication without Alignment using Multiple-Qubit Single-Photon States.” Phys. Rev . Lett. **98**, 100501 (2007).

[36] M. A. Nielsen and I. L. Chuang, *Quantum Computation and Quantum Information* (Cambridge University Press, 2000).

[37] N. Gisin, G. Ribordy, W. Tittel, and H. Zbinden, “Quantum Cryptography,” Rev. Mod. Phys. **74**, 145–195 (2002).

[38] J. L. 0’Brien, “Optical Quantum Computing,” Science **318**, 1567–1570 (2007).

[39] N. Gisin and R. Thew, “Quantum communication,” Nature Photonics **1**, 165–171 (2007).

[40] S. Portolan, L. Einkemmer, Z. Vörös, G. Weihs, and P. Rabi, “Generation of hyper-entangled photon pairs in coupled microcavities,” New J. Phys. **16**, 063030 (2014).

[41] V. Karimipour, A. Bahraminasab, and S. Bagherinezhad, “Entanglement swapping of generalized cat states and secret sharing,” Phys. Rev. A **65**, 042320 (2002).

[42] G. Molina-Terriza, J. P. Torres, and L. Torner, “Twisted Photons,” Nature Phys. **3**, 305–310 (2007).

[43] S. F. Arnold, L. Allen, and M. Padgett, “Advances in optical angular momentum,” Laser & Photon. Rev **2**, 299–313 (2008).

[44] J. P. Torres and L. Torner, *Twisted Photons* (Wiley-VCH, 2011).

[45] D. L. Andrews and M. Babiker, *The angular momentum of light* (Cambridge University Press, 2013).

[46] D. L. Andrews, *Structured light and its applications* (Elsevier, 2008).

[47] C. Rosales-Guzmán, N. Hermosa, and J. P. Torres, “Helico-conical optical beams self-heal,” Opt. Lett. **3**, 383–385 (2013).

[48] C. Alonzo, P. J. Rodrigo, and J. Glückstad, “Helico-conical optical beams: a product of helical and conical phase fronts,” Opt. Express **13**, 1749–1760 (2005).

[49] A. Belmonte and J. P. Torres, “Optical Doppler shift with structured light.” Optics letters **36**, 4437–9 (2011).

[50] C. Rosales-Guzmán, N. Hermosa, A. Belmonte, and J. P. Torres, “Experimental detection of transverse particle movement with structured light,” Sci. Rep. **36**, 2815 (2013).

[51] C. Rosales-Guzmán, N. Hermosa, A. Belmonte, and J. P. Torres, “Direction-sensitive transverse velocity measurement by phase-modulated structured light beams,” Opt. Lett. **18**, 5415–5418 (2014).

[52] C. Rosales-Guzmán, N. Hermosa, A. Belmonte, and J. P. Torres, "Measuring the translational and rotational velocities of particles in helical motion using structured light," Opt. Express **22**, 16504–16509 (2014).

[53] M. M. Varma, H. D. Inerowicz, F. E. Regnier, and D. D. Nolte, "High-speed label-free detection by spinning-disk micro-interferometry," Biosensors and Bioelectronics **19**, 1371 (2004).

[54] D. D. Nolte, "High-Speed Spinning-Disk Interferometry on the BioCD for Human Diagnostic Applications," Conf. Proc. IEEE Eng Med Biol Soc. p. 6368 (2009).

[55] M. M. Varma, D. D. Nolte, H. D. Inerowicz, and F. E. Regnier, "High-Speed Label-Free Multi-Analyte Detection through Microinterferometry," Proceedings of SPIE **4966**, 58 (2003).

[56] N. Hermosa, C. Rosales-Guzmán, S. F. Pereira, and J. P. Torres, "Nanostep height measurement via spatial mode projection," Opt. Lett. **39**, 299–302 (2014).

[57] E. Francotte and W. Lindner, eds., *Chirality In Drug Resaerch* (Widley-VCH, 2006).

[58] A. E. Cohen and Y. Tang, "Optical Chirality and its interactions with matter," Phys. Rev . Lett. **104**, 163901 (2010).

[59] Y. Tang and A. E. Cohen, "Enhanced enantioselectivity in excitation of chiral molecules by superchiral light," Science **332**, 333–336 (2011).

[60] C. Rosales-Guzmán, K. Volke-Sepulveda, and J. P. Torres, "Light with enhanced optical chirality," Opt. Lett. **37**, 3486–3488 (2012).

2

The Angular Momentum of Light

Contents

2.1 The Helmholtz equation **10**
  2.1.1 The vectorial Helmholtz equation 10
  2.1.2 The paraxial wave equation 11
2.2 Solutions to the paraxial wave equation **13**
  2.2.1 Solutions in Cartesian coordinates 13
  2.2.2 Solutions in cylindrical coordinates 15
2.3 Angular momentum of Light **19**
  2.3.1 Historical introduction 19
  2.3.2 Mathematical description 20
2.4 Generation of structured light beams **24**
  2.4.1 Intracavity generation 24
  2.4.2 Extracavity generation 25
References **30**

In this chapter we describe the basic theory that supports what is done in the following chapters. We start by deriving the Helmholtz equation from Maxwell equations using the vectorial potential approach (section 2.1.1). In section 2.2 we describe some of the most common solutions to the Helmholtz equation. The conditions for which these solutions might carry angular momentum (AM) along the direction of propagation are discussed in section 2.3, as well as the conditions for which the AM can be separated into spin andf orbital angular momentum. Finally we discuss how to generate beams endowed with Orbital Angular Momentum (OAM).

2.1 The Helmholtz equation

Maxwell equations are the basis of any study regarding electromagnetic systems. Therefore we start this section by rewriting Maxwell equations in its differential form using the international system of units.

I. **Gauss's law**

$$\nabla \cdot \mathbb{D}(\mathbf{r}, t) = \varrho(\mathbf{r}, t) \qquad (2.1a)$$

The sources of the electric displacement $\mathbb{D}$ are the electric charges with density $\varrho(\mathbf{r}, t)$.

II. **Faraday's law**

$$\nabla \times \mathbb{E}(\mathbf{r}, t) = -\frac{\partial \mathbb{B}(\mathbf{r}, t)}{\partial t} \qquad (2.1b)$$

The vortices of the electric field $\mathbb{E}$ are caused by temporal variations of the magnetic induction $\mathbb{B}$.

III. **Gauss's law for magnetism**

$$\nabla \cdot \mathbb{B}(\mathbf{r}, t) = 0 \qquad (2.1c)$$

The magnetic field $\mathbb{B}$ is solenoidal, *i.e.*, there exist no “magnetic charges".

IV. **Ampere's law**

$$\nabla \times \mathbb{H}(\mathbf{r}, t) = \frac{\partial \mathbb{D}(\mathbf{r}, t)}{\partial t} + \mathbb{J}(\mathbf{r}, t) \qquad (2.1d)$$

The vortices of the magnetic field $\mathbb{H}$ are either caused by an electric current with density $\mathbb{J}$ or by temporal variations of $\mathbb{D}$.

In the above equations, $\mathbf{r}$ is the vector position, t is the time and ∇ is the nabla operator in the appropriate coordinates system. We are mostly concerned with the propagation of waves in free space where $\varrho(\mathbf{r}, t)$ and $\mathbb{J}(\mathbf{r}, t)$ are both zero and where the relations,

$$\mathbb{D}(\mathbf{r}, t) = \epsilon_0 \mathbb{E}(\mathbf{r}, t) \qquad (2.2a) \qquad\qquad \mathbb{H}(\mathbf{r}, t) = \frac{1}{\mu_0} \mathbb{B}(\mathbf{r}, t) \qquad (2.2b)$$

are satisfied. Here, ϵ_0 is the electric permittivity (or dielectric constant) and μ_0 the magnetic permeability. These are in general complex quantities related to the physical properties of the medium. Using these relations, equations 2.1 can be written as

$$\nabla \cdot \mathbb{E}(\mathbf{r}, t) = 0 \qquad (2.3a) \qquad\qquad \nabla \cdot \mathbb{B}(\mathbf{r}, t) = 0 \qquad (2.3c)$$

$$\nabla \times \mathbb{E}(\mathbf{r}, t) = -\frac{\partial \mathbb{B}(\mathbf{r}, t)}{\partial t} \qquad (2.3b) \qquad\qquad \nabla \times \mathbb{B}(\mathbf{r}, t) = \mu_0 \epsilon_0 \frac{\partial \mathbb{E}(\mathbf{r}, t)}{\partial t} \qquad (2.3d)$$

2.1.1 The vectorial Helmholtz equation

Applying the rotational operator to both sides of Eqs. (2.3b) and (2.3d) and with the help of the vectorial identity $\nabla \times (\nabla \times \mathbf{F}) = \nabla(\nabla \cdot \mathbf{F}) - \nabla^2 \mathbf{F}$, we arrive to the well known wave equation for the electric and the magnetic fields,

$$\nabla^2 \mathbb{E}(\mathbf{r}, t) + \frac{1}{c^2} \frac{\partial^2}{\partial t^2} \mathbb{E}(\mathbf{r}, t) = 0 \qquad (2.4a) \qquad\qquad \nabla^2 \mathbb{B}(\mathbf{r}, t) + \frac{1}{c^2} \frac{\partial^2}{\partial t^2} \mathbb{B}(\mathbf{r}, t) = 0 \qquad (2.4b)$$

here, $c = 1/\sqrt{\mu_0\epsilon_0}$ the speed of light in vacuum. In this thesis, we assume that the electric and magnetic fields have the form

$$\mathbb{E}(\mathbf{r}, t) = \frac{1}{\sqrt{2\pi}} \int_{-\infty}^{\infty} \mathbf{E}(\mathbf{r}, \omega) \exp[-i\omega t] d\omega \tag{2.5a}$$

$$\mathbb{B}(\mathbf{r}, t) = \frac{1}{\sqrt{2\pi}} \int_{-\infty}^{\infty} \mathbf{B}(\mathbf{r}, \omega) \exp[-i\omega t] d\omega \tag{2.5b}$$

after inserting the above equations [eqs. (2.5)] into Eqs.(2.4) we arrive to the well known vectorial Helmholtz equation

$$\nabla^2 \mathbf{E}(\mathbf{r}, \omega) - k^2 \mathbf{E}(\mathbf{r}, \omega) = 0 \tag{2.6a}$$

$$\nabla^2 \mathbf{B}(\mathbf{r}, \omega) - k^2 \mathbf{B}(\mathbf{r}, \omega) = 0 \tag{2.6b}$$

where, $k = 2\pi/\lambda$ is the magnitude of the wave vector $\mathbf{k} = k_x\, \hat{\mathbf{x}} + k_y\, \hat{\mathbf{y}} + k_z\, \hat{\mathbf{z}}$ associated to the propagation direction of a wave.

2.1.2 The paraxial wave equation

A paraxial approximation to Eqs. (2.6) needs to be treated with care since, as detailed by Lax *et al.* [1] it might lead to inconsistencies with the Maxwell's equations (for example in using a linearly polarized electric field along a single direction of the form $\mathbb{E}(\mathbf{r}, t) = E_x(\mathbf{r}, t)\, \hat{\mathbf{x}}$). These inconsistencies motivated Lax and co-workers to pioneer the search for rigorous solutions to the exact Maxwell equations [Eqs. (2.1)], formulating a general, even thought complicated, procedure [1]. Few years later, Davis was able to simplify this procedure by taking the vector potential $\mathbb{A}(\mathbf{r}, t)$ to be linearly polarized in the transverse plane rather than the electric field $\mathbb{E}(\mathbf{r}, t)$ [2].

We start by noticing that Eq. (2.3c) directly implies the existence of a vector $\mathbb{A}(\mathbf{r}, t)$ such that,

$$\mathbb{B}(\mathbf{r}, t) = \nabla \times \mathbb{A}(\mathbf{r}, t). \tag{2.7}$$

Upon substitution of Eq. (2.7) into Eq. (2.3b) we arrive to

$$\nabla \times \left(\mathbb{E}(\mathbf{r}, t) + \frac{\partial \mathbb{A}(\mathbf{r}, t)}{\partial t} \right) = 0, \tag{2.8}$$

which is a direct implication of the existence of scalar potential $\Phi(\mathbf{r}, t)$ that satisfies

$$\nabla \Phi(\mathbf{r}, t) = -\left(\mathbb{E}(\mathbf{r}, t) + \frac{\partial \mathbb{A}(\mathbf{r}, t)}{\partial t} \right), \tag{2.9}$$

or equivalently,

$$\mathbb{E}(\mathbf{r}, t) = -\frac{\partial \mathbb{A}(\mathbf{r}, t)}{\partial t} - \nabla \Phi(\mathbf{r}, t). \tag{2.10}$$

After substituting Eqs. (2.7) and (2.10) into Eq. (2.3d) we arrive to

$$\nabla \times \nabla \times \mathbb{A}(\mathbf{r}, t) = \mu_0\epsilon_0 \frac{\partial}{\partial t} \left(-\nabla \Phi(\mathbf{r}, t) - \frac{\partial \mathbb{A}(\mathbf{r}, t)}{\partial t} \right). \tag{2.11}$$

Using again $\nabla \times (\nabla \times \mathbf{F}) = \nabla(\nabla \cdot \mathbf{F}) - \nabla^2 \mathbf{F}$, the above equation can be written as,

$$\nabla(\nabla \cdot \mathbb{A}(\mathbf{r}, t)) - \nabla^2 \mathbb{A}(\mathbf{r}, t) = \mu_0\epsilon_0 \nabla \left(\frac{\partial \Phi(\mathbf{r}, t)}{\partial t} \right) - \mu_0\epsilon_0 \frac{\partial^2 \mathbb{A}(\mathbf{r}, t)}{\partial t^2} \tag{2.12}$$

from which, after rearranging terms, we can obtain

$$\nabla^2\mathbb{A}(\mathbf{r},t) - \mu_0\epsilon_0\frac{\partial^2\mathbb{A}(\mathbf{r},t)}{\partial t^2} - \nabla\left(\nabla\cdot\mathbb{A}(\mathbf{r},t) + \mu_0\epsilon_0\frac{\partial\Phi(\mathbf{r},t)}{\partial t}\right) = 0. \tag{2.13}$$

At this point, it is convenient to use the Lorentz gauge defined as

$$\nabla\cdot\mathbb{A}(\mathbf{r},t) = -\mu_0\epsilon_0\frac{\partial\Phi(\mathbf{r},t)}{\partial t}. \tag{2.14}$$

Substitution of Eq. (2.14) into Eq. (2.13) leads to the wave equation for the vector potential $\mathbb{A}(\mathbf{r},t)$ given by

$$\nabla^2\mathbb{A}(\mathbf{r},t) - \frac{1}{c^2}\frac{\partial^2\mathbb{A}(\mathbf{r},t)}{\partial t^2} = 0. \tag{2.15}$$

An analogous expression for the scalar potential Φ can be obtained by inserting Eq. (2.10) into Eq. (2.3a) and using the Lorentz gauge [Eq. (2.14)], which has the form,

$$\nabla^2\Phi - \frac{1}{c^2}\frac{\partial^2\Phi(\mathbf{r},t)}{\partial t^2} = 0 \tag{2.16}$$

In a similar way to the previous section, we assume that the vector potential $\mathbb{A}(\mathbf{r},t)$ has the form,

$$\mathbb{A}(\mathbf{r},t) = \frac{1}{\sqrt{2\pi}}\int_{-\infty}^{\infty}\mathbf{A}(\mathbf{r},\omega)\exp[-i\omega t]d\omega. \tag{2.17}$$

After inserting Eq. (2.17) into Eq. (2.16) we arrive to Helmholtz equation for the vector potential $\mathbb{A}(\mathbf{r},t)$

$$\nabla^2\mathbf{A}(\mathbf{r},\omega) + k^2\mathbf{A}(\mathbf{r},\omega) = 0. \tag{2.18}$$

If we use Eqs. (2.10) and (2.14) we can express the electric field in terms of the vector potential as,

$$\mathbb{E}(\mathbf{r},t) = i\omega\mathbf{A}(\mathbf{r},t) + \frac{ic^2}{\omega}\nabla\left[\nabla\cdot\mathbb{A}(\mathbf{r},t)\right]. \tag{2.19}$$

The scalar Helmholtz equation

It is possible to obtain a scalar form of Eq. (2.18) by choosing a unitary constant polarization vector $\hat{\mathbf{e}}$ in the plane perpendicular to the propagation axis, this is,

$$\mathbf{V}(\mathbf{r}) = \hat{\mathbf{e}}U(\mathbf{r}), \tag{2.20}$$

where $\mathbf{V}(\mathbf{r})$ can be the vector potential $\mathbf{A}(\mathbf{r})$, the electric field $\mathbf{E}(\mathbf{r})$ or the the magnetic induction $\mathbf{B}(\mathbf{r})$ and $U(\mathbf{r})$ is a scalar function. Whit this ansatz, Eq 2.18 becomes

$$\nabla^2U(\mathbf{r}) + k^2U(\mathbf{r}) = 0, \tag{2.21}$$

which is known as the scalar Helmholtz equation.

The paraxial approximation

We are finally ready to find a paraxial approximation to the scalar wave equation [Eq. (2.21)]. Within the context of geometric optics, we say that a ray is paraxial if its slope is small, this is, $tan(\theta) \approx \theta$, where θ is the angle of inclination with respect to the optical axis. In the case of optical waves, a paraxial light beam is formed mainly of plane waves that are paraxial to the propagation direction of the beam. Therefore, the largest component of the wavevector **K** lies along the propagation axis, lets say the z direction. Now, a solution to the scalar Helmholtz Eq. (2.21) can be proposed to explicitly depend on the phase factor $\exp[-ikz]$, this is,

$$U(\mathbf{r}) = u(\mathbf{r})\exp[-ikz] \tag{2.22}$$

Here $u(\mathbf{r})$ is an amplitude distribution. On substituting Eq. (2.22) into Eq. (2.21) we find a partial differential equation for the amplitude distribution $u(\mathbf{r})$ defined by,

$$\nabla_T^2 u + \frac{\partial^2 u}{\partial z^2} - 2ik\frac{\partial u}{\partial z} = 0, \tag{2.23}$$

where ∇_T^2 is the transverse Laplace operator, computed in the plane perpendicular to the propagation axis. If the profile is slowly varying with z, the second derivative is much smaller than the first derivative multiplied by the wavenumber. Simultaneously, the transverse variation is larger that the second derivative. This is expressed mathematically as,

$$\frac{\partial^2 u}{\partial z^2} << k\frac{\partial u}{\partial z} \qquad \text{and} \qquad \frac{\partial^2 u}{\partial z^2} << \nabla_T^2 u$$

respectively. In essence, neglecting the second-order derivative with respect to z constitutes the paraxial approximation and lead us to the well known paraxial wave equation,

$$\nabla_T^2 u - 2ik\frac{\partial u}{\partial z} = 0. \tag{2.24}$$

2.2 Solutions to the paraxial wave equation

The paraxial approximation to the wave equation can hold solutions in different coordinate systems. Some of these solutions are of interest to us because they represent one of our principal tools. In this section, we first describe solutions that arise naturally in Cartesian coordinates, more specifically, the Gaussian and Hermite-Gaussian modes. These solutions are the first supported naturally by a laser cavity. Two more sets of solutions, that appear naturally in cylindrical coordinates, will be described afterwards: Laguerre-Gaussian (LG) and Bessel beams(BB), which are good examples of ring-shaped beams endowed with Orbital Angular momentum (OAM).

2.2.1 Solutions in Cartesian coordinates

Gaussian beam

The Gaussian beam has been of great relevance since the invention of the laser because this is the lowest order that a laser cavity can support. Gaussian beams are also commonly used as the input beam to produce new beams with exotic phases and amplitudes, a topic that will be discussed in detail in section 2.4. The method followed to derive the Gaussian beam is to propose a trial solution to the paraxial wave equation [Eq. (2.24)] of the form,

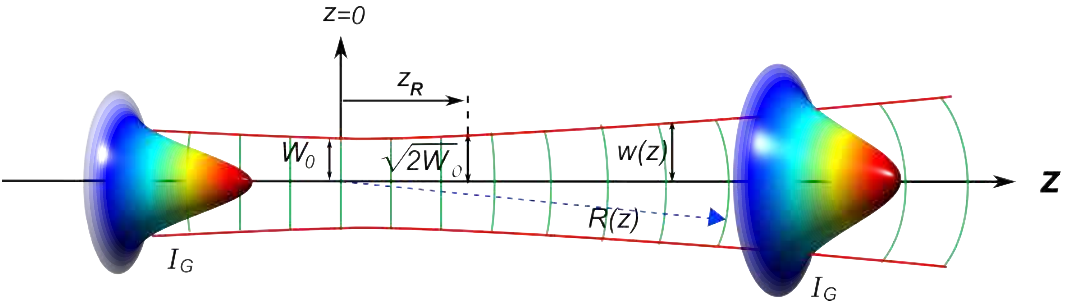

Figure 2.1: The Gaussian beam is one of the simplest solutions to the paraxial wave equation. It represents a paraboloidal wave with wave front radius of curvature $R(z)$ and a beam width $W(z)$.

$$G(\mathbf{r}) = A \exp\left[-ik\frac{\rho^2}{2q(z)}\right]\exp[-ip(z)], \tag{2.25}$$

where $\rho^2 = x^2 + y^2$ and the functions $q(z)$ and $p(z)$ are two unknown functions that can be determined by substituting the trial solution [Eq. (2.25)] into the paraxial wave equation (see for example [3]). The solution we arrive takes the form,

$$G(\mathbf{r}) = \frac{AW_0}{W(z)}\exp\left[-\frac{\rho^2}{W^2(z)}\right]\exp\left[-ikz - ik\frac{\rho^2}{2R(z)} + i\zeta(z)\right], \tag{2.26}$$

with the following definitions

$$\begin{aligned} W(z) &= W_0\sqrt{1+\left(\frac{z}{z_R}\right)^2}, & W_0 &= \sqrt{\frac{\lambda z_R}{\pi}}, \\ R(z) &= z\left[1+\left(\frac{z_R}{z}\right)^2\right] \quad \text{and} & \zeta(z) &= \arctan\left(\frac{z}{z_R}\right). \end{aligned} \tag{2.27}$$

Equation 2.26 represents a paraboloidal wave with radius of curvature $R(z)$ (Fig. 2.1). $W(z)$, known as the spot size, is the distance from the axis to a point ρ_0, in the transverse plane, where the intensity of the beam falls to $1/e^2$ of its peak value and the amplitude to $1/e$ of its axial value. At $z = 0$, $W(z)$ reaches its minimum value W_0, called the beam waist, where the narrowest point in the beam profile is located. The term z_R is a constant known as the Rayleigh range, it is used to measure the distance over which the beam remains well collimated, this is, with wave fronts nearly plane. The parameter $\zeta(z)$, know as the Gouy phase, indicates that the wavefront acquires an additional phase shift of half a wavelength compared to an ideal plane wave, in passing through the waist. Equation 2.26 is called the fundamental Gaussian beam solution, since its intensity shows a Gaussian dependence on ρ given by,

$$I_G = G(\mathbf{r})^* G(\mathbf{r}) \propto \exp\left[-\frac{\rho^2}{W^2(z)}\right]. \tag{2.28}$$

Hermite-Gaussian beam

The trial solution method can be extended to find the Hermite-Gaussian (HG) modes [3] which is a higher order set of solutions. These set of solutions forms a complete set, this is, any other set of complete solutions can be expressed in terms of HG modes. The procedure to find HG modes involves the proposition of a more general solution, defined as the product of two identical functions

$H_1(x,z)$ and $H_2(y,z)$ modulated by the Gaussian beam, this is,

$$HG(\mathbf{r}) = H_x(x,z)H_y(y,z)\exp\left[-ik\frac{\rho^2}{2q(z)}\right]\exp[-ip(z)], \tag{2.29}$$

$H_x(x,z)$ and $H_y(y,z)$ are two unknown functions with the same mathematical form. In order to find their explicit form, it is sufficient to find one of the two functions and bring in the other by analogy. The paraxial wave equation in one coordinate has the form,

$$\frac{\partial^2 u(x,z)}{\partial x} - 2ik\frac{\partial u(x,z)}{\partial z} = 0, \tag{2.30}$$

where,

$$u(x,z) = H_x(x,z)\exp\left[-ik\frac{x^2}{2q(z)}\right]\exp[-ip(z)]. \tag{2.31}$$

After inserting Eq. (2.31) into Eq. (2.30) we arrive to a differential wave equation which is very similar to the standard differential equation for the Hermite polynomials $H_n(x)$ defines as,

$$H_n''(x) - 2xH_n' + 2nH_n = 0, \tag{2.32}$$

from which $H_x(x,z)$ is found to be,

$$H_x = \left(\frac{2}{\pi}\right)^{\frac{1}{4}}\sqrt{\frac{1}{2^n W(z) n!}}\exp\left[i\left(m+\frac{1}{2}\right)\zeta(z)\right]H_n\left[\frac{\sqrt{2}x}{W(z)}\right]$$
$$\exp\left[\frac{-x^2}{W^2(z)}\right]\exp\left[\frac{-ikx^2}{2R(z)}\right]\exp[-ikz], \tag{2.33}$$

where $H_n(x)$ are the Hermite polynomials of order n. $H_y(x,z)$ has exactly the same form. The final expression for $u_{HG}(x,y,z)$ is therefore

$$HG(\mathbf{r})_{nm} = \frac{1}{W(z)}\sqrt{\frac{2^{-(n+m-1)}}{\pi n! m!}}\exp\left[i(n+m+1)\zeta(z)\right]$$
$$H_n\left[\frac{\sqrt{2}x}{W(z)}\right]H_m\left[\frac{\sqrt{2}y}{W(z)}\right]\exp\left[-\frac{\rho^2}{W^2(z)}\right]\exp\left[\frac{-ik\rho^2}{2R(z)}\right]\exp[-ikz]. \tag{2.34}$$

The intensity profile of some of the first modes is shown in figure 2.2. Notice that HG_{00} coincides with the Gaussian beam discussed in the previous section. These set of solutions are called the Hermite-Gaussian modes because they involve a product of Hermite and Gaussian functions. They can also be supported by laser cavities, which can be accomplished by breaking the rotational symmetry of the cavity to suppress the fundamental HG_{00} mode.

2.2.2 Solutions in cylindrical coordinates

Laguerre-Gaussian modes

One of the first sets of solutions that arise naturally in cylindrical coordinates are the Laguerre-Gaussian modes. They are of special interest to us because these modes were used in some of the experiments we carried out. In order to derive these set of solutions, we need to express the paraxial

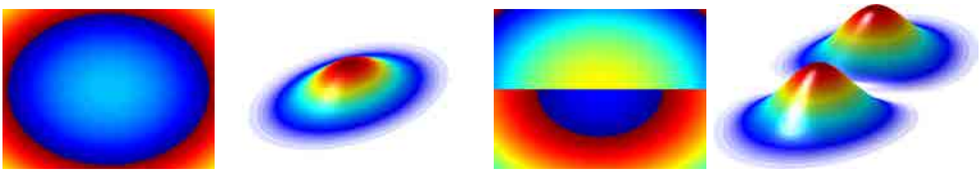

(a) HG_{00} (Phase) (b) HG_{00} (Amplitude) (c) HG_{01} (Phase) (d) HG_{01} (Amplitude)

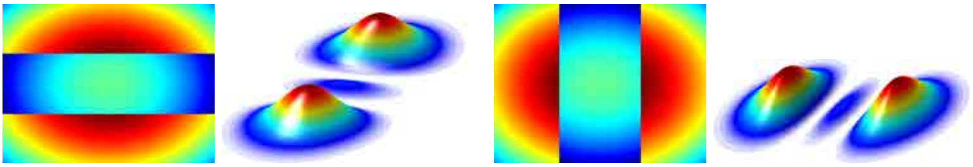

(e) HG_{02} (Phase) (f) HG_{02} (Amplitude) (g) HG_{20} (Phase) (h) HG_{20} (Amplitude)

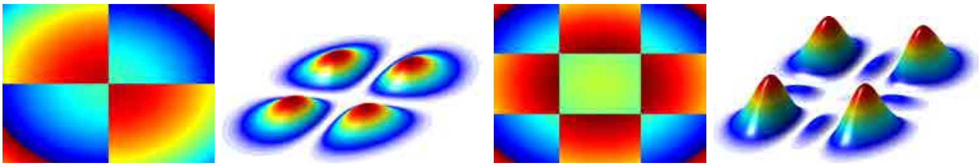

(i) HG_{11} (Phase) (j) HG_{11} (Amplitude) (k) HG_{21} (Phase) (l) HG_{22} (Amplitude)

Figure 2.2: Theoretical phase and intensity plots of Hermite-Gaussian modes.

wave equation [Eq.(2.24)] in the cylindrical coordinates system. This can be done by using the Laplace operator expressed in these coordinates system as

$$\nabla^2\Psi = \frac{1}{\rho}\frac{\partial}{\partial\rho}\left(\rho\frac{\partial\Psi}{\partial\rho}\right) + \frac{1}{\rho^2}\frac{\partial^2\Psi}{\partial\phi^2}. \tag{2.35}$$

Equation 2.24 takes now the form

$$\frac{1}{\rho}\frac{\partial}{\partial\rho}\left[\rho\frac{\partial u}{\partial\rho}\right] + \frac{1}{\rho^2}\frac{\partial^2 u}{\partial\phi^2} - 2ik\frac{\partial u}{\partial z} = 0. \tag{2.36}$$

One simple trial solution to Eq.(2.36 involving the product of two independent functions, one for the radial coordinate and another for the azimuthal coordinate modulated by a Gaussian envelope, this is,

$$LG(\mathbf{r}) = L\left[\frac{\rho}{W(z)}\right]\exp[-ip(z)]\exp\left[k\frac{\rho^2}{2(q(z))}\right]\exp[i\ell\phi]. \tag{2.37}$$

In this case, after inserting Eq. (2.37) into Eq. (2.36) one finds the standard differential equation for the Laguerre polynomials $L(x)$ of the form

$$xL''(x) + (\alpha + 1 - x)L(x)'' + nL(x) = 0, \tag{2.38}$$

whose solutions are the associated Laguerre polynomials L_p^ℓ of radial index p and axial index ℓ

$$L\left[\frac{\rho}{W(z)}\right] = \left(\frac{\sqrt{2}\rho}{W}\right)^\ell L_p^\ell\left(\frac{\sqrt{2}\rho^2}{W^2}\right). \tag{2.39}$$

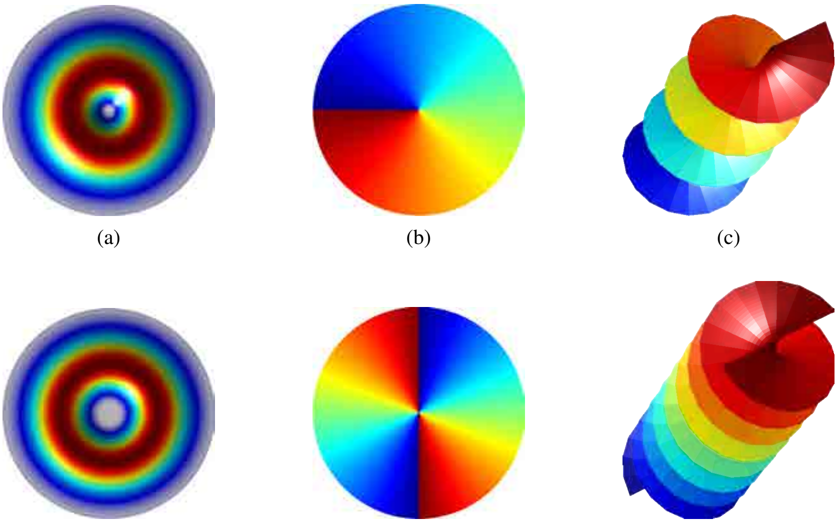
(a) (b) (c)

(d) (e) (f)

Figure 2.3: The transverse intensity profile of an LG beam with $p = 0$ for (a) $\ell = 1$ and (d) $\ell = 2$ winding numbers features a doughnut shaped intensity profile. (b) and (e) are their respective phases in the transverse plane. (c) and (f) represent their respective helicoidal wavefront upon propagation.

The solution can be finally expressed as,

$$LG_p^\ell(\mathbf{r}) = \sqrt{\frac{2p!}{\pi(\ell+p)!}}\left[\frac{\sqrt{2}\rho}{W(z)}\right]^\ell L_p^\ell\left[\frac{2\rho^2}{W^2(z)}\right]\frac{\exp[i(2p+\ell+1)\zeta(z)]}{W(z)} \exp\left[-\frac{\rho^2}{W^2(z)}\right]\exp\left[\frac{-ik\rho^2}{2R(z)}\right]\exp[-i\ell\phi], \quad (2.40)$$

$W(z)$, $R(z)$ and ζ are the same as in Eqs. (2.27). In the transverse plane LG modes with $p = 0$ and $\ell \neq 0$, features an azimuthally varying phase with an axial singularity where the phase is not well defined, as result the intensity profile shows a dark core at the center of the beam. For $\ell = 1$ the phase fronts are simple screw thread, whereas for $\ell = 2$ the phase fronts evolves in the form of a double helix (see Fig. 2.3).

For $p > 0$, the modes are multiringed with $p + 1$ radial nodes. Figure 2.4 shows the intensity of some of the first modes. Notice that the mode LG_{00} is the same as the mode HG_{00}. One of the most interesting features of these set of solutions is the phase term $\exp[i\ell\phi]$ associated to an orbital angular momentum along the propagation direction, a property that will be discussed in section 2.3

Bessel beams

The full Helmholtz equation [Eq. (2.21)] supports a class of solutions that arises also naturally in cylindrical coordinates. These solutions are described in terms of the Bessel functions from which the name of Bessel beams has been coined. The transverse profile of these solutions is invariant upon propagation and are known to be a class of diffraction-free beams [4]. Theoretically, Bessel beams features an infinitely extended transverse profile but, under laboratory conditions the realization of such beams is limited by the physical requirement of a finite aperture and therefore they will show diffraction effects.

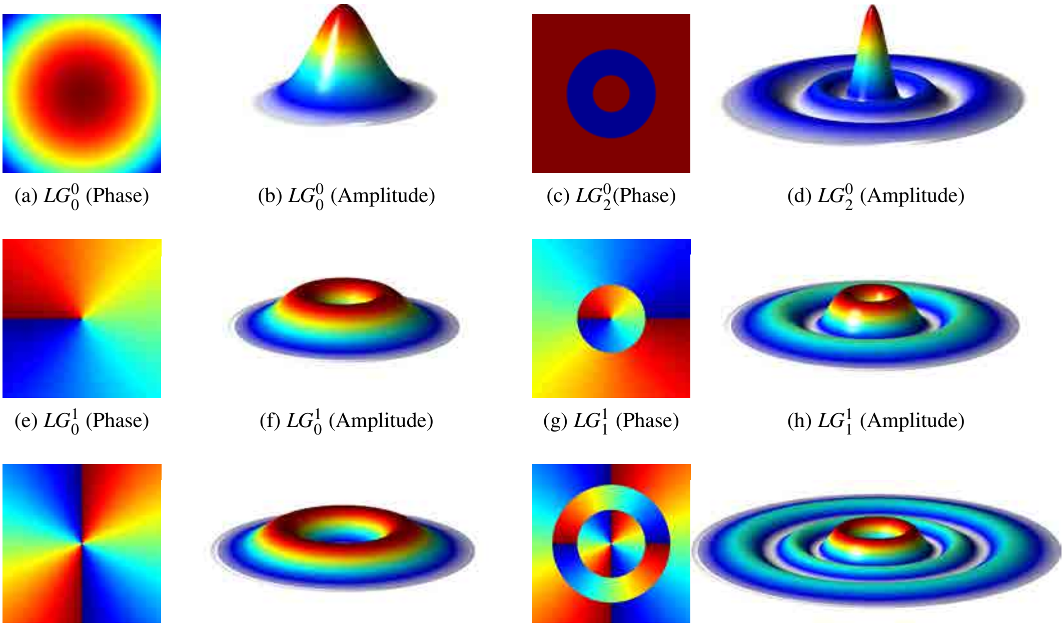

(a) LG_0^0 (Phase) (b) LG_0^0 (Amplitude) (c) LG_2^0(Phase) (d) LG_2^0 (Amplitude)

(e) LG_0^1 (Phase) (f) LG_0^1 (Amplitude) (g) LG_1^1 (Phase) (h) LG_1^1 (Amplitude)

(i) LG_0^2 (Phase) (j) LG_0^2 (Amplitude) (k) LG_2^2 (Phase) (l) LG_2^2 (Amplitude)

Figure 2.4: Theoretical phase and intensity plots of Laguerre-Gaussian modes.

To derive the explicit form of the Bessel beams, a trial solutions formed by the product of independent functions, each one depending on only one variable, is proposed. This is,

$$U = f(k_T\rho)\exp[-ik_z z]\exp[i\ell\phi], \tag{2.41}$$

where k_T is the wave vector in the transverse plane and k_z is the wave vector along the propagation direction obeying the relation $k^2 = k_T^2 + k_z^2$.

The full Helmholtz equation [Eq. (2.23)] can be rewritten in cylindrical coordinates as

$$\frac{1}{\rho}\frac{\partial}{\partial\rho}\left[\rho\frac{\partial u}{\partial\rho}\right] + \frac{1}{\rho^2}\frac{\partial^2 u}{\partial\phi^2} + \frac{\partial^2 u}{\partial z^2} - 2ik\frac{\partial u}{\partial z} = 0. \tag{2.42}$$

After introducing Eq. (2.41) into Eq. (2.42) we arrive to the partial differential equation

$$(\rho k_T)^2\frac{\partial^2 f}{\partial\rho^2} + (\rho k_t)\frac{\partial f}{\partial\rho} + [(k_T\rho)^2 - \ell^2]f = 0, \tag{2.43}$$

which has the same form of the Bessel differential equation, whose solution are the Bessel polynomials $J_m(x)$. Hence, in cylindrical coordinates, a solution to the full Helmholtz equation has the form

$$B(\mathbf{r}) = J_\ell(k_T\rho)\exp[ik_z z]\exp[-ikz]\exp[i\ell\phi]. \tag{2.44}$$

Bessel beams which forms also a complete set of solutions have the same azimuthal phase factor $\exp[i\ell\phi]$ as the Laguerre-Gaussian modes, and hence carry also orbital angular momentum. Some of the first few modes are shown in figure 2.5.

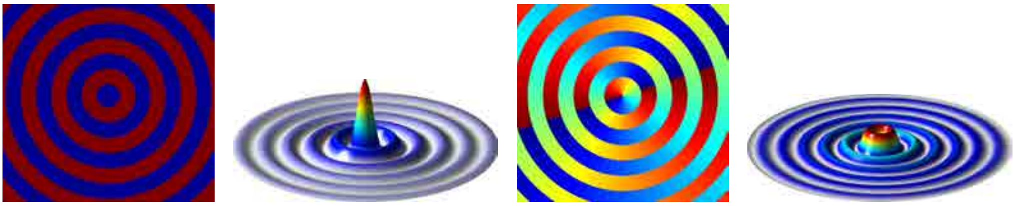

(a) B_0 (Phase) (b) B_0 (Amplitude) (c) B_1 (Phase) (d) B_1 (Amplitude)

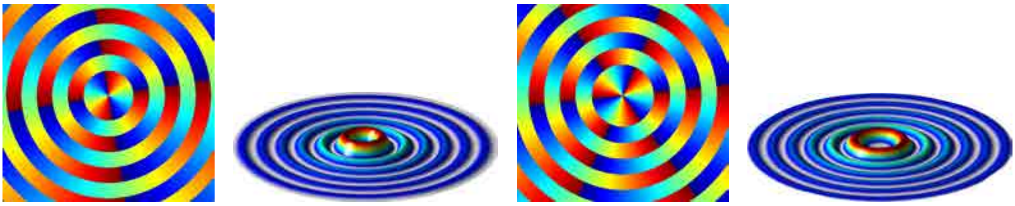

(e) B_2 (Phase) (f) B_2 (Amplitude) (g) B_3 (Phase) (h) B_3 (Amplitude)

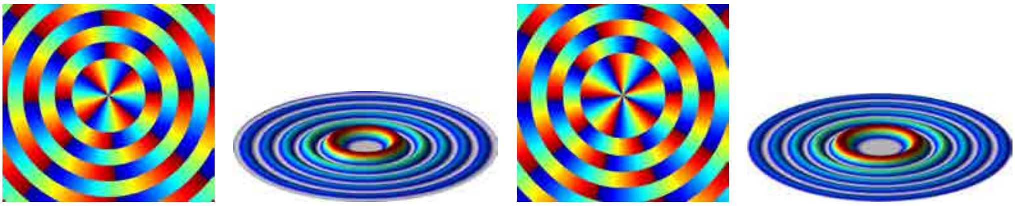

(i) B_4 (Phase) (j) B_4 (Amplitude) (k) B_5 (Phase) (l) B_5 (Amplitude)

Figure 2.5: Theoretical phase and intensity profiles of Bessel modes

2.3 Angular momentum of Light

Rotating light beams carry angular momentum (AM) as they propagate in free space. This AM is associated with the circulatory flows of energy in the plane perpendicular to the propagation axis. Two sources of AM have been identified, the first one related to circular or elliptic polarization, known as spin angular momentum (SAM). The second one known as Orbital Angular Momentum (OAM) is attributed to a macroscopic energy circulation caused by the beam spatial phase distribution and might be several times larger than the SAM. In general, a separation into spin and orbital angular momentum is not possible, however within the paraxial approximation this separation become possible. A brief historical introduction about AM will be given next, followed by a description of the separation of AM into SAM and OAM.

2.3.1 Historical introduction

The study of optical angular momentum can be traced back to 1873 when Maxwell published his famous treatise on electromagnetism. Here, his ideas of the electromagnetic field and its mechanical properties were first expressed in clear and consistent form. Few years later (in 1898), based on Maxwell equations, Sadovsky predicted that the light with circular and elliptic polarization exerts a rotatory action upon material objects [5]. The same facts became commonly known after Poynting rediscovery (in 1909) of these predictions [6]. Poynting demonstrated that an amount $E\lambda/2\pi$ of angular momentum would be transmitted through a plane per unit time, per unit area. Here, E is the energy per unit volume and λ the wavelength. If we associate an energy $\hbar\omega$ to each photon crossing the surface, we obtain that each circularly polarized photon should carry an angular momentum $\hbar$. Poynting also provided with an experimental proposal to measure the angular momentum associated with Circularly Polarized Light (CPL). He believed that when CPL passes through a large number of suspended quarter-wave plates, a conversion from circular polarization to linear polarization would occur and therefore a well defined amount of angular momentum would be transferred to the suspension. His prediction was confirmed in 1939 by Beth [7] who, in a very clever way, used a single quarter wave plate along with a mirror to sent the light back through the plate enhancing the torque on the suspension.

Even though helically phased light fields have been under study for a number of years, the realization that they might carry orbital angular momentum was established not very long ago, in 1992, after the seminal paper by Allen *et al.* [8]. In this paper, it was predicted that any beam with amplitude distribution $u(r, \phi, z) = u_0(r, z)\exp[i\ell\phi]$ carries, besides the angular momentum associated to the polarization of light, an orbital contribution associated to the phase structure of the beam. They did not only established a theoretical framework for the Orbital Angular Momentum (OAM) but also proposed an optical system to transform Hermite-Gaussian (HG) into Laguerre-Gaussian (LG) modes and *vice versa*. Moreover, they proposed an experiment to measure the mechanical torque induced by the transfer of OAM associated with such a transformation. One year later, in 1993, Beijersbergen *et al.* [9] also presented a design of a mode converter to transform HG modes into LG and predicted that beams with an azimuthal dependence $\exp[i\ell\phi]$ would carry an amount $L = \ell\hbar$ of OAM per photon. This new form of angular momentum has started new lines of research and found numerous applications.

2.3.2 Mathematical description

Although the separation of angular momentum of light along the propagation direction into a spin part and an orbital part can not be done in general, such separation is possible and physically meaningful in the paraxial limit. A natural way to compute this angular momentum is via the flux of angular momentum, which is valid to both, the paraxial and the non-paraxial regime. A quantification of the flux of angular momentum can be given in terms of the Poynting vector $\mathbb{S}$ (see for example [10]), which is defined as

$$\mathbb{S}(\mathbf{r}, t) = \frac{1}{\mu_0}\mathbb{E}(\mathbf{r}, t) \times \mathbb{B}(\mathbf{r}, \mathbf{t}). \tag{2.45}$$

The Poynting vector measures the energy flux density at any point in space, *i.e.*, the direction and magnitude of energy per unit area per unit time transported by the fields. In free space, it is related to the local value of the linear $\mathbf{p}$ an angular $\mathbf{j}$ momentum densities via the following relations,

$$\mathbf{j} = \mathbf{r} \times \mathbf{p} \tag{2.46}$$

$$\mathbf{p} = \frac{\mathbb{S}}{c^2} = \epsilon_0\mathbb{E}(\mathbf{r}, t) \times \mathbb{B}(\mathbf{r}, \mathbf{t}), \tag{2.47}$$

where c is the light speed in vacuum. The total linear $\mathbf{P}$ and angular $\mathbf{J}$ momentum per unit length may be found by integrating Eqs. (2.48) and (2.49) over the area dA of the beam in a plane perpendicular to the propagation direction, this is

$$\mathbf{P} = \int\int \mathbf{p}\, dA \tag{2.48}$$

$$\mathbf{J} = \int\int \mathbf{j}\, dA. \tag{2.49}$$

Equations 2.46 and 2.47 shows that a component of angular momentum along the propagation direction $\hat{\mathbf{z}}$, requires a component of linear momentum in the azimuthal direction. This means, the electromagnetic field must have a component in the direction of propagation $\hat{\mathbf{z}}$. An idealized plane wave of infinite extent has only transverse fields components, hence it carries no angular momentum. For paraxial waves, which comprise a beam of limited radius such as those described in section 2.2, this is not the case and a z-component of the electromagnetic field can arise in two distinct ways. One of these gives rise to the spin angular momentum and the other to the orbital angular momentum. In finding these we need to compute the real part of the time averaged Poynting vector, defined as [8]

$$\langle \mathbb{S}(\mathbf{r},t)\rangle = \frac{1}{2\mu_0}\{\mathbb{E}(\mathbf{r},t)\times\mathbb{B}^*(\mathbf{r},\mathbf{t}) + \mathbb{E}^*(\mathbf{r},t)\times\mathbb{B}(\mathbf{r},\mathbf{t})\}, \tag{2.50}$$

where $\mathbb{E}^*$ and $\mathbb{B}^*$ denote the complex conjugate of $\mathbb{E}$ and $\mathbb{B}$ respectively.

We first compute $\mathbb{E}(\mathbf{r},t)$ and $\mathbb{B}(\mathbf{r},t)$ from a vector potential of the form

$$\mathbb{A}(\mathbf{r},t) = u(\mathbf{r})\exp[ikz - i\omega t]\ \hat{\mathbf{n}}, \tag{2.51}$$

where $\hat{\mathbf{n}} = \alpha\,\hat{\mathbf{x}} + \beta\,\hat{\mathbf{y}}$ represents the unitary polarization vector perpendicular to the propagation direction $\hat{\mathbf{z}}$.

Upon using Eqs. (2.7) and (2.19) we find the magnetic and electric fields to be

$$\mathbb{B}(\mathbf{r},t) = ik\left\{\left[u(\mathbf{r}) - \frac{i}{k}\frac{\partial u(\mathbf{r})}{\partial z}\right]\hat{\mathbf{z}}\times\hat{\mathbf{n}} + \frac{i}{k}\ \hat{\mathbf{n}}\times\nabla_T u(\mathbf{r})\right\}\exp[ikz - i\omega t], \tag{2.52}$$

and

$$\mathbb{E}(\mathbf{r},t) = i\omega\left\{u(\mathbf{r})\ \hat{\mathbf{n}} + \frac{i}{k}\ \hat{\mathbf{n}}\cdot\nabla u(\mathbf{r})\ \hat{\mathbf{z}} + \frac{1}{k^2}\ [\ \hat{\mathbf{n}}\cdot\nabla]\ \nabla u(\mathbf{r})\right\}\exp[ikz - i\omega t]. \tag{2.53}$$

In the paraxial approximation, second partial derivatives might be ignored as well as variations of u along the propagation direction $\hat{\mathbf{z}}$, this is, $\partial u/\partial z << u$ so that Eqs. (2.52) and (2.53) take now the form

$$\mathbf{B}(\mathbf{r}) = ik\left\{u(\mathbf{r})\ \hat{\mathbf{z}}\times\hat{\mathbf{n}} + \frac{i}{k}\ \hat{\mathbf{n}}\times\nabla_T\ u(\mathbf{r})\right\}\exp[ikz], \tag{2.54}$$

and

$$\mathbf{E}(\mathbf{r}) = i\omega\left\{u(\mathbf{r})\ \hat{\mathbf{n}} + \frac{i}{k}[\ \hat{\mathbf{n}}\cdot\nabla u(\mathbf{r})]\ \hat{\mathbf{z}}\right\}\exp[ikz], \tag{2.55}$$

where we have drop the dependence on t for the sake of brevity. After inserting Eqs. (2.54) and (2.55) into the time-averaged Poynting vector [Eq. [2.50)], we obtain

$$\langle\mathbf{s}\rangle = \frac{\omega k}{2\mu_0}\left\{2|u|^2\ \hat{\mathbf{z}} + \frac{i}{k}\left[u\nabla u^* - u^*\nabla u\right] + \frac{i}{k}\left[\hat{\mathbf{n}}(\hat{\mathbf{n}}^*\cdot\nabla|u|^2) - \hat{\mathbf{n}}^*(\hat{\mathbf{n}}\cdot\nabla|u|^2)\right]\right\}, \tag{2.56}$$

where explicit dependence of $\mathbf{r}$ in $u(\mathbf{r})$ has been drop. We can further simplified Eq. (2.56) by substituting $\hat{\mathbf{n}} = \alpha\ \hat{\mathbf{x}} + \beta\ \hat{\mathbf{y}}$. Hence,

$$\langle\mathbf{s}\rangle = \frac{\omega k}{2\mu_0}\left\{2|u|^2\ \hat{\mathbf{z}} + \frac{i}{k}\left[u\nabla u^* - u^*\nabla u\right] + \frac{i}{k}\left[(\alpha\beta^* - \alpha^*\beta)\nabla|u|^2\times\hat{\mathbf{z}}\right]\right\}. \tag{2.57}$$

Therefore, the time-averaged linear momentum $\langle\mathbf{p}\rangle$ is

$$\langle\mathbf{p}\rangle = \frac{\langle\mathbf{s}\rangle}{c^2} = \omega k\epsilon_0|u|^2\ \hat{\mathbf{z}} + \frac{i\omega\epsilon_0}{2}\left[u\nabla u^* - u^*\nabla u\right] + \frac{i\omega\epsilon_0}{2}\left[(\alpha\beta^* - \alpha^*\beta)\nabla|u|^2\times\hat{\mathbf{z}}\right]. \tag{2.58}$$

The first term of the time-averaged linear momentum is directed along the propagation direction $\hat{\mathbf{z}}$, therefore it has no contribution to the angular momentum. The remaining two terms contain all the contributions to the angular momentum, this is,

$$p_\phi = \frac{i\omega\epsilon_0}{2}\left[u\nabla u^* - u^*\nabla u\right] + \frac{i\omega\epsilon_0}{2}\left[(\alpha\beta^* - \alpha^*\beta)\nabla|u|^2 \times \hat{\mathbf{z}}\right]. \tag{2.59}$$

The time-averaged angular momentum $\langle \mathbf{j} \rangle$ along the direction of propagation $\hat{\mathbf{z}}$ is then,

$$\langle j_z \rangle = \frac{i\omega\epsilon_0}{2}\mathbf{r} \times \left[u\nabla u^* - u^*\nabla u\right] + \frac{i\omega\epsilon_0}{2}\left[(\alpha\beta^* - \alpha^*\beta)\mathbf{r} \times (\nabla|u|^2 \times \hat{\mathbf{z}})\right]. \tag{2.60}$$

The first term, involving a gradient of the field, is related to the orbital angular momentum and the second one, containing the term $\alpha\beta^* - \alpha^*\beta$, is associated to the spin angular momentum. For a linearly polarized paraxial plane wave, $\alpha\beta^* = \alpha^*\beta$ and $(u\nabla u^* - u^*\nabla u)_\phi = 0$ since u does not depend on ϕ. Hence $\mathbf{r} \times (u\nabla u^* - u^*\nabla u)_\phi = 0$, this is, it carries no angular momentum.

Spin angular momentum

For circularly polarized plane waves, the first term in Eq. (2.60) is again zero but, the second term is not. This term can be computed easier in cylindrical coordinates as,

$$\nabla|u|^2 \times \hat{\mathbf{z}} = -\hat{\mathbf{z}} \times \frac{\partial|u|^2}{\partial\rho}\hat{\rho} = -\frac{\partial|u|^2}{\partial\rho}\hat{\phi}. \tag{2.61}$$

Therefore, the time-averaged angular momentum arising from the fact that light is circularly polarized, denoted as s, becomes

$$s = \frac{-\epsilon_0\omega\rho\sigma}{2}\frac{\partial|u|^2}{\partial\rho}, \tag{2.62}$$

where $\sigma = \alpha\beta^* - \alpha^*\beta$. The total angular momentum along the direction of propagation, after integration by parts over the ρ coordinate is

$$S = \frac{-\epsilon_0\omega\sigma}{2}\int\int\frac{\rho\partial|u|^2}{\partial\rho}\rho d\rho d\phi = -\epsilon_0\omega\sigma\left[\int\rho^2|u|^2 d\phi - 2\int\int|u|^2\rho d\rho d\phi\right]. \tag{2.63}$$

A further simplification can be done by noticing that $\rho^2|u|^2 \to 0$ as $\rho \to \infty$. This is,

$$S = \epsilon_0\omega\sigma\left[\int\int|u|^2\rho d\rho d\phi\right]. \tag{2.64}$$

The angular momentum per photon can be estimated by computing the ratio of the angular momentum to the energy per unit length, this is, $S/\mathcal{W}$. The energy per unit time is given by

$$\mathcal{W} = \int\int c\mathbf{p}_z = c\omega k\epsilon_0\int\int|u|^2\rho d\rho d\phi. \tag{2.65}$$

Hence, the angular momentum carried by each photon is,

$$\frac{S}{\mathcal{W}} = \frac{\epsilon_0\omega\sigma\int\int|u|^2\rho d\rho d\phi}{c\omega k\epsilon_0\int\int|u|^2\rho d\rho d\phi} = \frac{\sigma}{\omega}, \tag{2.66}$$

σ takes the value 1 or -1 depending on the handedness of the circularly polarized light.

Orbital angular momentum

In the presence on an azimuthal phase dependence of the form $\exp[i\ell\phi]$, the term $(u\nabla u^* - u^*\nabla u)_\phi$ in Eq. (2.60) is no longer zero, giving rise to another form of angular moment, known as orbital angular momentum. As mentioned before, optical beams with a phase of the form $\exp[i\ell\phi]$, carries no energy along its center. Therefore the vortex itself carries neither linear momentum nor angular momentum. It is only in the immediate vicinity of the same that the azimuthal phase term occur in helicoidal phase fronts of the optical field (Fig.2.6). The electric and magnetic fields at any point lie in the plane tangent to these helicoidal phase fronts. This means that the local momentum density, $\epsilon_0\vec{E}\times\vec{B}$, is normal to the phase front, hence the momentum density itself follows a helical path along the beam (Fig. 2.6). Orbital angular momentum and optical vortices are often incorrectly used as synonymous though the former may exist without the presence of the second, as demonstrated in 1997 by Courtial *et al.* [11]. In this significant work, it was demonstrated than an elliptical Gaussian beam focused by a cylindrical lens can posses orbital angular momentum without the presence of an optical vortex, since an optical beam can have an azimuthal phase gradient without a nearby phase singularity.

Assuming an amplitude distribution with an azimuthal dependence of the form

$$u(\mathbf{r}) = u_0(\mathbf{r})\exp[i\ell\phi]. \tag{2.67}$$

The second term of Eq. (2.60) related to the polarization will be zero and we are left only with the first term (denoted as l), this is,

$$l = \frac{i\omega\epsilon_0}{2}\mathbf{r}\times\left[u\nabla u^* - u^*\nabla u\right]. \tag{2.68}$$

By introducing Eq. (2.67) into Eq. (2.68) we obtain,

$$l = \epsilon_0\omega\ell|u|^2. \tag{2.69}$$

Hence, the total angular momentum along the direction of propagation is

$$L = \epsilon_0\omega\ell\int\int|u|^2\rho d\rho d\phi. \tag{2.70}$$

After dividing this by the energy per unit length, we finally get

$$\frac{L}{\mathcal{W}} = \frac{\epsilon_0\omega\ell\int\int|u|^2\rho d\rho d\phi}{c\omega k\epsilon_0\int\int|u|^2\rho d\rho d\phi} = \frac{\ell}{\omega}. \tag{2.71}$$

The direction of the OAM is related to the sign of the winding number ℓ. For a beam propagating in the + $\hat{\mathbf{z}}$ axis and a positive winding number $\ell > 0$, the OAM vector will have the same direction as the linear momentum p_z (Fig. 2.7a). If $\ell < 0$, the OAM will have the opposite direction to the linear momentum vector p_z (Fig. 2.7b). If the beam reverses its direction of propagation, and therefore its linear momentum(for instance by being reflected in a perfect mirror) the OAM vector maintains its direction. Hence, for $\ell > 0$ the linear momentum and the OAM vectors will have opposite directions (Fig. 2.7c). On the contrary, if $\ell < 0$ both vectors will point in the same direction [12]. The interference of a OAM beam with a slightly tilted Gaussian with respect to the OAM beam results in a typical fork-like interference pattern that point up or down depending on the sign of the index ℓ.

Finally, in the most general case, when a helical beam (with an azimuthal varying phase) is circularly polarized, neither of the two terms of Eq. (2.60) are zero, giving rise to a total angular momentum

$$\frac{J_z}{\mathcal{W}} = S + L = \frac{\sigma + \ell}{\omega} \tag{2.72}$$

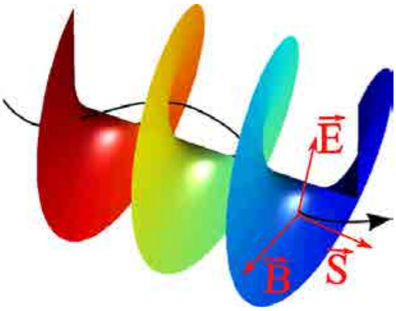

Figure 2.6: In the immediate vicinity of a vortex, the azimuthal phase term produces an optical field with a helicoidal wave front

carried by each photon. This can be interpreted as each photon of energy $\hbar\omega$ carries σ_z quanta of spin angular momentum, associated with the polarization state and ℓ quanta of orbital angular momentum, associated with the spatial distribution of the field. The spin and orbital angular momentum components can also be distinguished according to their different mechanical actions on small absorbing particles: SAM will induce a spin on the particle independent of its position, whereas the OAM will induce a rotation of particle around the beam axis [13, 14].

2.4 Generation of structured light beams

In this section we describe some of the current techniques that are used nowadays to generate optical beams with structured phases, being those endowed with OAM a special case. We classify these techniques as intracavity (Section 2.4.1) and extracavity (Section 2.4.2) generations. The extracavity generation is more flexible since current technology allow us to switch between different modes in fractions of seconds, for example with the help pf Spatial Light Modulators (SLMs) or Digital Micromirror Devices [15].

2.4.1 Intracavity generation

One of the first optical systems capable to generate an optical beam containing a single vortex was developed by Tamm and Weiss [16]. They demonstrated that residual astigmatism of a laser could be controlled such that HG_{10} and HG_{01} modes were frequency degenerate, and coherently interfered to give the hybrid mode TEM^{*}_{10} (a superposition of HG_{10} and HG_{01}). This mode has a transverse intensity pattern with the appearance of a ring donut. Another way to expressed this mode is a superposition of LG^{1}_{0} and LG^{-1}_{0} modes in which, the phases rotates in opposite directions around the vortex. Although these two modes have identical intensity distributions, when passed through a pair of cylindrical lenses they are transformed into a HG_{10} and HG_{01} modes respectively, providing thus a way to identify the sign of the vortex in the original mode. Tam and Weiss used this information to control the coupling back into the laser of a small fraction of the TEM^{*}_{10} amplitude, in such a way the output could be stabilized or switched between LG^{1}_{0} and LG^{-1}_{0} modes. Similar laser systems that emit LG beams directly have been developed including the one by Amiel *et al.*[17] and Okida and Omatsu[18]. The latter demonstrated direct production of high power LG modes and suggested the possibility for the generation of high power beams endowed with OAM in the visible and ultra-violet regimes.

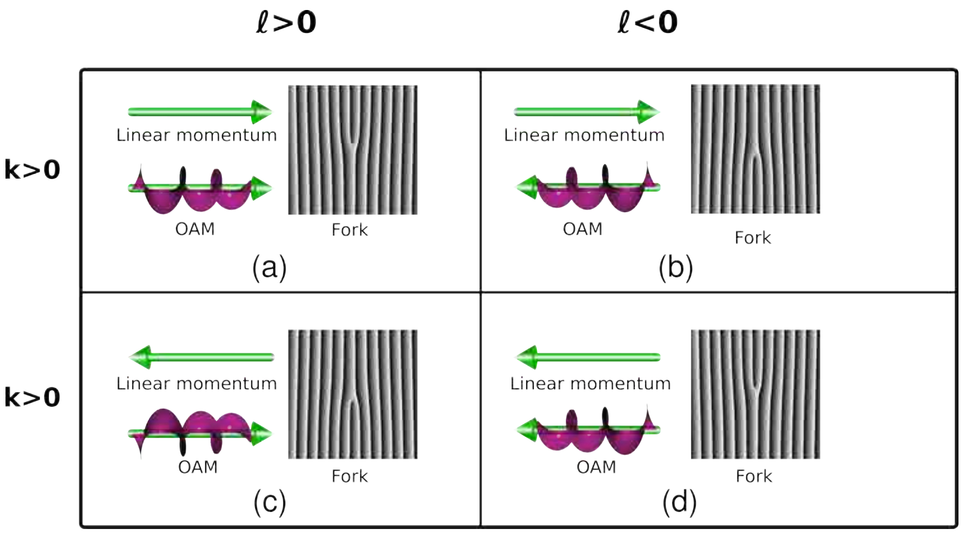

Figure 2.7: The direction of the OAM vector L of a beam propagating along the positive $\hat{\mathbf{z}}$ direction depends on the sign of the winding number ℓ. (a) For $\ell > 0$ both vectors have the same direction, where as for $\ell < 0$ they have opposite direction (b). If the beam changes its direction, for instance by being reflected by a perfect mirror, the direction of L remains the same (c) and (d). The interference of the OAM beam with a slightly tilted Gaussian beam produces a typical fork-like interference pattern that point up or down depending on the sign of the index ℓ.

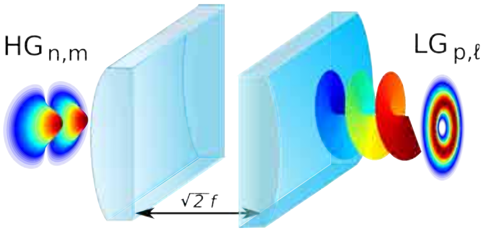

Figure 2.8: An HG_{nm} output of a conventional laser can be transformed by means of a cylindrical lens mode converter into an LG beam of radial number $p = min(n, m)$ and winding number $\ell = \pm|m - n|$, provide, that a separation between the cylindrical lenses is $\sqrt{2}f$.

2.4.2 Extracavity generation

The Cylindrical lenses mode converter

Following the work of Tamm and Weiss on low-order modes, Beijersbergen *et al.* demonstrated an extracavity way to obtain pure LG modes of any order, using a Cylindrical lens mode-converter (see Fig. 2.8) [9]. This device consist of two cylindrical lenses of focal length f separated by $\sqrt{2}f$, it works by direct analogy with the wave-plate for polarization [19, 20]. Cylindrical lens mode-converter can transform suitably oriented Hermite-Gaussian modes into Laguerre-Gaussian modes with $\ell = \pm \mid m - n \mid$ and $p = min(n, m)$.

When the cylindrical lenses are separated by $2f$ then they act as a π-converter and only rotates the Hermite-Gaussian mode. The combination of $\pi/2$ and π-converters provides considerable freedom in manipulating the mode and its orbital angular momentum. The analogy between transverse modes and polarization states extends to a description of modes and their transformation with an equivalent to the Poincaré sphere [21]. The operating principle of mode converters is based on the fact that both HG and LG modes form complete sets of solutions to the paraxial wave equation. Hence any arbitrary paraxial distribution can be described as a superposition of HG or LG terms with the appropriate weighting and phase factors. Therefore, it follows that a LG mode can be described as a superposition of various HG modes and *vice versa*.

In transforming HG into LG modes with cylindrical lenses there are two main problems: firstly, this method requires the generation of a high-order HG beam as an input; secondly, any imperfection in the cylindrical lenses shape or a misalignment in the arrangement leads to a residual astigmatism in the resulting LG mode. As consequence, the intensity pattern loses its circular profile and, upon propagation, higher index vortex splits into multiple vortices [22].

Spiral phase plates

Another approach to generate beams carrying OAM was provided by Woerdman and coworkers through the use of Spiral Phase Plates (SPP) [23, 24]. A SPP is an optical element constructed from a piece of disk-shaped transparent material with homogeneous refractive index n and variable height h. This height increases linearly with the azimuthal angle ϕ, resembling a spiral staircase (fig. 2.9a) and is given by

$$h = h_s \frac{\phi}{2\pi} + h_0, \tag{2.73}$$

where h_s is the step height and h_0 is the base height of the device. The spiraling thickness variation imposes an azimuthal retardation on the optical field (the thicker the plate, the greater the phase shift), creating the helicoidal phase distribution of an optical vortex (fig. 2.9b). The azimuth-dependent optical phase delay is given by

$$\varphi(\phi, \lambda) = \frac{2\pi}{\lambda}\left[\frac{(n-n_0)h_s\phi}{2\pi} + nh_0\right], \tag{2.74}$$

being n_0 the refractive index of the surrounding medium. If the height of the step corresponds to a phase difference of 2π, a SPP inserted in the waist of a Gaussian beam will imprint an azimuthal phase profile of $\exp[i\phi]$, generating a beam with a helicoidal phase endowed with OAM (fig. 2.10). If the step height of a SPP is not an integer multiple of 2π, in addition to the on-axis optical vortex, a radial phase discontinuity is created. Closer inspection reveals that this radial line has an intricate vortex structure. For half-integer step heights, there is a chain of vortices with alternating sign on propagation [25]. These vortex points are simply the intersection of vortex lines with the viewing plane. Such vortex line can be observed by inspecting successive planes [26]. SPP with half-integer step heights have been deliberately fabricated for experiments in quantum optics [23]. In order to be effective, the phase plate must be smooth and accurately shaped to a fraction of the wavelength. Several groups have employed precise micro-machining techniques to manufacture them [27]. However, even if it is successfully produced, it is only applicable to a single wavelength of light and will produce a beam with a specific ℓ value.

A more versatile version is an adjustable spiral phase plate first proposed by Rostchild [28]. They are created by twisting a piece of line-cracked Plexiglas in such a way one tab of the phase plate is

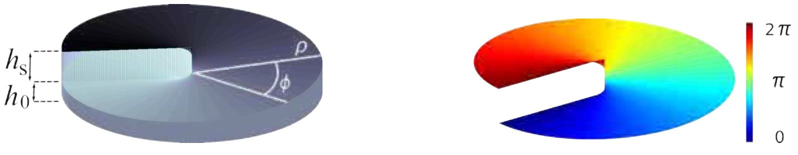

(a) (b)

Figure 2.9: (a)A spiral phase plate and (b) its phase distribution.

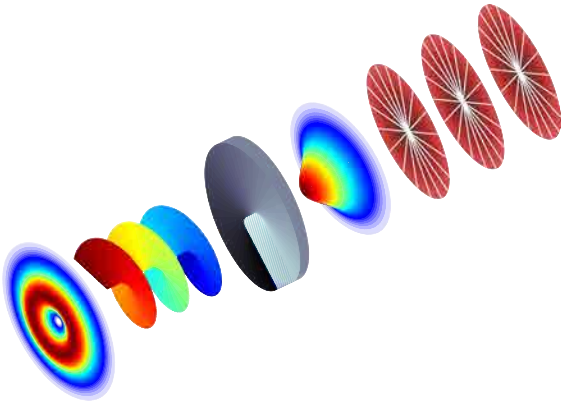

Figure 2.10: A collimated Gaussian beam can be transformed into a helical beam by inserting a spiral phase plate aligned with its optical axis.

directly perpendicular to the incident light, and the other tab is bent at some angle β away from the other. Because of the azimuthally varying tilt around the center of the phase plate, a laser directed to this point will acquire a phase singularity. These phase plates can be used with multiple wavelengths and are able to produce beams within a wide range of topological charges.

Holographic film

The use of diffractive optical components to transform spatially coherent, flat phase beams into beams carrying OAM began to be explored in the early 1990s. Soskin *et al.* discovered that when a diffraction grating is modified to include an edge dislocation at its center, in the form of a fork, an optical singularity appears in the first order diffracted beam [29, 30]. To create this diffracting grating, the interference pattern between a plane wave and the beam one desires to produce is recorded as a hologram on photosensible film. The resulting grating has a "pitchfork" dislocation with a ℓ-value imposed corresponding to the difference between the number of lines above and below the dislocation. Holograms designed to create a beam with $\ell = 1$ and $\ell = 2$ are shown in Fig. 2.11(a) and 2.11(b) respectively. Once constructed, the film can be illuminated by a plane wave to produce a first-order diffracted beam that has both the intensity and phase of the desired beam [29, 31]. This forked design, which has become synonymous of the generation of optical vortices, can be implemented either as an amplitude or phase grating.

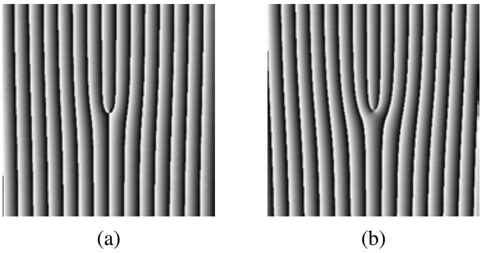

(a) (b)

Figure 2.11: Examples of blazed holograms that create vortex beams with (a) single and (b) double helical wave front.

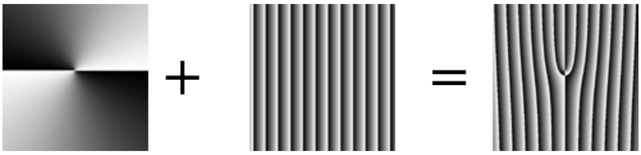
(a)

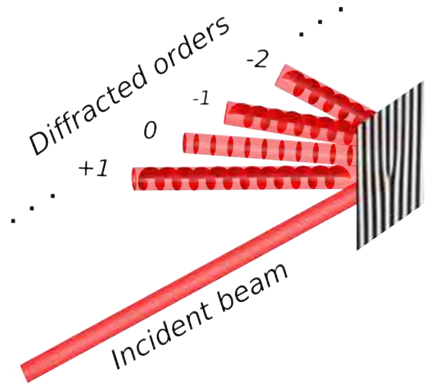

(b)

Figure 2.12: (a) A forked hologram produced by the addition of a blaze grating and the spiraling phase is use to separate modulated light from un-modulated. (b) The use of fork holograms produce several diffracted orders

Spatial light modulators

The big advantage of this approach relies in the current availability of high-quality computed-controlled devices, as is the case of spatial light modulators (SLMs) and Digital Micromirror Devices. Spatial Light Modulators (SLMs) are computer-controlled pixellated liquid crystal devices. SLMs have replaced the holographic film and avoid the experimental derivation of the interference pattern that can be simply computed-calculated and displayed on the device. Holograms calculated in this way allow for the conversion of a well collimated laser beam into any beam with exotic phases and amplitude structures. One of the main advantages of using SLMs is that the encoded pattern can be easily changed with frequencies as high as $60Hz$, so the emerging beam can be adjusted to meet the experimental requirements. The versatility of SLMs for beam shaping has made of this the most popular method to generate almost any exotic beam with application in fields as diverse as optical manipulation and adaptive optics [32, 33]. An issue to deal with when using SLMs is that a considerable percentage of the incoming light does not undergoes a phase modulation. Simply because part of it is reflected at the interface of the SLM but also because another portion is diffracted due to the gaps between the pixels. This un-modulated light overlaps with the phase modulated light. This problem can be overcome easily by adding a blazed grating to the hologram (Fig.2.12) to spatially separate the modulated from the un-modulated light. This also gives rise to higher diffraction orders that propagates at different angles (see Fig2.12b) but with the help of spatial filters we can select the desired order.

q-plates

In 2006 a novel concept for the transformation of spin angular momentum into orbital angular momentum was introduced by Marrucci *et al.* [34]. The process for this conversion was termed spin-to-orbital conversion of angular momentum (STOC). Marruci *et al.* used the fact that in an optically

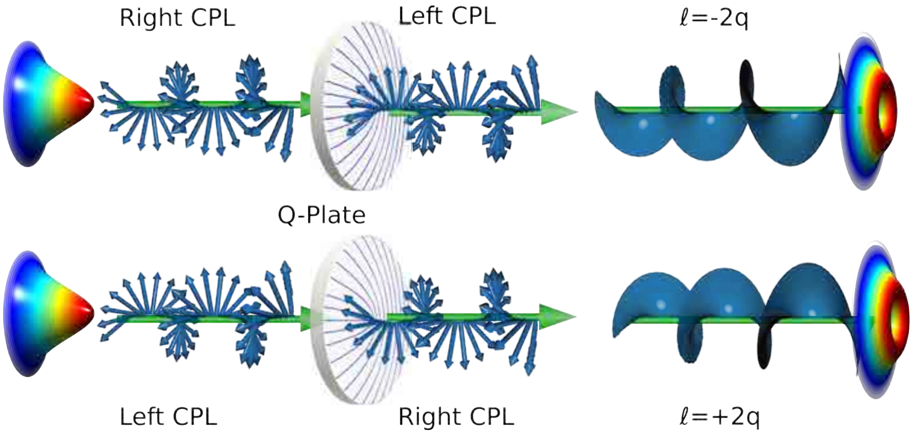

Figure 2.13: A beam with a flat phase impinging on a q-plate can be converted into a helically-phased beam carrying OAM.

anisotropic media only the spin angular momentum of light is transferred to matter, while for inhomogeneous isotropic transparent media only an orbital angular momentum interaction takes place. They discovered that these two mechanisms of light-matter interactions are not independent in a material which is both inhomogeneous and anisotropic and realized that under certain conditions the exchange of spin affects the direction (sign) of the exchange of orbital angular momentum. Moreover, under specific geometrical conditions both exchanges remain always exactly opposite to each other, resulting in a zero transfer of angular momentum from light to matter. These are the conditions for a direct transformation from spin to orbital angular momentum where matter is the intermediary[34]. Marrucci *et al.* also demonstrated this process experimentally with visible light by using patterned liquid 'q-plates' (QP) [35]. In essence, a QP is a slab of a birefringent material, a liquid crystal for example, with a uniform birefringent phase retardation δ and a transverse optical axis pattern with a nonzero topological charge. The pattern distribution is defined by the number q of rotations that the optical axis exhibits in a path circling once around the center of the plate, where a topological defect must be present of topological charge q (being q an integer or semi-integer). When a circularly polarized Gaussian beam traverses a QP, a helical beam of topological charge $\ell = \pm 2q$ is generated at the output, whose sign is determined by the input polarization state, allowing for high-speed switching. QPs provide with a very efficient, fast and stable way to generate beams endowed with OAM, but with the inconvenience that each QP is capable to generate only two different values of the winding number, this is, $\ell = \pm 2q$.

References

[1] M. Lax, W. H. Louisell, and W. B. McKnight, “From Maxwell equations to paraxial wave optics,” Phys. Rev. A **11**, 1365–1369 (1975).

[2] L. W. Davis, “Theory of electromagnetic beams,” Phys. Rev. A **19**, 1177–1179 (1979).

[3] A. E. Siegman, *Lasers* (Standfor University, 1986).

[4] J. Durnin, J. J. Micelli, and J. H. Eberly, “Diffraction-free beams.” Phys. Rev. Lett. **58**, 1499–501 (1987).

[5] A. Sadowsky, “ Acta et Commentationes Imp.” Universitatis Jurievensis **7**, 1–3 (1899).

[6] J. H. Poynting, “The wave motion of a revolving shaft, and a sugesstion as to the angular momentum in a beam of circularly polarised light,” Proc. Roy. Soc. London **Ser. A 82**, 560–567 (1909).

[7] R. A. Beth, “Mechanical detection and measurement of the angular momentum of light,” Phys. Rev. **50**, 115–125 (1936).

[8] L. Allen, M. W. Beijersbergen, R. J. C. Spreeuw, and J. P. Woerdman, “Orbital angular momentum of light and the transformation of Laguerre-Gaussian laser modes,” Phys. Rev. A **45**, 8185–8189 (1992).

[9] M. W. Beijersbergen, L. Allen, H. E. L. O. van der Veen, and J. P. Woerdman, “Astigmatic laser mode converters and transfer of orbital angular momentum,” Opics Communications **96**, 123–132 (1993).

[10] D. J. Griffiths, *Introduction to elecctrodynamics* (Prentice Hall, 1999), 3rd ed.

[11] J. Courtial, K. Dholakia, L. Allen, and M. J. Padgett, “Gaussian beams with very high orbital angular momentum,” Opt. Commun. **144**, 210–213 (1997).

[12] C. I. Osorio, G. Molina-Terriza, and J. P. Torres, “Orbital angular momentum correlations of entangled paired photons,” J. Opt. A: Pure Appl. Opt. **11**, 094013 (2009).

[13] A. O’Neil, I. MacVicar, L. Allen, and M. Padgett, “Intrinsic and extrinsic nature of the orbital angular momentum of a light beam.” Phys. Rev. Lett. **88**, 053601 (2002).

[14] N. B. Simpson, K. Dholakia, L. Allen, and M. J. Padgett, “Mechanical equivalence of spin and orbital angular momentum of light: An optical spanner,” Opt. Lett. **22**, 52–54 (1997).

[15] M. Mirhosseini, O. S. Magana-Loaiza, C. Chen, B. Rodenburg, M. Malik, and R. Boyd, “Rapid generation of light beams carrying orbital angular momentum ,” Opt. Express **21** (2013).

[16] C. Tam and C. O. Weiss, “Bistability and optical switching of spatial patterns in a laser,” J. Opt. Soc. Am. B **7**, 1034–1038 (1990).

[17] A. Amiel, N. Davidson, G. Machavariani, E. Hasman, and A. A. Friesem, “Efficient Selection of High-Order Laguerre–Gaussian Modes in a Q-Switched Nd : YAG Laser,” J. of quantum electronics **39**, 74–82 (2003).

[18] M. Okida, T. Omatsu, M. Itoh, and T. Yatagai, “Direct generation of high power Laguerre– Gaussian output from a diode-pumped Nd:YVO4 1.3 μ m bounce laser,” Opt. Express **15**, 7616–7622 (2007).

[19] L. Allen and M. Padgett, “Equivalent geometric transformations for spin and orbital angular momentum of light,” J. of Modern Optics **54**, 487–491 (2007).

[20] M. Padgget, J. Arlt, N. Simpson, and L. Allen, “An experiment to observe the intensity and phase structure of Laguerre-Gaussian laser modes,” American Journal of phisics **64**, 77–82 (1996).

[21] M. J. Padgett and J. Courtial, “Poincaré-sphere equivalent for light beams containing orbital angular momentum,” Opt. Lett. **24**, 430–432 (1999).

[22] J. Courtial and M. J. Padgett, “Performance of a cylindrical lens mode converter for producing Laguerre-Gaussian laser modes,” Opt. Commun. **159**, 13–18 (1999).

[23] S. S. R. Oemrawsingh, E. R. Eliel, J. P. Woerdman, E. J. K. E. Verstegen, J. G. Kloosterboer, and G. W. Hooft, “Half-integer spiral phase plates for optical wavelengths,” J. Opt. A: Pure Appl. Opt. **6**, S288–S290 (2004).

[24] S. S. R. Oemrawsingh, J. A. W. van Houwelingen, E. R. Eliel, J. P. Woerdman, E. J. K. Verstegen, J. G. Kloosterboer, and G. W. ’t Hooft, “Production and characterization of spiral phase plates for optical wavelengths,” Applied Optics **43**, 688–694 (2004).

[25] M. V. Berry, “Optical vortices evolving from helicoidal integer and fractional phase steps,” J. Opt. A: Pure Appl. Opt. **6**, 259–268 (2004).

[26] J. Leach, E. Yao, and M. J. Padgett, “Observation of the vortex structure of a non-integer vortex beam,” New J. Phys. **6**, 71 (2004).

[27] H. Tsai, H. Smith, and R. Menon, “Fabrication of spiral-phase diffractive elements using scanning-electron-beam lithography,” Vac. Sci. Technol. B **25**, 2068–2071 (2007).

[28] C. Rostchild, S. Zommer, S. Moed, O. Hershcovitz, and S. G. Lipson, “Adjustable spiral phase plate,” Applied Optics **43**, 2397–2399 (2004).

[29] V. Y. Bazenhov, M. V. Vasnetsov, and M. S. Soskin, “Laser beams with screw dislocations in their wave fronts,” Sov. Phys. JETP Lett **52**, 429–431 (1990).

[30] V. Y. Bazhenov, M. S. Soskin, and M. V. Vasnetsov, “Screw Dislocations in Light Wavefronts,” J. Mod. Opt. **39**, 985–990 (1992).

[31] N. R. Heckenberg, R. J. McDuff, C. P. Smith, H. Rubinztein-Dunlop, and M. J. Wegener, “Laser beams with phase singularities,” Optical and quantum electronics **24**, S951–S962 (1992).

[32] D. Grier, “A revolution in optical manipulation,” Nature **424**, 810–816 (2003).

[33] A. Wright, B. Patterson, S. Poland, J. Girkin, G. Gibson, and M. Padgett, “Dynamic closed-loop system for focus tracking using a spatial light modulator and a deformable membrane mirror,” Opt. Express **14**, 222–228 (2006).

[34] L. Marrucci, C. Manzo, and D. Paparo, “Optical Spin-to-Orbital Angular Momentum Conversion in Inhomogeneous Anisotropic Media,” Phys. Rev. Lett **96** (2006).

[35] S. Slussarenko, A. Murauski, T. Du, V. Chigrinov, L. Marrucci, and E. Santamato, “Tunable liquid crystal q-plates with arbitrary topological charge,” Opt. Express **5**, 4085–4090 (2011).

3

A new type of self-healing beams

Contents

3.1 Self-healing beams **33**
3.1.1 Airy beams 34
3.1.2 Petal-like beams 34
3.1.3 Pearcy beams 35
3.2 Helico-conical Beams **36**
3.2.1 Experimental observation of self-healing properties in HC beams 36
3.2.2 Energy flow in Helico-conical beams 38
References **40**

In this chapter we describe one of the most exotic features of a particular set of beams, this is, the ability to regenerate its transverse intensity profile after being distorted by an obstacle placed at its propagation path. These beams are known as self-healing beams. The dynamics involved in the phenomenon of self reconstruction is linked to the energy transport and it is still under investigation. This chapter is divided in two sections. In the first section we describe some examples of self-healing beams. In the last section we report our discovery about the self reconstruction properties in helico-conical (HC) beams. HC beams are a particular set of beams recently discovered in which, both the intensity and the phase twist around the optical axis.

3.1 Self-healing beams

Perhaps one of the most remarkable properties of any diffraction-free beam is their ability to recover their transverse intensity profile after being distorted by a small perturbation placed at its path. These beams are know as self-healing beams. Diffraction-free beams are not the only beams with the ability to auto-reconstruct, there exist also nondifracting-free beams that tend to recover their intensity profile when this is distorted [1, 2]. Self-healing beams are of particular interest especially because they can recover after propagating through scattering and turbulent media and they show advantage when used in optical manipulation[3, 4]. This chapter is divided in two sections. In the first one we discuss some of the recently observed cases of self-healing beams. The second section is entirely devoted to present our experimental observation of self-healing properties in Helico-conical beams.

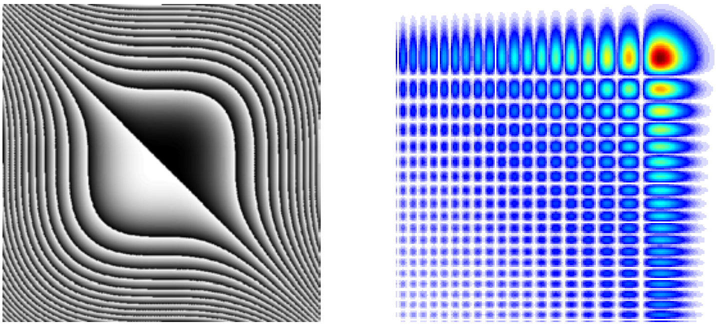

(a) (b)

Figure 3.1: (a) Phase mask encoded in an SLM to produce the AiryBeam. (b) Intensity profile of an Airy beam

3.1.1 Airy beams

Airy beams arose as another solution to the paraxial wave equation [see Eq. (2.24)]. They were first predicted by Siviloglou and Christodoulides in 2007 taking advantage of the similitude between the Schrödinger equation and the paraxial equation [5]. The experimental realization was achieved the same year [6] with the help of an SLM, by using a a cubic phase modulation [see Fig. 3.1(a)] onto an incident Gaussian laser beam, producing the Airy intensity pattern shown in Fig.3.1(b) The main attractiveness of Airy beams is their ability to accelerate as they propagate in free space. This is, the intensity profile of Airy beams experiences a shift in the transverse plane, following a parabolic trajectory in the direction of the main lobe (the one with the highest intensity). This feature was fully exploited by Mazilu *et. al* in the optical micro manipulation field [4], who were able to push small microscopic particles along curved trajectories.

The theoretical and experimental self-healing properties associated to Airy beams were shown by the same group who synthesized these beams for the first time [7]. They showed that Airy beams exhibit remarkable resilience against perturbations tending to reform opun propagation. They also demonstrated that these kind of beams retain their shape when propagating in turbulent media. In their experiment, they blocked with a rectangular obstacle the main intensity lobe, were most of the energy is contained and observed that it started to reconstruct after few centimeters.

In this case, the self-healing process was explained in terms of the transverse power flow. This is, part of the energy surrounding the main lobe of the beam (now blocked by the obstacle) moves towards blocked part of the beam to reconstruct it. This process stops after the self-healing process has finished and the energy within the beam flows again in the same initial direction, at 45^o.

In 2012 an analytical study by X. Chu *et. al* confirmed this first observation [8]. Moreover, they observed that the speed of self-healing process is affected by the size of the obstacle, since a large opaque obstacle causes slow reformation of the Airy beam.

3.1.2 Petal-like beams

The petal-like beams, also known as ferris wheels, are generated by a coaxial superposition of two LG modes of opposite helicity and direction of the Pointing vector (see Fig. 3.2). In general, the superposition can be written as

$$u(r) = A(r)[\exp(i\ell\phi) + \exp(-i\ell\phi)]. \tag{3.1}$$

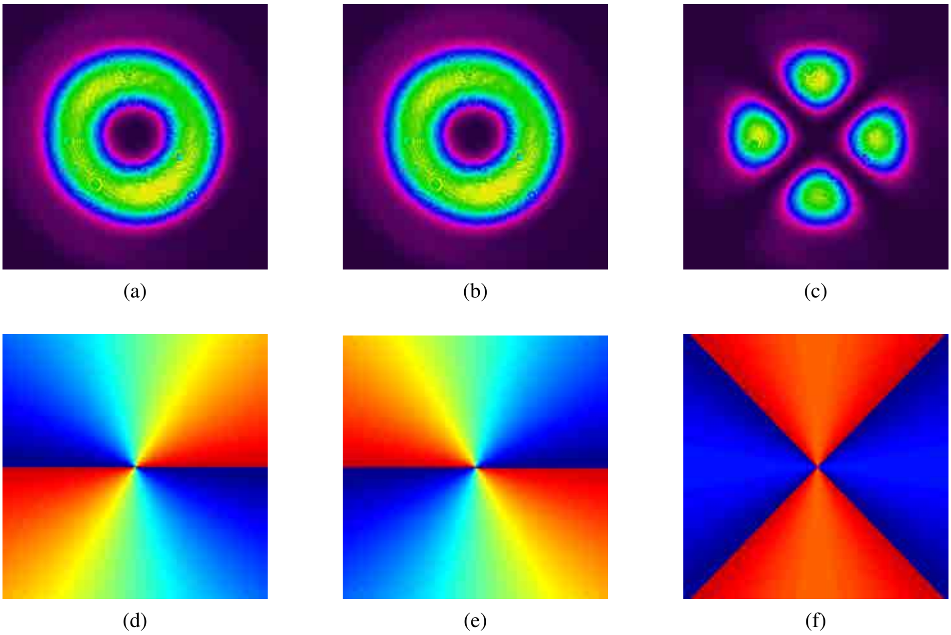

Figure 3.2: Experimental intensity pattern and phase of Laguerre-Gaussian beams with winding numbers $\ell = 2$ [(a) and (d)] and $\ell = -2$ [(b) and (e)] and petal-like beam [(c) and (f)].

Very recently it was shown that, although these structures are not diffraction-free, they show self-healing properties [9, 10]. In [9] one of the petals was blocked in a similar way as in the case of Airy beams. The reconstruction of the beam was monitored again in terms of the Poynting vector of the field upon propagation. They were able to observe a redistribution of energy from the surrounding petals, contributing to form a nascent petal, growing in strength as the beam propagates. At a distance $z = 220cm$, from the plane where the blocked was located, they observed an almost full reconstructed beam.

They also observed that such a reconstruction is not always guaranteed and it is influenced by the distance between the obstacle and the location waist of the beam. This study was complemented by Litvin *et al.* who gave an intuitive argument for the self-reconstruction of petal-like beams, and derived a simple analytical equation of the distance required for the self-reconstruction [10]. They also pointed out that this distance is independent of the azimuthal orders in the superposition but depends on the angular size of the obstacle.

3.1.3 Pearcy beams

A novel type of paraxial light beam was recently introduced by J. D. Ring *et. al*, which is based on the Pearcey function [11]. Within the context of catastrophe theory, the Pearcey function is used to describe diffraction about a cusp caustic. The transverse profile of a Pearcey beam resembles this diffraction cusp. Upon propagation this novel beam focuses to a small spot, after which it undergoes a spatial inversion.

In a similar way to Bessel and Airy beams, Pearcey beams have infinite energy, hence the Pearcey function needs to be modulated by a Gaussian function in real space. This modulation leaves almost intact the properties of the beam. Pearcey beams were also reported to self-heal in the same paper, though not discussed in detail. The main lobe of the beam was obstructed and a clear revival of the

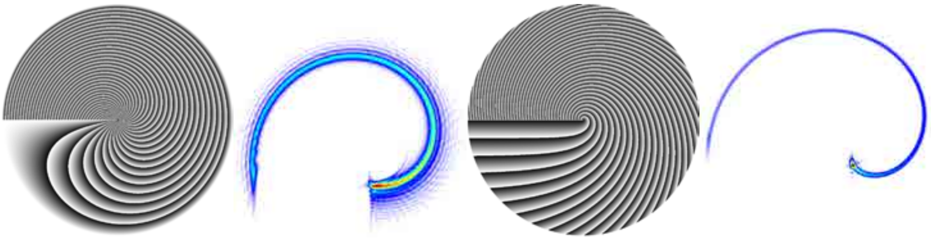
(a) (b) (c) (d)

Figure 3.3: (a) and (c) On-axis Holograms to generate $K = 0$ and $K = 1$ HC beams respectively. (b) and (d) Far field intensity pattern of $K = 0$ and $K = 1$ HC beams.

intensity pattern was observed after few centimeters. It was also noticed that for larger obstructions the reconstruction took place at longer distances. The propagation dynamics of the obstructed beam is very similar to an unobstructed beam, this is, it still focuses to a small point after which it inverts its intensity profile where a full reconstruction is observed.

3.2 Helico-conical Beams

In this last section, we report about the first experimental observation of the self-healing behavior of Helico-conical (HC) beams [12]. HC beams are created by multiplying a helical and a conical phase. As consequence the complex exponential cannot be separated into radial and azimuthal terms. More explicitly, the phase of a HC beams has the form

$$\Phi(\rho, \phi) = \ell\phi\left(K - \frac{\rho}{\rho_0}\right), \tag{3.2}$$

where ℓ is the winding number, ρ is the radial coordinate normalized by ρ_0, ϕ is the azimuthal angle and K is a constant that can take the values 0 or 1. HC beams feature a spiral profile in both the amplitude and the phase. In the far field, the intensity profile of these beams resembles a spiral, with $K = 1$ [Fig. 3.3(b)] having a more pronounced head near the center of the beam axis compared to $K = 0$ [Fig. 3.3(d)].

HC beams are of great interest because, unlike LG beams, its far field projection maintains a high photon concentration even at high values of topological charge. The applications of HC beams range from fundamental studies of light and atoms such as in quantum entanglement of the OAM to toroidal traps for cold atoms as well as for optical manipulation of microscopic particles. In the context of optical manipulations, very recently a HC beam with $K = 0$ was used to trap and induce spiral motion to particles along its path [13], a three dimensional motion that combines phase gradient with intensity gradient forces.

3.2.1 Experimental observation of self-healing properties in HC beams

Here, we provide evidence that HC beams reconstruct their intensity profile at a relatively short propagation distance after a small perturbation is placed in its path. We observe how the beam reconstructs for different values of ℓ and for different block sizes. The phase of the HCOB is not rotationally symmetric, therefore the reconstruction of the intensity depends on the angular position of the obstructing block, a property we also analyzed. We then compare our experimental results

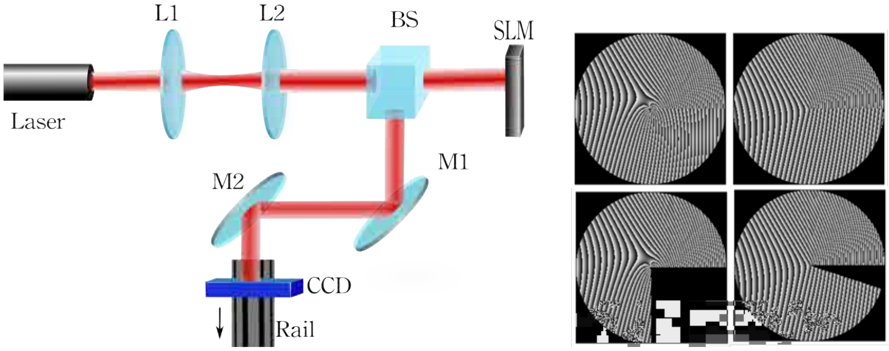

(a) (b)

Figure 3.4: (a) Experimental setup. (b) Samples of unblocked (above) and blocked (below) holograms encoded onto a SLM. Lenses L1 and L2 expands and collimates the incoming beam while M1 and M2 mirrors for alignment; BS is beam splitter and CCD stands for Charge Coupled Device camera.

with numerical simulations. Finally, we look at the transverse energy flow of the beam and relate it to its self-healing property [12]. A sketch of the experimental setup implemented to monitor the beam as it propagates in free space is shown in Fig. 3.4. A collimated HeNe ($\lambda = 632.8$ nm) laser impinges onto a spatial light modulator (SLM) encoded with the appropriated computer-generated hologram. The intensity pattern of the HC beam was captured with a Charged-Coupled Device (CCD) camera connected to a computer. In order to observe the self healing process, we mounted the CCD on a computer-controlled rail aligned with the beam propagation axis. Figure 3.5 show the experimental (top row) and theoretical (bottom row) intensity profiles obtained at a distance of 16 cm from the SLM for $K = 0$ (left column) and $K = 1$ (right column) respectively.

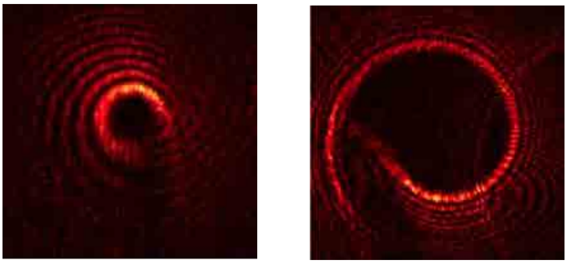

(a) (b)

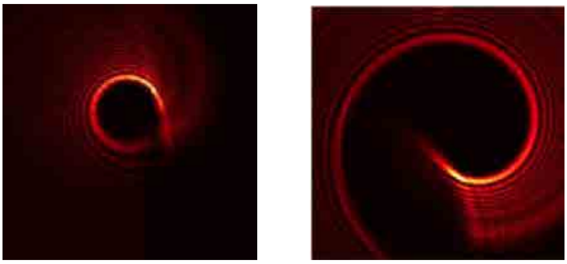

(c) (d)

Figure 3.5: Experimental [(a) and (b)] and theoreticl [(c) and (d)] intensity profiles of Helico-conical beams, after 16cm propagation distance. In (a) $k = 0$ and in (b) $K = 1$.

The block was imitated by means of an incomplete hologram. This was done for better control of the size of the block. Figure 3.6 shows experimental and simulated images of the self healing process. Figure3.6(a) (left column) show the intensity pattern of a $K = 0$, $\ell = 50$ HC beam at positions $z = 0$ cm (right after the block) and $z = 8$ cm. There we can observe how part of the blocked intensity has been reconstructed. For comparison we simulated numerically the intensity distribution upon propagation using Fresnel propagation [Fig. 3.6(a) right column]. An analogous experiment and simulation was done with a $K = 1$, $\ell = 50$ HC beam [3.6(b)]

By moving the camera away from the SLM, we observed that the HCOBs self-heal as the beams propagate. The shadow of the block moves in a rotatory manner reminiscent of the self-healing of higher-order Bessel beams. However, unlike Bessel beams, HCOBS slightly rotate and expand.

3.2.2 Energy flow in Helico-conical beams

Finally, in order to understand why HC beams self-heal, a numerical computation of the energy flux in the transverse plane was carried out using the expression derived in section 2.3.2 [Eq. (2.56)]. The energy flow is,

$$\langle \mathbf{s} \rangle = \frac{\omega k}{2\mu_0} \left\{ 2|u|^2 \, \hat{\mathbf{z}} + \frac{i}{k} \left[u \nabla u^* - u^* \nabla u \right] \right\}$$

Figure 3.7 shows the transverse energy flow calculated with this equation for the case $\ell = 30$, $K = 0$ HC beam. The direction of the energy flow traces a curved path (shown as white arrows in figure 3.7). Similar images can be obtained for $K = 1$. Even with the block, the direction of the energy flow is unaltered, always flowing in a circulatory way. The energy flow is once again responsible for the reconstruction of the blocked area, in a very similar way to the cases discussed before. Since both the energy and the energy flow are greater at the upper section, the beam reconstructs faster in this part. In addition, the transverse energy flow is greater for larger ℓ values, which translates to

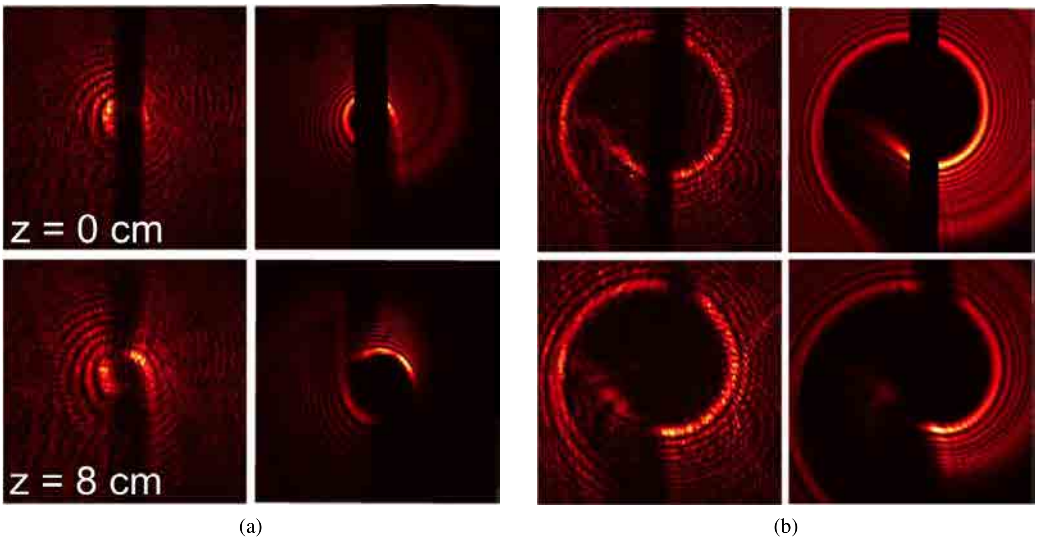

(a) (b)

Figure 3.6: A 0.38*mm* strip is placed at the path of a $\ell = 40$ HC beam. Top images are obtained right after the block while the bottom images are after 8 cm of propagation. (a) corresponds to $K = 0$ and (b) to $K = 1$, in both cases, first column are experimental images while second columns are simulations.

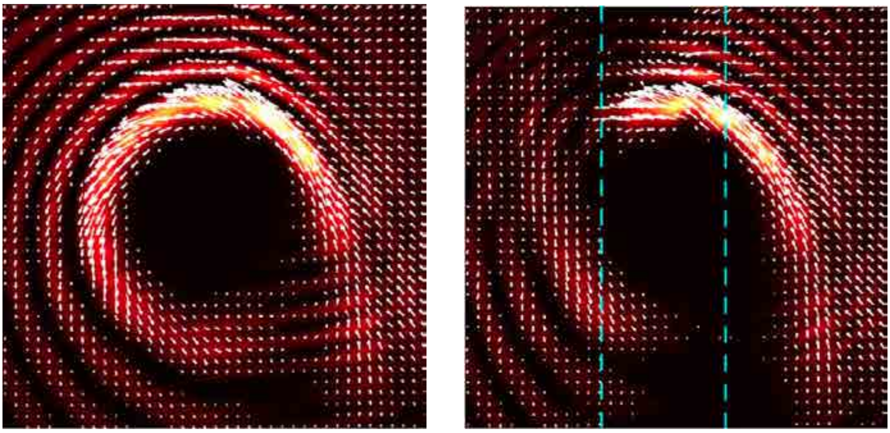
(a) (b)

Figure 3.7: Numerical simulation of the energy flow with an obstruction (a) and without the obstruction (b). The energy flow is unaltered with the presence of the block, it always flows in a circulatory way, being this, responsible for the reconstruction of the intensity in HC beams.

faster reconstruction (not shown). This suggests that the transverse energy flow is the mechanism involved in the beam's reconstruction.

Our experiments show that HC beams have the ability to reconstruct themselves at relatively short propagation distance beyond the small perturbation placed in its path. We were able to observe this for different ℓ values as well as different block sizes and reinforced our experimental results with numerical simulations. These simulations show the transverse energy flow plays a crucial role in the self-healing process.

References

[1] M. Anguiano-Morales, A. Martínez, M. Iturbe-Castillo, S. Chávez-Cerda, and N. Alcalá-Ochoa, “Self-healing property of a caustic optical beam.” Appl. Opt. **46**, 8284–8290 (2007).

[2] P. Vaity and R. P. Singh, “Self-healing property of optical ring lattice,” Opt. Lett. **36**, 2994–2996 (2011).

[3] D. M. H. M. W. S. V. Garcés-Chávez and K. Dholakia, “Simultaneous micromanipulation in multiple planes using a self-reconstructing light beam,” Nature **419**, 145–147 (2002).

[4] M. M. J. Baumgartl and K. Dholakia, “Optically mediated particle clearing using Airy wavepackets,” Nature Photonics **2**, 675–678 (2008).

[5] G. A. Siviloglou and D. N. Christodoulides, “Accelerating finite energy Airy Beams,” Opt. Lett **32**, 979–981 (2007).

[6] J. B. D. G. A. Siviloglou and D. N. Christodoulides, “Observation of Accelerating Airy Beams,” Phys. Rev.Lett **99**, 213901 (2007).

[7] A. Dogariu, J. Broky, G. Siviloglou, and D. Christodoulides, “Self-healing properties of optical Airy beams,” Opt. Express **16**, 12880–12891 (2008).

[8] G. Z. X Chu and R. Chen, “Analytical study of the self-healing property of Airy beams,” Phys. Rev. A **85**, 013815 (2012).

[9] P. Vaity and R. P. Singh, “Self-healing property of optical ring lattice,” Opt. Lett. **36**, 2994–2996 (2011).

[10] I. A. Litvin, L. Burger, and A. Forbes, “Angular self-reconstruction of petal-like beams,” Opt. Lett. **38**, 3363–3365 (2012).

[11] J. D. Ring, J. Lindberg, A. Mourka, M. Mazilu, K. Dholakia, and M. R. Dennis, “Auto-focusing and self-healing of Pearcey beams,” Opt. Express **20**, 18955–18964 (2012).

[12] N. Hermosa, C. Rosales-Guzmán, and J. P. Torres, “Helico-conical optical beams self-heal,” Opt. Lett. **3**, 383–385 (2013).

[13] V. R. Daria, D. Z. Palima, and J. Glückstad, “Optical twists in phase and amplitude,” Opt. Express **19**, 476–481 (2011).

4

Transverse Doppler shift with Structured light

Contents

4.1 Theoretical description of the transverse Doppler shift 42
4.1.1 The longitudinal Doppler shift 42
4.1.2 The transverse Doppler shift 42
4.2 Experimental detection of transverse particle movement with structured light 45
4.2.1 Experimental implementation 46
4.2.2 Experimental results and discussion 48
4.3 Direction sensitive transverse velocity measurement by phase modulated structured light 50
4.4 Measuring the translational and rotational velocities of particles in helical motion. 55
4.4.1 Theoretical framework 56
4.4.2 Experimental implementation 57
References 61

In this chapter we present experimental results on the use of structured light to measure in a direct way the velocity component perpendicular to the direction of illumination. The chapter is organized in four sections. In the first one, we introduce the theoretical basis of this technique (Section 4.1.2). In section 4.2 we present the first experimental results that validates the technique. For this, we used a microparticle moving in the plane perpendicular to the illumination source. In section 4.3 we examine the use of dynamic structured phases to retrieve information of the direction of motion. This, by modulating in time the phase in the transversal plane. In the last section (section4.4) we consider the extension of this technique to tree dimensional motion. In particular, we measured experimentally the velocities involved in helical motion, this is, translation and rotation about the translation axis.

4.1 Theoretical description of the transverse Doppler shift

4.1.1 The longitudinal Doppler shift

The Doppler shift (first noticed by Christian Doppler in 1842) is the perceived change in frequency of waves caused by the relative motion between a transmitting source and a detector . Laser remote sensing systems based on the classical longitudinal Doppler effect, are widely used to monitor the location and velocity of moving targets in fields as diverse as medicine, astronomy, meteorology and aeronautics [1]. Such systems usually employ Gaussian beams, whose phase in the transversal plane is almost constant. The beam reflected by the target will have a time-varying phase given by $\Psi(\mathbf{r}, t) = 2kz(t)$, where $k = 2\pi f/c$ is the wavenumber, f is the frequency of the incident light beam, c is the velocity of light in vacuum and $z(t)$ is the time-dependent relative displacement along z between the emitter and the target. If the target is moving with constant velocity $\mathbf{v}$, the reflected signal will show an optical frequency shift $\Delta f = 2|\mathbf{v}|cos\theta/\lambda$, where θ is the angle between the velocity of the target and the direction of propagation of the light beam. Hence, by knowing the shift in frequency, we can remotely compute the velocity of a target. Since any transverse velocity generates no frequency shift, the classical longitudinal Doppler effect is sensitive only to the velocity of the target along the line-of-sight between the emitter and the detector, *i.e.*, longitudinal velocity and does not provide information about the components of the velocity perpendicular to the direction of propagation of the light beam ($\theta = 90°$). This makes the transverse velocity undetectable in the classical scheme.

To detect the full vector velocity including transverse components, one can perform Doppler measurement along the line of sight for a large set of directions [2]. Moving Doppler instruments can map the velocity field over large areas by alternating the pointing direction or by scanning the beam during the measurement. Various velocity retrieval techniques have been developed to estimate 2D and 3D vector fields from Doppler longitudinal data. Algorithms range from computationally intensive variational data assimilation techniques to simpler and faster methods based on volume velocity processing. In general, however, all these algorithms suffer of poor spatial and temporal resolution and tend to loose local information about the velocity field due to the averaging involved. Moreover, these schemes require fast mechanical realignment of the direction of propagation of the laser beam, which render its implementation more complicated.

Relativity theory shows that the Doppler effect is sensitive to transverse velocities as well - *the relativistic transverse Doppler effect* [3]. Unfortunately, it yields relative frequency shifts of the order of $\sim \mathrm{v}^2/c^2$, which renders the sought-after frequency shifts staggeringly small in all applications of interest in current laser radar systems. Moreover, it can not distinguish between different directions of movement in the transverse plane, giving all of them the same frequency shift for a given transverse velocity. In the next section we discuss about how these drawbacks can be overcame by using structured light.

4.1.2 The transverse Doppler shift

In 2011, Belmonte and Torres put forward a novel method to measure directly transverse velocity components using structured light as illumination source [4]. In this scheme, the illumination beam can take on different spatial phase profiles that are tailored to adapt to the target's motion. The beam must have a wide enough transverse intensity profile to cover all possible locations of the moving particle. In this way, the measurement of the transverse velocity is enormously simplified. The main idea is based on the fact that structured light has different phase values at each point in the transverse plane . Hence the phase of the reflected light from a moving target will contain information about the position and velocity of the target at each instant, producing a Doppler shift associated to the change of transverse position.

Assuming that a single small particle is illuminated by a paraxial light beam of the form

$$\mathbb{E}(\mathbf{r}, t) = E_0 \exp\{i[kz + \Psi(\mathbf{r}_\perp) - 2\pi f t]\}, \tag{4.1}$$

being E_0 the complex amplitude of the beam at the location of the scatterer, $\mathbf{r}_\perp$ the transverse position across the beam wavefront, and $\Psi(\mathbf{r})$ a spatially varying phase that has been imprinted into the beam, A. Belmonte and J. P. Torres demonstrated that when the particle passes the observation region with velocity $\mathbf{v}$, it generates a burst of optical echoes that, when coherently detected, produce a time varying phase given by

$$\Theta = 2kzt + \Psi[\mathbf{r}_\perp(t)], \tag{4.2}$$

with a time rate of the total phase change

$$\frac{\partial \Theta}{\partial t} = 2k\mathrm{v}_z + \nabla_\perp \Psi \cdot \mathrm{v}_\perp. \tag{4.3}$$

The first term of Eq. (4.3) can be immediately associated to the usual longitudinal Doppler shift. The second yields a new Doppler frequency shift, due to the transverse velocity v_z of the scatterer, namely

$$\Delta f_\perp = \frac{1}{2\pi} \nabla_\perp \Psi[\mathbf{r}(t)] \cdot \mathbf{v}_\perp, \tag{4.4}$$

where $\mathbf{r}(t)$ is the transverse position of the target across the beam wavefront and $\nabla_\perp \Psi[\mathbf{r}(t)]$ is the transversal gradient of the phase. This new transverse Doppler component is independent of the optical frequency [5]. For the sake of clarity, two examples will be explained with more detail in the next section: a particle moving with a constant transverse velocity $\mathrm{v}_\perp$ and a particle rotating in the transverse plane with an a angular velocity Ω.

Transverse linear motion

Let us consider a particle moving with a constant velocity $\mathrm{v}_\perp$ along the $\hat{\mathbf{x}}$ direction, this is, the component of the velocity along the direction $\hat{\mathbf{z}}$ is zero. As mentioned before, there are methods that allow to measure the velocity $\mathrm{v}_\perp$ in a non straight forward way by illuminating the target along several directions (for example by continuously changing the illumination source). However if we illuminate the target with a structured beam, this task might be greatly simplified as long as we choose an appropriate engineered phase to imprint the beam with. For the case under consideration, the most convenient beam to illuminate with is one with a structured phase that increases or decreases linearly in the same direction of motion, this is, a phase of the form $\Psi = \gamma x$, being γ a constant [Fig. 4.1(a)]. In this way, as the particle moves trough the beam, it will reflect light with a continuously varying phase depending on the position of the particle. When coherently detected, reflected light will experience a frequency shift given by Eq. (4.4) [Fig. 4.1(b)]. Computation of $\nabla_\perp \Psi = \gamma \hat{\mathbf{x}}$ makes evident that an appropriate choice of the structured phase simplifies enormously the math involved. Hence, the frequency shift is

$$\Delta f = \frac{\gamma \mathrm{v}_\perp}{2\pi}. \tag{4.5}$$

Transverse rotational motion

As a second example, let us consider an object rotating with a constant angular velocity Ω (see Fig. 4.2). In this case, the movement's geometry suggests a phase that increases or decreases linearly in the azimuthal direction, this is, $\exp(i\ell\phi)$. Computation of $\nabla_\perp \Psi$ can be done by changing to cylindrical coordinates, where ∇_T is defined as

$$\nabla_\perp \Psi = \frac{\partial(\ell\phi)}{\partial \rho}\,\hat{\rho} + \frac{1}{\rho}\frac{\partial(\ell\phi)}{\partial \phi}\,\hat{\phi} = \frac{\ell}{\rho}\,\hat{\phi}. \tag{4.6}$$

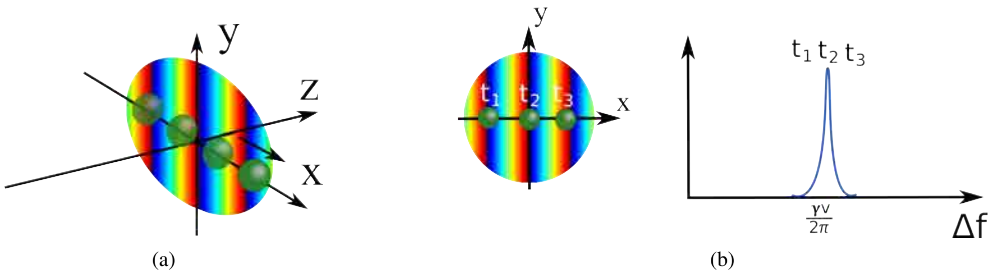

(a) (b)

Figure 4.1: (a) A particle moving in a light beam with structured linear phase gradient. (b) Variation in time $(t_1, t_2, t_3, ...)$ of the particle across the structured light beam induces a frequency shift $\Delta f = \gamma v_\perp/2\pi$, scalable with γ

In this coordinate system, the velocity, directed along the azimuthal direction, is given by $\mathbf{v} = \mathbf{\Omega}\rho\,\hat{\phi}$. Hence, the light reflected back by the rotating particle will be shifted in frequency by an amount

$$\Delta f_\perp = \frac{|\ell\omega|}{2\pi}. \tag{4.7}$$

Again, Eq. (4.7) does not depend on the wavelength of the illuminating beam. Notice also that the frequency shift can be scaled on demand by simply changing the winding number ℓ.

Alternative description in terms of the Poynting vector

Recently, Lavery *et al.* [10] demonstrated the angular frequency detection of a spinning object using light with orbital angular momentum. Here we show, using the Poynting vector, that this scheme is equivalent to what we have presented. In general, the Doppler frequency shift generated by a moving surface can be written as

$$\Delta f = \frac{1}{\lambda}(\hat{\mathbf{d}}_1 - \hat{\mathbf{d}}_2)\cdot(\mathbf{v}), \tag{4.8}$$

where λ is the wavelength of the incident light with unit vector $\hat{\mathbf{d}}_1$, $\hat{\mathbf{d}}_2$ is the unit vector of the scattered light and $\mathbf{v}$ is the velocity of the moving surface. For a paraxial incident beam whose vector potential $\mathbf{A}$ is of the form $\mathbf{A} = \hat{\mathbf{x}}\mathbf{u}(x, y, z)\exp(ikz)$, the Poynting vector $\mathbf{S}$ is given by

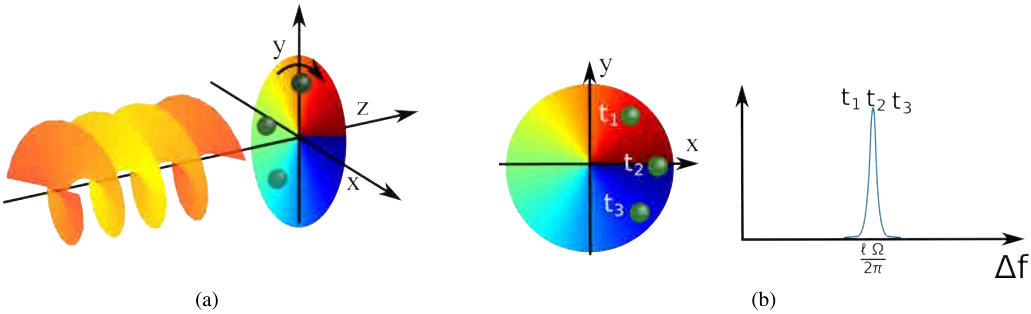

(a) (b)

Figure 4.2: (a) A rotating particle being illuminated with an LG beam endowed with OAM. (b) Variation in time $(t_1, t_2, t_3, ...)$of the particle yields a frequency shift $\Delta f_\perp = |\ell\Omega|/2\pi$ to the reflected light that can be scaled with ℓ. $\Delta f_\perp$ regardless of the wavelength of the illuminating source.

$$\mathbf{S} = \frac{|E|^2}{2\eta}\left(\hat{\mathbf{z}} + \frac{1}{k}\nabla_\perp\Psi\right), \tag{4.9}$$

where η is the vacuum impedance. Since for a paraxial beam, the longitudinal component of S is much larger than the transverse component, one can write

$$\hat{\mathbf{d}} = \hat{\mathbf{z}} + \frac{1}{k}\nabla_\perp\Psi. \tag{4.10}$$

From Eqs. (4.8) and (4.10), the Doppler shift observed for $\hat{\mathbf{d}}_2 = -\hat{\mathbf{z}}$ is

$$\Delta f = \frac{1}{\lambda}\frac{\nabla_\perp\Psi}{k}\cdot\mathbf{v}. \tag{4.11}$$

If we substitute $k = 2\pi/\lambda$ in Eq. (4.11) we arrive to Eq. (4) of Belmonte and Torres [4]. Furthermore, we can define $\delta = \nabla_\perp\Psi/k$. Using $\lambda f = c$, Eq. (4.11) reduces to Eq. (2) in Lavery *et al.* [10] for the one-dimensional case.

4.2 Experimental detection of transverse particle movement with structured light

In this section we will discus about the experimental demonstration of the technique presented in the previous section. Once demonstrated, this technique might be added to current laser radar systems to expand their functionalities. For example, one can envision a system capable to measure at once both, longitudinal ($v_{||}$) and transverse components ($v_\perp$) of the velocity. On one hand, the longitudinal component of the velocity generates a frequency shifts $\sim v_{||}/\lambda$ and on the other, the transverse component produces frequency shifts in a frequency band determined by the phase gradient of the light. For instance, for a particle moving in a circular path with radius R_0 and constant angular velocity, the frequency shift due to the transverse velocity $v_\perp$ is $\Delta f = \ell v_\perp/(2\pi R_0)$. Notice that the frequency band can be tuned by changing the phase profile, which cannot be done with the techniques based on the classical longitudinal Doppler effect.

As discussed above, the key point, in measuring the transverse component of the velocity, relies on the use of structured light beams. These beams are unique in the sense that their phases can be engineered such that each point in its transverse plane has an associated phase value. When a particle moves across the beam, it reflects the position-dependent varying phase imprinted on the laser beam, producing a signal with a time-dependent phase at the receiver -a Doppler frequency shift- associated with the change of transverse position. In chapter 2 Section 2.4.2 we discussed about different possibilities that current technology offers to efficiently generate almost any light beam with the spatial shape required: appropriately designed spiral phase plates, computer-generated holograms, q-plates, as well as suitable combination of astigmatic optical elements [6]. However, during the last decade, Spatial Light Modulators (SLMs) have become one of the most popular devices capable to generate almost any exotic beam. With these devices, one can generate and modify complex spatial phase and amplitude light patterns in a fast and efficient manner.

The SLM technology opens the possibility to use the Doppler transverse effect discussed here to detect not only transverse velocities, but transverse positions as well. In this case, a unique phase gradient is associated with each location in the transverse plane, so that the detection of the corresponding frequency shift can only come from the presence of the particle at a specific location with that specific phase gradient.

4.2.1 Experimental implementation

The experimental setup

A modified Mach-Zehnder interferometer, shown in Fig. 4.3, is used to demonstrate the feasibility and usefulness of the method proposed. The continuous wave (CW) Helium-Neon laser light source (wavelength $\lambda = 633$ nm, power $P \sim 15$ mW) is spatially filtered and expanded by a telescope T1 made with a lens combination of focal lengths $F_1 = 25$ mm and $F_2 = 100$ mm for the front and back lenses respectively [Fig. 4.4(b)]. The beam is then divided by a beam splitter into two: a reference beam [green line in Fig. 4.3(b)] and a signal beam [blue line in Fig. 4.3(b)]. The signal beam impinges onto a spatial light modulator (SLM, Hamamatsu LCOS-SLM) where it acquires the desired phase profile via a 2π-modulo phase wrapped computer generated hologram (CGH) displayed on the SLM. The CGH is calculated from the interference of a beam with our desired phase and a tilted plane wave to generate a hologram with a carrier period of 84.85 μm.

Figure 4.4(a) shows as example the hologram encoded in the SLM to produce an LG_0^5 mode. In our experiments, we produce beams with helical or linear phases. The helical phase is made with

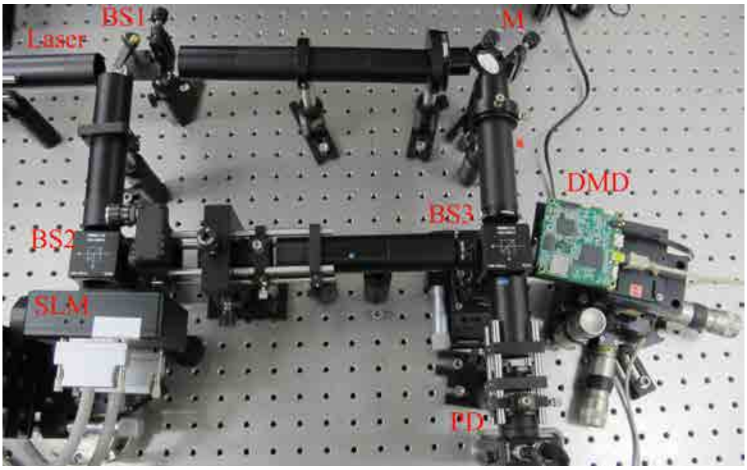

(a) Picture of the experimental setup

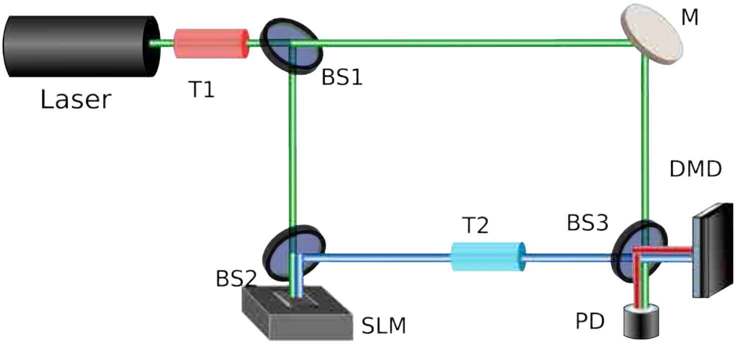

(b) Simplified sketch of the experimental setup

Figure 4.3: A collimated Gaussian beam is divided by a beam splitter (BS) into a reference beam (green line) and a probe beam. The probe beam acquires the desired phase profile after impinging on the SLM. This structured light (blue line) is then made to shine onto a Digital Mirror Display (DMD). The DMD is controlled to mimic a moving particle. Light reflected by the particle (red line) is made to interfere with the reference beam at the photodetector (PD).

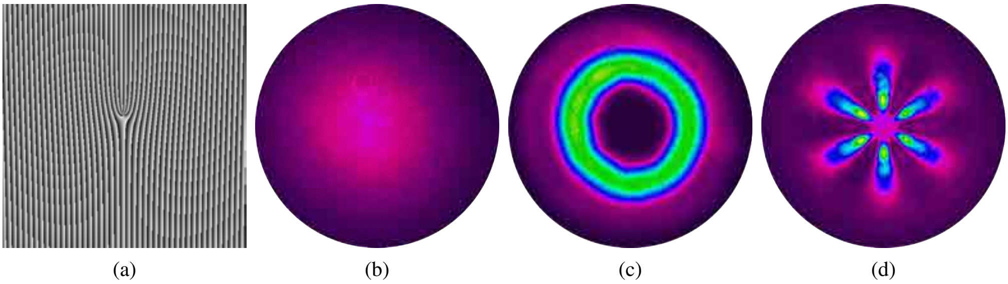
(a) (b) (c) (d)

Figure 4.4: (a) Example of the holograms encoded in the SLM. (b) Reference beam. (c) Structured light beam (in this case, LG_0^6). (d) Interference of the Structured light beam with the reference beam.

a phase that changes as $2\pi\ell$ as one goes around the azimuth, where ℓ is an integer, the winding number of the beam. The linear phase is done by putting a small constant tilt in the beam. The carrier period makes the separation and filtering of the desired structured beam easier. This is done by appropriately placing another telescope T2 with lens combination of focal lengths $F_3 = 50$ mm for the front lens, $F_4 = 30$ mm for the back lens and a 30 μm pinhole. Notice that the beam size is reduced to fit the active area of the Digital micromirror device (DMD). Figure 4.4(c) shows an example of a structured beam we used to illuminate the particles, in this case a Laguerre-Gaussian of winding number $\ell = 6$. The structured signal beam [blue line in Fig. 4.3(b)] is then sent to the controllable DMD where a tiny circle composed of an array of micromirrors simulates a 35 μm radius particle. By manipulating the position and the time in which the mirrors are in the 'on' state, the micromirrors ensemble can mimic a particle that is moving with different paths and velocities (see details at the Simulation of particle and its movement). Light reflected [red line in Fig. 4.3(b)] from the DMD contains information about the velocity and position of the particle. The signal beam is then made to interfere with the reference beam at the photodetector. Figure 4.4(d) shows an example of interference produced when the DMD reflects all the incoming intensity, six maximum intensity lobes are present because the winding number for this case is $\ell = 6$. The PD is connected to an oscilloscope (TDS2012C, Tektronix) attached to a computer for faster data acquisition and analysis.

Simulation of particle and its movement

The structured light beam illuminates a scatterer that reflects back the signal beam with a phase that depends on the specific location of the scatterer. We mimic a particle and its movement by controlling a DMD from DLP Lightcrafter [Fig. 4.5(a)]. We remove the RGB LED light engine to expose the DMD display. Our DMD is composed of an array of 608 × 684 micro-mirrors with a diagonal side length of 10.8 μm arranged in a diamond geometry. Each micro-mirror can be controlled independently and switched between 'on' and 'off' state. A set of 1-bit depth images are uploaded in the DMD software, where a '0' corresponds to the 'on' state and a '1' to the 'off' state. The time in which the micromirrors are in the 'on' or 'off' state can also be controlled by the software. A micromirror in the 'on' state will have a tilt of $+12^0$ while the 'off' state has -12^0 [see Fig. 4.5](b). Thereby, only micromirrors which are on the 'on' state will reflect back light in the correct direction by careful alignment of the DMD. We make sure that the 'on' state reflects light that is parallel to the optical axis of the incident beam. Light reflected from the 'off' is blocked. A 35 μm radius disk-like particle was simulated with an array of 7 × 14 micromirrors. ensemble of micromirrors are manipulated such that a constant array size are turned 'on' at specific positions in a particular interval of time while all other micromirrors are switched 'off'. With this, the moving array seems emulates a moving particle. We vary the speed of the movement by changing the time

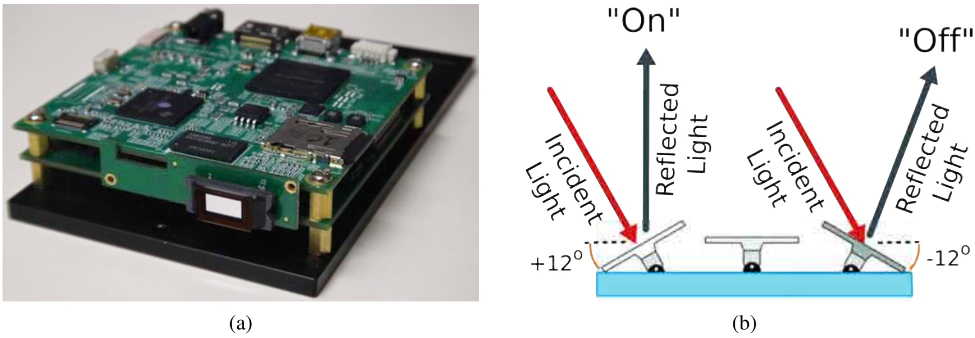

(a) (b)

Figure 4.5: (a) Digital Micromirror Device (DMD).

interval to switch to another set of micromirror array. Hence, by controlling which specific mirrors are in the 'on' or 'off' states, and the timing between these states, we can simulate any transverse particle's trajectory and velocity.

Data Analysis

Understanding how the strength of our signal is distributed in the frequency domain relative to the strengths of other unwanted ambient signals, is central to the design of any sensor system intended to estimate the Doppler shift signal. While many methods for spectrum estimation are discussed in the statistical literature, we use here only the overlapped segmented averaging of modified periodograms. In our case, a periodogram is the discrete Fourier transform (DFT) of one segment of the signal time series that has been modified by the application of a time-domain window function. It has been averaged to reduce the variance of the spectral estimates. While its practical implementation involves a number of nontrivial details -such as equal binning of frequencies, Hamming windowing, and filtering of unwanted residual amplitude modulations- our data processing and analysis is rather straightforward and computes a spectrum or spectral density starting from a digitized time series, typically measured in Volts at the input of the A/D-converter.

The time-varying phase of the reflected signal beam was retrieved by observing the time-varying intensity modulation of the interference between the reference and the signal beams. A typical record is shown in Figs. 4.6(a), where a signal beam of the form $E(\rho, \phi, z) = I^{1/2}(\rho) \exp(ikz + i\ell\phi - i2\pi f t)$ illuminates a particle which follows a uniform circular movement. Here ρ is the radial coordinate in cylindrical coordinates, ϕ is the azimuthal angle and ℓ is the winding number of the beam [7]. Ideally, the structured optical beam is designed so that the movement of the scatterer under investigation takes place in a region where $I_0(\mathbf{r}_\perp)$ is approximately constant, so that only the spatially-varying induced phase differences produce time-varying intensity modulations at the receiver side. After detection, filtering and postprocessing of the signal detected, to remove noise and unwanted signals, one obtains frequency spectra as the one shown in Fig. 4.6(b).

4.2.2 Experimental results and discussion

For the proof of concept, two types of motions were mimicked with the DMD: a transverse rectilinear motion and a transverse rotational motion. Our result are presented next.

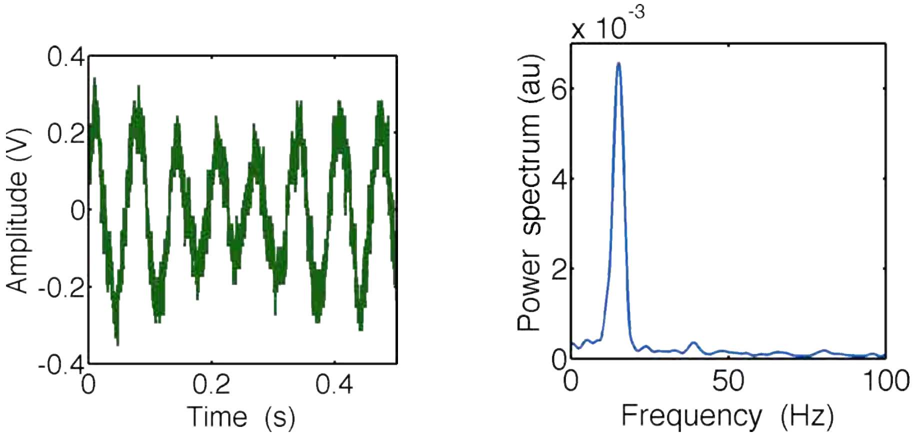

(a) (b)

Figure 4.6: (a) Raw signals detected by the photodetector as acquired by the oscilloscope when the particle moving in a circular motion with $\Omega = 16.36\, s^{-1}$, is being illuminated by a beam with a helical phase $\phi = 2\pi\ell$ with topological charge $\ell = 4$. (b) Power spectra obtained with an FFT algorithm after being processed. The peaks in (c) and (d) correspond to the Doppler frequency shifts of $\ell\Omega/(2\pi) = 2.60 Hz$ and $10.41 Hz$, respectively. See text for further details.

Transverse rectilinear motion

Fig. 4.7 shows results for the case of a particle moving with constant rectilinear velocity v illuminated by a signal beam with a uniform phase gradient profile ($\Psi = \gamma x$). This uniform gradient phase profile, generated by the SLM, tilts the incident Gaussian beam into different angles. The Doppler shift expected from Eq. (4.5) is $\Delta f = \gamma \mathrm{v}/(2\pi)$, which shows a linear dependence on both velocity and phase gradient of the light beam. Fig. 4.7(a) shows the dependence of the frequency shift on the velocity of the particle for a constant phase gradient $\gamma = 17.92\,\mathrm{mm}^{-1}$, and Fig. 4.7(b) shows the dependence of the frequency shift for different phase gradients, for a particle that moves with velocity v = 4.68 mm/s. Notice the high degree of agreement between theory (dots) and experiment (line) for both cases.

Transverse rotational motion

Fig. 4.8 shows the case of a particle moving in a circular path with a constant angular velocity Ω. In this case, the most convenient phase profile to retrieve the value of the angular velocity is the one corresponding to a Laguerre-Gauss beam with winding number ℓ. From Eq. (4.7), the phase profile given by $\Psi(\phi) = \ell\phi$ has an expected Doppler shift of $\Delta f = \ell\Omega/(2\pi)$. Similarly to the previous case, the Doppler frequency shift shows a linear dependence on both the angular velocity and the winding number ℓ. Fig. 4.8(a) shows the linear dependence of the frequency shift on the angular velocity of the target for $\ell = 3$, and Fig. 4.8(b) shows the dependence on ℓ for a target that moves with angular velocity $\Omega = 16.36\, s^{-1}$. In general, one can detect arbitrary transverse velocities by engineering phase profiles. Figs. 4.7 and 4.8 are examples of how a choice of the appropriate phase profile for a particular type of movement can give simple relationships between the velocity and the Doppler frequency shift.

The approach proposed here can also be considered for other types of measurements, as in the case of the motility of single-cells or simple multicellular organisms. For a typical value of motility of a biological specimen of tens of micrometers per second [8], a local spatial modulation of ~

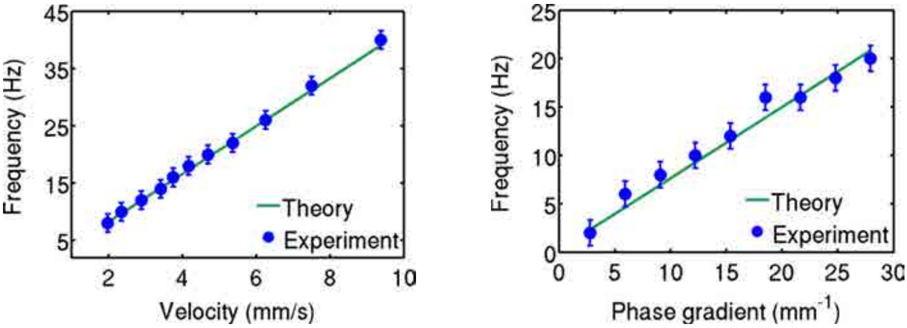

(a) (b)

Figure 4.7: Detected frequency shifts when the target moves in a rectilinear path. (a) The target is set to move at different rectilinear velocities when illuminated by a beam with a linear phase gradient of $\gamma = 17.92$ mm^{-1}. (b) The target moves under the illumination of a beam with different linear phase gradients γ at a constant linear velocity of v = $4.68\, mm/s$.

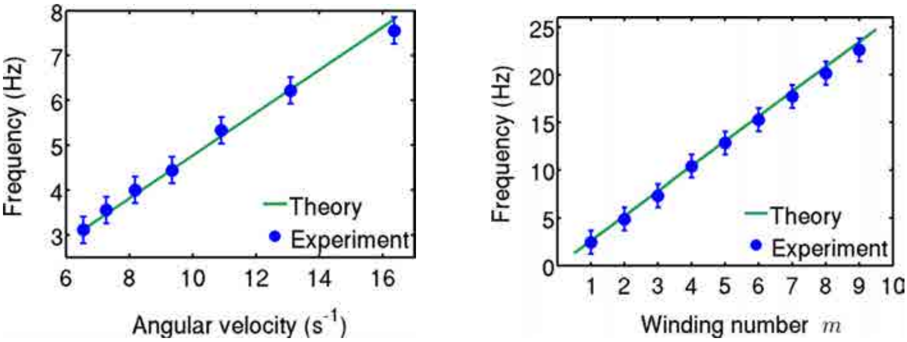

(a) (b)

Figure 4.8: Detected frequency shifts when the target moves in a circular path. (a) The target is set to move at different circular velocities when illuminated by a beam with a helical phase of $\phi = 6\pi$, corresponding to $\ell = 3$. (b) The target moves at a constant circular velocity of $\Omega = 16.36\, s^{-1}$. The particle is illuminated with a phase gradient $\phi = 2\pi\ell$, where ℓ is the winding number.

1 μm^{-1} would yield a Doppler frequency shift of some tens of hertz. This scheme can also be used to measure fluid flows in live tissue, where the possibility of inducing tiny phase gradients that would not affect the in vivo system under study can be of great interest. For instance, the diagnosis of certain important eye diseases can be assessed by observing abnormal retinal blood flow [9]. Notice that typical blood flow velocities in the retina are in the range of some tens of mm/s. Using phase gradients of ~ 0.1 μm^{-1} would result in Doppler shifts of several KHz.

4.3 Direction sensitive transverse velocity measurement by phase modulated structured light

In previous sections, we demonstrated experimentally that targets moving in a plane perpendicular to the direction of illumination can induce a velocity-dependent frequency shift to structured light beams, *i.e.*, beams with appropriate transverse phase profile [11, 10, 12]. This frequency shift, enables the determination of the velocity component perpendicular to the illumination axis (*transverse* *velocity*). The value of the generated frequency shift depends on both the velocity of the target and the phase profile imprinted on the light beam. For the case of a purely rotational motion with angular velocity Ω_t, the appropriate phase gradient of the illuminating beam should preferably have circular symmetry, such as in the case of a Laguerre-Gauss beam

$$E(\rho, \phi, t) = U(\rho)\exp(ikz + i\ell\phi - i\omega t) + H.c., \tag{4.12}$$

where $H.c.$ means Hermitian conjugate, z is the direction of propagation of the light beam, $\omega = ck$ is the angular frequency, k is the wavenumber, ρ and ϕ are the radius and the azimuthal angle in cylindrical coordinates respectively, $U(\rho)$ is the radial profile and ℓ the winding number. In this case, the frequency shift Δf is given by [11],

$$\Delta f = \frac{\ell\Omega_t}{2\pi}. \tag{4.13}$$

The validity of this expression has been experimentally demonstrated in two recent experiments [10, 12]. In [10], the target was illuminated with two co-propagating beams with opposite winding numbers, $+\ell$ and $-\ell$, and the beating frequency of both beams was measured. In [12], Δf is determined through an interferometric technique where light reflected from the moving target is made to interfere with a reference signal. In both cases a linear dependence of the wind number ℓ with the frequency shift Δf was reported. Since most photodetectors are sensitive to light intensity alone and the detection systems are interferometric in nature, only the absolute value of the difference between the frequency of the reflected and the reference light can be obtained, *i.e.* there is no indication of whether the received scattered wave is upshifted or downshifted in frequency with respect to the frequency of the incident beam. Therefore, information about the direction of motion -clockwise or anti-clockwise in the case of rotational motion- is not available. Well known techniques for direction-sensitive velocity measurements are generally based on the generation of an optical frequency offset between the illumination and the reference beam (*heterodyne detection*) or between the two illumination beams. For this purpose, the use of mechanically rotating wave-plates [13] or diffraction gratings [14] have been extensively reported. Other techniques employ acousto-optic modulators[15] or electro-optic frequency shifters [16]. In general, these systems should be customized for a particular beam size and specific frequency.

In this section we put forward a novel method that allows to discriminate velocity direction based on the use of properly modulated beams of structured phase [17]. In a sense, the scheme described here plays a similar role in the transverse plane to the role of an acousto-optic modulator, which dynamically changes the phase along the propagation direction of the source light beam (*longitudinal phase*) modifying its frequency. In our method, the phase change takes place in the transverse plane of the illuminating beam. The significance of this method lies on the facts that: 1) absolute velocity directions can be determined easily; and 2) it does not require the use of additional components other than a dynamic and configurable optical beam generator. Here, we applied our method to a specific case: rotation of micro-particles. This technique can easily be generalized to other types of motion by proper tailoring and controlling of the movement of the phase of the illumination beam.

For example, in the special case of a rotating target, a rotating helical-phased beam can be used to extract information about its rotation sense. The phase of the beam now takes the form $\Psi(t) = \ell\phi \pm \ell\Omega_s t$, where Ω_s is the velocity of rotation of the phase [see Fig. 4.9(a)]. The time-varying light beam can be obtained by sequentially displaying holograms calculated for different rotated CGHs. A sample of the fork-like hologram displayed in the Spatial Light Modulator is shown in Fig. 4.9(b). Figure 4.9(c) shows the experimental intensity profile of the Laguerre-Gaussian mode with winding number $\ell = 10$. Figure 4.9(d) shows the experimental interference pattern of the LG beam with a Gaussian beam featuring ten petals. The phase jumps from 0 to 2π ten times as one goes from $\phi = 0$ to $\phi = 2\pi$.

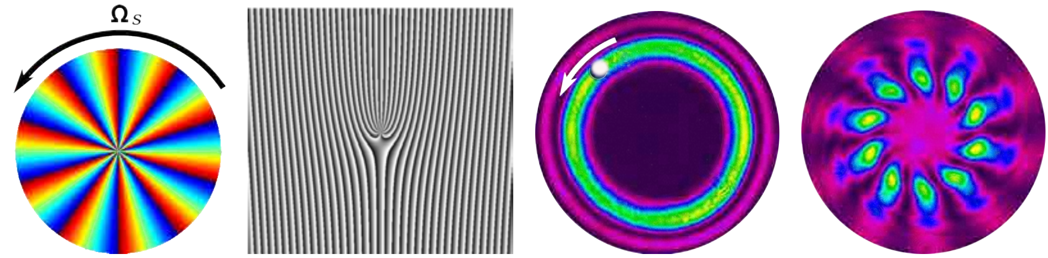

(a) (b) (c) (d)

Figure 4.9: (a) The illuminating beam's phase is rotated either clockwise or anti-clockwise with angular velocity Ω_s. The phase changes from zero (blue) to 2π (red) ten times around the azimuth. (b) Fork-like hologram displayed in the SLM to generate the LG_0^{10} mode. (c) Experimental intensity profile of the generated beam (4mm in diameter). The target, a 70 μm in diameter disk-like particle (shown here exaggerated for illustrative purposes) rotates around the LG_0^{10} beam in the region of maximum intensity. (d) Interference pattern between the LG_0^{10} and a Gaussian beam obtained in experiments.

The frequency shift of the light reflected back from the target is now given by,

$$\Delta f' = \frac{\ell(\Omega_t - \Omega_s)}{2\pi}. \tag{4.14}$$

One has $|\Delta f'| < |\Delta f|$ when both Ω_t and Ω_s have the same sign, whereas $|\Delta f'| > |\Delta f|$ when they have opposite signs. A higher frequency shift will be measured when the target rotates in the opposite direction of the beam.

We extract the Doppler frequency shift imparted by the moving particles via an interferometric technique using the modified Mach-Zehnder interferometer shown in Fig. 4.10. A 15 mW continuous wave He-Ne laser (Melles-Griot, $\lambda = 632.8$ nm) is spatially filtered and expanded to a diameter of 5 mm , using a lens combination of focal lengths $F_1 = 25$ mm and $F_2 = 100$ mm for the front and back lenses, respectively, and a 30 μm pinhole placed at the middle focus. This beam is split into two (*signal* and *reference* beams) using a polarizing beam splitter (PBS1). A mirror (M1) redirects the signal beam to a SLM that imprints the beam with the desired phase profile. The first diffracted order of a fork-like hologram [Fig. 4.9(b)] encoded into the SLM is used to illuminate the target while the rest are spatially filtered (SF) using two lenses of focal lengths $F_3 = 50$ mm and a 200μm pinhole placed at the middle focus. The diameter of the LG_0^ℓ beam is generally several times larger than the size of the particle to ensure the particle moves in the phase gradient generated by the light beam while rotating around it. In our case, the beam and the particle diameters are 4 mm and 70 μm, respectively. A second polarizing beam splitter (PBS2) in combination with a quarter-wave plate (QWP) collects light reflected from the target back into the interferometer. These reflections are afterwards interfered with the reference signal using a beam splitter (BS). A balanced detection scheme is implemented with two photodetectors PD1 and PD2 to improve the signal-to-noise ratio. An optical chopper (OC) placed in the path of the signal beam shifts our detected frequency from Hz to kHz, so that we can work far from the low frequency noise. An autocorrelation process that cross-correlates the signal with itself to find periodic patterns obscured by noise, allows us to enhance the signal-to-noise ratio. The resulting signal is Fourier transformed to find the frequency content. Hamming windowing and zero padding are also applied to smooth the Fourier spectrum. The rotation of the particles was mimicked using a Digital Micro-mirror Device (DMD) as in [12]. For this experiment we used an array of 7x14 micro-mirrors to simulate a disk-like particle of 70 μm in diameter. Its rotation was produced by displaying N consecutive binary images of the particle at positions separated from the previous one by an amount $\Delta\theta = 2\pi/N$, in our case was N=96. Hence, the angular velocity will be $\Omega_t = \Delta\theta/\Delta t = 2\pi/(NT)$, with T the time interval between consecutive images.

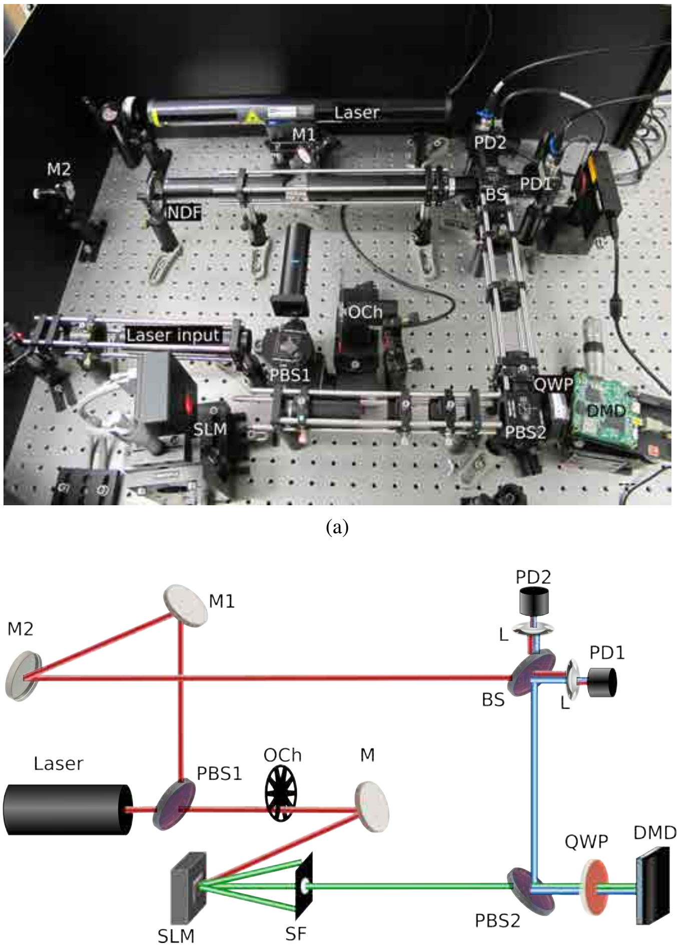

(a)

(b)

Figure 4.10: Experimental setup to extract the rotation velocity and its sense of direction. PBS: polarizing beam splitter; M: mirror; L: lens; PD: photodetector; SLM: Spatial Light Modulator; SF: spatial filter; QWP: Quarter-Wave Plate; DMD: Digital Micro-mirror Device. *See text for details.*

Different methods have been reported in order to implement the beam's rotation [18, 19, 20, 21]. Here we programmed the SLM to display images of the fork-like hologram that produces the LG_0^{10} mode. In each image, the phase appears rotated by an amount $\Delta\phi = 2\pi/\eta$, where η is an integer number. The time from one image to the next is the refresh rate τ of the SLM. The angular velocity of rotation of the phase can then be computed as $\Omega_s = 2\pi/(\eta\tau)$. In order to increase (decrease) the angular velocity Ω_s, we can increase (decrease) η or τ. In any case, η should be larger than 2ℓ to avoid aliasing in the generated signal. Even though most commercially available SLMs have limited frame refresh rate of 60 Hz, with the emerging technology of DMDs, refresh rates of up to 4 KHz can be achieved [22, 23].

Figure 4.11 shows the spectra produced when an LG_0^{10} beam with a static phase, and an LG_0^{10} beam with rotating phase at different angular speed impinges upon a rotating particle. The speed of rotation of the phase was varied from negative to positive values. With a static phase, the frequency shift is induced only by the rotation of the particles as expected [Fig. 4.11(a)]. The particle rotates at an angular velocity $\Omega_t = 3.27s^{-1}$ hence, for this speed, the frequency shift obtained is $\Delta f = 5.29 \pm 0.27s^{-1}$ (error estimation given by the typical standard deviation of ten measurements). +This frequency decreases when the phase is rotated in the same direction as the rotation sense of the particle [Fig.4.11(b)-(d)], while it increases when the phase is rotated in the opposite direction [Fig.4.11(e)-(g)]. Moreover, the amount of frequency shift with respect to a non-rotating phase is determined by the rate of the rotation of the LG_0^{10} phase. Direction sensitivity is clear as the frequency is upshifted or downshifted based on the relative direction of rotation of the LG_0^{10} phase. All our frequencies are referenced to the chopper frequency (1 KHz).

In Figure 4.12, we plot the frequency shift $\Delta f'$ as function of the velocity of rotation of the phase (Ω_s). We do this for two possible directions of rotation, clockwise ($\Omega_t < 0$) and anti-clockwise ($\Omega_t > 0$). According to Eq. (4.14) there is a linear relationship between $\Delta f'$ and Ω_s. This is clearly observed in Fig. 4.12 for two cases: $\Omega_t > 0$ and $\Omega_t < 0$. As in Fig. 4.11, the point labeled (a) corresponds to a static phase ($\Omega_s = 0$), whose corresponding frequency shift is $\Delta f = 5.29 \pm 0.27s^{-1}$. From ($b$) to ($e$) the phase rotates anti-clockwise ($\Omega_s < 0$) with increasing angular velocities, whereas from (f) to (i) it rotates in the opposite direction $\Omega_s > 0$, again with increasing angular velocities.

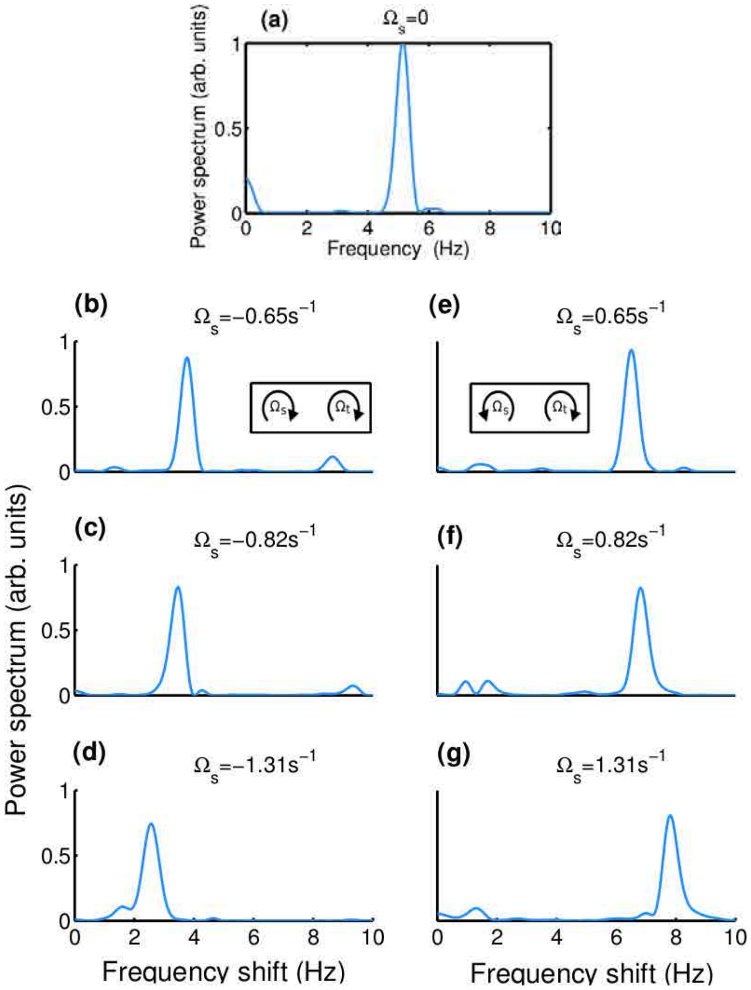

Figure 4.11: Fourier spectrum obtained when an LG_0^{10} impinges on a particle rotating at an angular velocity $\Omega_t = 3.27s^{-1}$. On (a) the phase is static. From (b) to (d) the phase of the LG_0^{10} is rotated counterclockwise with increasing angular velocities. From (e) to (g) it is rotated clockwise, also with increasing angular velocities.

Whenever Ω_t and Ω_s have opposite signs, the generated frequency shift $\Delta f'$ will be larger than Δf. Conversely, if they have the same sign, the frequency shift will be smaller.

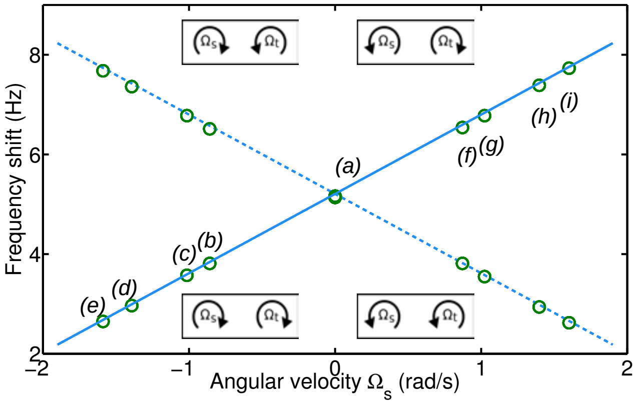

Figure 4.12: Frequency shift as function of the angular velocity of the phase gradient of the illuminating beam. The particle rotates clockwise (solid line) or anti-clockwise (dashed line).

Figure 4.12 can be considered a description of the measurement method. For a given value of the sought-after Ω_t, changing the velocity Ω_s in a controlled way with a programmable spatial phase modulator allows detection of the frequency shift as a function of Ω_s. The dashed line (negative slope) corresponds to a particle with anti-clockwise rotation ($\Omega_t > 0$), while the continue line (positive slope) corresponds to a particle rotating clockwise ($\Omega_t < 0$). Here, for the sake of simplicity, we have only presented results for $\ell = 10$. Similar results are obtained for different values of ℓ, that confirm the linear dependence between the winding number ℓ and the frequency shift ΔF stated in Eq. (4.14).

To summarize, we have presented the experimental demonstration of a direction-sensitive velocity measurement method that uses frequency shifts induced by dynamic structured light beam illumination. In addition to the frequency shifts induced by the moving target under investigation, the frequency is upshifted or downshifted based on the relative direction between the target's movement and the movement of the phase. This enables the detection of the absolute direction of the target's movement. The method is easy to implement since it does not require the use of additional optical elements. It uses the same device that generates the structured light beam. In particular, we implemented the method by obtaining the rotational velocity, its absolute value and its sign, of a rotating particle employing optical beams with a rotating helical phase. This method can be generalized to more complex movements, beyond the rotating targets considered here, by properly tailoring the structured illumination beam. For example, the method presented in [24] can take advantage of this technique to fully characterize a three dimensional motion.

4.4 Measuring the translational and rotational velocities of particles in helical motion.

The search for reliable methods to detect the velocity of micro- and nano-particles, and microorganisms in a three-dimensional (3D) motion is challenging and is continually being addressed [25, 26, 27]. Certainly, the ability of quantifying the full velocity of a particle's movement opens new possibilities. For example, it can unveil some of the most intriguing biomechanical causes and ecological consequences of particle movement such as in helical swimming [28, 29]. Nearly all aquatic microorganisms smaller than 0.5 mm long, exhibit helical swimming paths either in search for food, to move toward appropriate temperature or pH, or to escape from predators. These paths are inherently three-dimensional [30]. This is the case of sperm when traveling towards the ovum. These specific characteristics of the movement should be taken into account when creating fertilization models [31, 32]. To characterize 3D motion, researchers usually extend two-dimensional (2D) measurement schemes, commonly based on standard optical systems such as video cameras and microscopes [33]. Other researchers employ numerical analysis [34, 35] or digital holography with extensive numerical computations [36].

Here we demonstrate that the recently introduced technique to measure directly transverse velocity components using structured light as illumination source can also be used to detect all velocity components in a full 3D helical motion. This is a two-step technique wherein we first illuminate the target with a Gaussian mode to determine its translation velocity. Then we change the illumination to an LG_0^ℓ mode to obtain the velocity of rotation. When the direction of translation is known, it is possible to determine the sense of rotation by simply reversing the sign of the mode index ℓ of the LG_0^ℓ mode. Conversely, if we know the sense of rotation, we can compute the direction of translation, again by reversing the sign of ℓ. Even though we implemented the technique in two steps, one can envision illuminating the target with two beams simultaneously.

4.4.1 Theoretical framework

In the classical non-relativistic scheme, light reflected from a moving target is frequency shifted proportional to the target's velocity as $\Delta f_{\|} = 2|\mathbf{v}|cos(\theta)/\lambda$, where λ is the wavelength of light and θ is the angle between the velocity $\mathbf{v}$ of the target and the direction of propagation of the light beam. Under structured light illumination, the phase along the transverse plane is no longer constant. Therefore in the presence of a transverse velocity component, the frequency shift will have an additional term given by [11]

$$\Delta f = \Delta f_{\|} + \Delta f_{\perp} = \frac{1}{2\pi}(2k\mathrm{v}_z + \nabla_{\perp}\Psi \cdot \mathbf{v}_{\perp}), \tag{4.15}$$

where v_z is the velocity of the target along the line of sight, $\mathbf{v}_{\perp}$ is the velocity in the transverse plane, $k = 2\pi/\lambda$ is the wave vector and $\nabla_{\perp}\Psi$ is the transverse phase gradient.

Helical motion is a combination of a translation along the line of sight and a rotation in the transverse plane [Fig. 4.13(c)]. Therefore, the use of an azimuthally varying phase $\Psi = \ell\phi$, present in an LG beam [Fig. 4.13(a) and (b)], simplifies the determination of the angular velocity of rotation.

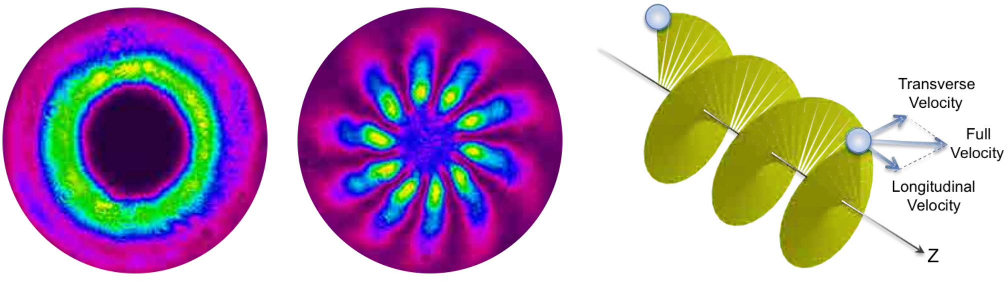

(a) (b) (c)

Figure 4.13: (a) Intensity profile of the LG_0^{10} beam illuminating the Digital Micromirror Device (DMD). (b) Interference of the LG_0^{10} beam with the reference beam. The 10 lobes observed are due to the phase profile $\Psi = 10\phi$. (c) Schematic representation of the helical trajectory followed by particles. Z is the propagation axis of the beam.

Here, ϕ is the azimuthal angle and ℓ is the number of 2π phase jumps of the light beam as one goes around ϕ. The second term of Eq. (4.15) becomes $\nabla_\perp \Psi \cdot \mathbf{v}_\perp = \ell\Omega$, so that

$$\Delta f = \frac{1}{2\pi}(2k\mathrm{v}_z + \ell\Omega). \tag{4.16}$$

Two aspects of this equation should be highlighted. First, if we illuminate with a Gaussian mode ($\ell = 0$), as most radar Doppler systems do, $\Delta f = \Delta f_{||} = k\mathrm{v}_z/\pi$ and the translational velocity can be determined. Second, Δf depends on the relative signs of v_z, ℓ and Ω. It will acquire maximum value when v_z and $\ell\Omega$ have the same signs and a minimum value when they have opposite signs. Moreover, the larger the value of ℓ, the larger is the frequency shift observed.

4.4.2 Experimental implementation

Experimental setup

We extract the Doppler frequency shift imparted by the moving particles via an interferometric technique using the modified Mach-Zehnder interferometer shown in Fig. 4.14(a). A $15mW$ continuous wave He-Ne laser ($\lambda = 632.8$nm) is spatially filtered and expanded to a diameter of 5mm. This beam is split into two (*signal* and *reference*) using a polarizing beam splitter (PBS1). A mirror (M1) redirects the signal beam to a Spatial Light Modulator (SLM) that imprints the beam with the structured phase, as shown in Fig. 4.13. The first diffracted order of the fork-like hologram encoded into the SLM is used to illuminate the target while the rest of the diffracted orders are spatially filtered (SF). A second polarizing beam splitter (PBS2) in combination with a quarter-wave plate (QWP) collects light reflected from the target back into the interferometer. The light reflected interferes with the reference signal using a beam splitter (BS).

A balanced detection is implemented with two photodetectors (PD1 and PD2), connected to an oscilloscope (TDS2012 from Tektronix). To eliminate most of the low-frequency noise, an optical chopper (OCh) placed in the path of the signal beam shifts our detected frequency from Hz to kHz. Figure 4.14(b) shows a typical signal resulting from the difference of the signals detected from output ports PD1 and PD2. An autocorrelation process allows us to improve the signal-to-noise ratio significantly by finding periodic patterns obscured by noise [Fig. 4.14(c)]. The signal is Fourier transformed to find the fundamental frequency content. Hamming windowing and zero padding are applied to smooth the Fourier spectrum shown in Fig. 4.14(d).

To generate the helical motion of particles, we employed a Digital micromirror device (DMD). A cluster of 512 diamond-shape squares ($10 \times 10\,\mu$m) randomly distributed within a circular area with a diameter of 3 mm was set to rotation as a solid body in a similar way to [12]. The DMD was attached to a translation stage (BP1M2-150 from Thorlabs, with a maximum displacement of 150 mm), aligned perpendicularly to the plane of rotation of the DMD. The axis of the illumination beam is aligned to coincide with the axis of the helical trajectory.

Due to the interferometric nature of the experimental set up, we can measure only $|\Delta f|$. However, since the frequency shift given by Eq. (4.16) is dependent on the relative signs of v_z, ℓ, and Ω, we can determine the absolute magnitudes of $|\Delta f_{||}|$ and $|\Delta f_\perp|$, and consequently $|\mathrm{v}_z|$, $|\Omega|$ and the relative sign between v_z and Ω. The frequency shifts always fulfill $|\Delta f| > |\Delta f_{||}|$ for v_z and $\ell\Omega$ showing the same sign, while $|\Delta f| < |\Delta f_{||}|$ for v_z and $\ell\Omega$ showing opposite signs. Therefore, if $|\Delta f|$ is larger for $\ell > 0$ than for $\ell < 0$, v_z and Ω have the same sign, while if is smaller, v_z and Ω have opposite signs. The important point is that the sign of ℓ is a free parameter imposed on the illumination beam chosen in the experiment. The experimental procedure to measure $|\mathrm{v}_z|$, $|\Omega|$ and the sign of $\mathrm{v}_z \cdot \Omega$ is thus to choose a beam with $\ell = 0$ to obtain $|\Delta f_{||}|$, use afterward a *LG* beam with the sign of the index ℓ so that it maximizes $|\Delta f|$, and obtain $|\Delta f_\perp| = |\Delta f| - |\Delta f_{||}|$. Furthermore, if $\ell > 0$, we have $\mathrm{v}_z \cdot \Omega > 0$, and $\mathrm{v}_z \cdot \Omega < 0$ otherwise. Previous knowledge of the sign of v_z, for instance knowing that the particle or microorganism under study advances in a fluid stream, allows to determine the sign of Ω.

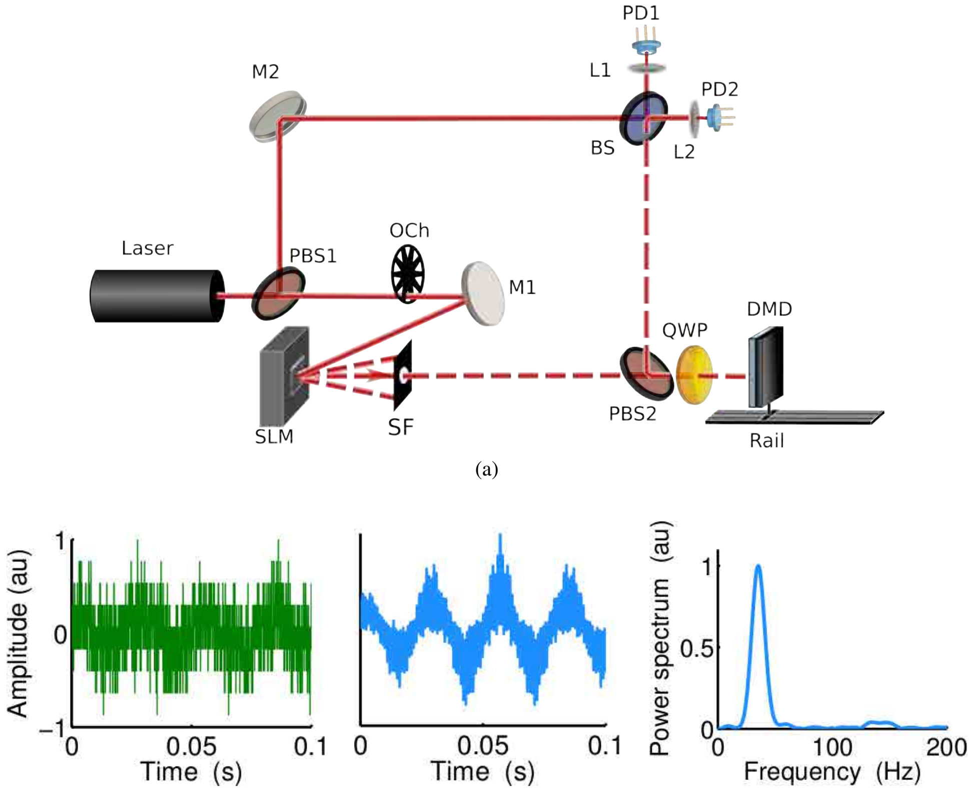

(a)

(b) (c) (d)

Figure 4.14: (a) Experimental setup. (b) Raw signal after balanced detection. (c) Autocorrelation function of the signal. (d) Power spectral density. We only show the spectrum above the chopping frequency. PBS: polarizing beam splitter; M: mirror; L: lens; PD: photodetector; SLM: Spatial Light Modulator; SF: spatial filter; OCh: optical chopper; QWP: Quarter-Wave Plate; DMD: Digital Micromirror Device. *See text for details.*

Experimental results

In our experiments, we first illuminate the helically moving particles with a Gaussian beam. Here, $\Delta f = \Delta f_{||}$ since the particles experiences a constant phase along the transverse plane. Figure 4.15 shows the experimental results. We do all possible combinations: $\mathrm{v}_z > 0$ (forward, moving away from the illuminating source) with negative [Fig. 4.15(a)] and positive [Fig. 4.15(c)] rotations, as well as $\mathrm{v}_z < 0$ (backwards, moving towards the illuminating source) with negative [Fig. 4.15(d)] and positive [Fig. 4.15(f)] rotation. Positive (negative) rotation refers to counterclockwise (clockwise) rotation for an observer looking towards the illumination source. For the sake of comparison, we also show the spectra when particles translate without any rotation for both $\mathrm{v}_z > 0$ and $\mathrm{v}_z < 0$ [Figs. 4.15(b) and 4.15(e), respectively]. The frequency shift measured, $|\Delta f_{||}| = 31.6\ \mathrm{s}^{-1}$, is the same in all cases, regardless of the relative signs of v_z and ℓ. From this information, computing the translational velocity is straight forward using Eq. (4.16). The velocity we obtained is $|\mathrm{v}_z| = \pm 10\,\mu m/s$, exactly the same as the velocity we programmed our rail to move. This leaves only the rotational velocity unknown.

Figures 4.16 and 4.17 show experimental results when the moving particles are illuminated by an LG_0^ℓ mode with $\ell = \pm 10$. With any value of ℓ we would obtain similar results. The presence of some lower-intensity secondary peaks is attributed to the remaining low-frequency noise still present

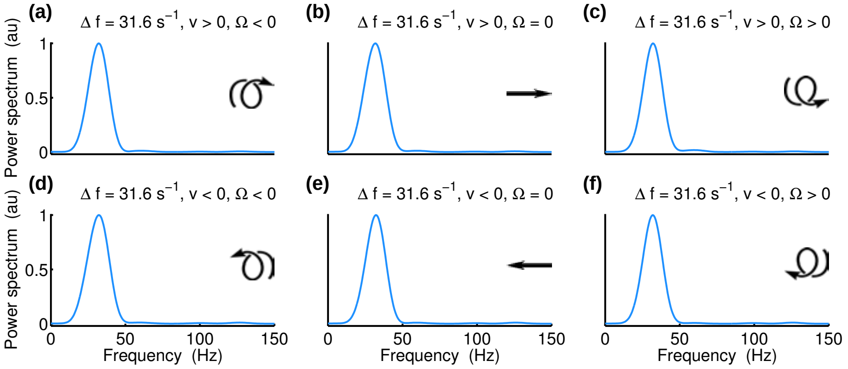

Figure 4.15: Frequency shift measured under illumination with a Gaussian mode ($\ell = 0$) for any direction of translation ($v_z > 0$ and $v_z < 0$), and any sense of rotation ($\Omega > 0$ and ($\Omega < 0$). For the sake of comparison, the case with $\Omega = 0$ is also shown.

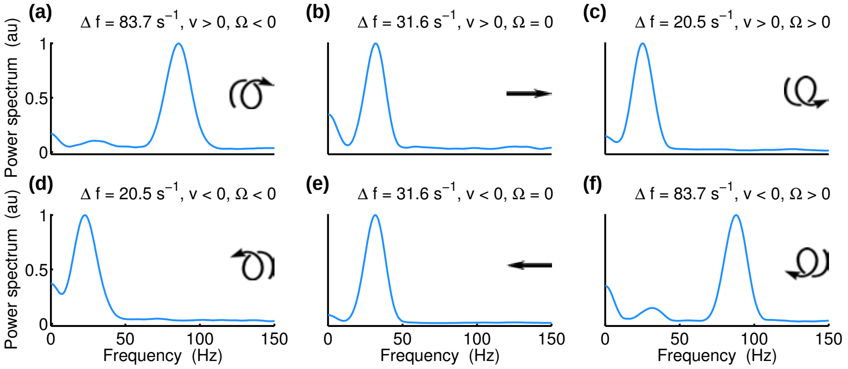

Figure 4.16: Frequency shift measured under illumination with a LG_0^{-10} mode for $v_z > 0$ and $v_z < 0$, and for $\Omega > 0$ and ($\Omega < 0$.

in the detection system. For $\ell = -10$ (Fig. 4.16) and $v_z > 0$, Δf is larger if the particles rotate with $\Omega < 0$ [Figs. 4.16(a)], while it is smaller if the particles rotate in the opposite direction ($\Omega > 0$) [Fig. 4.16(c)]. The frequency shifts measured are Δf = 83.7 s^{-1} and Δf =20.5 s^{-1} for $\Omega < 0$ and $\Omega > 0$, respectively. By accounting these and using the procedure described above, we can compute $\Delta f_\perp$ due to the rotation of the particles according to Eq. (4.16). In all cases, $|\Delta f_\perp|$ = 52.1 s^{-1}, yielding an angular velocity of $|\Omega|$ =32.7s^{-1}. Conversely, when the particles move backwards ($v_z < 0$), Δf is larger for $\Omega > 0$ [Fig. 4.16(f)], while it is smaller for $\Omega < 0$ [Fig. 4.16(d)]. On the contrary, if we illuminate with LG_0^{10}, we observe a larger Δf when either $v_z > 0$ and $\Omega > 0$ [Fig. 4.17(c)] or $v_z < 0$ and $\Omega < 0$ [Fig. 4.17(d)]. We also show the spectra when the particles move forward [Fig. 4.16(b) and 4.17(b)] or backward [Figs. 4.16(e) and 4.17(e)] without rotation ($\Omega = 0$).

In short, we have measured the full velocity of particles moving in a helical motion by using the frequency shift generated by reflecting particles moving in a structured light beam, i.e., a beam with an engineered transverse phase profile. The technique requires choosing the appropriate spatial mode as the illumination beam, depending on the particular type of movement under investigation. First, we determine the longitudinal velocity component by illuminating with a Gaussian mode and afterwards, we use an LG_0^ℓ mode to obtain the angular velocity of the rotation. The translational and rotational velocities used in our experiment are within the range of velocities common to biological specimens. Human sperm for example, has helical rotation speeds ranging from ~ 18 to 120 s^{-1}

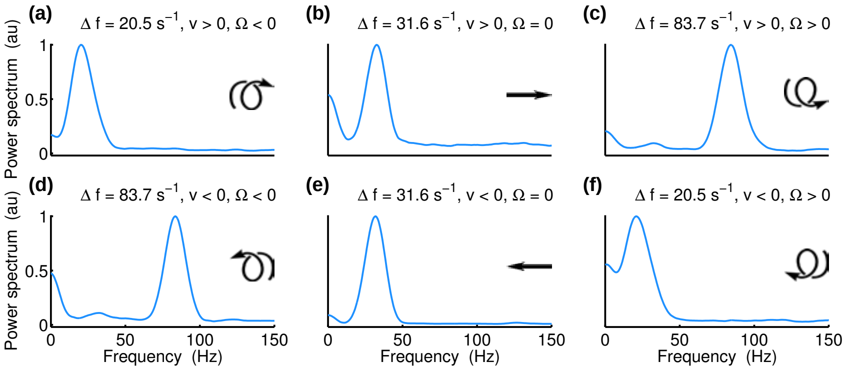

Figure 4.17: Frequency shift measured under illumination with a LG_0^{10} mode for $v_z > 0$ and $v_{HZ} < 0$, and for $\Omega > 0$ and ($\Omega < 0$.

and linear speeds of approximately 20 to 100$\mu m/s$ [37]. The technique can be generalized to other types of motion by selecting appropriately the transverse phase profile of the illuminating beam and can also be implemented in other frequency bands. For example, the microwave band is of special interest for detecting transverse velocities of macroscopic objects.

References

[1] R. M. Measures, *Laser Remote Sensing: Fundamentals and Applications* (Krieger Publishing Company, 1992).

[2] F. Durst, B. M. Howe, and G. Richter, "Laser-Doppler measurement of crosswind velocity," Appl. Opt. **21**, 2596–2607 (1982).

[3] A. Sommerfeld, *Lectures on theoretical physics: Optics* (Academic Press, 1954).

[4] A. Belmonte and J. P. Torres, "Optical Doppler shift with structured light." Optics letters **36**, 4437–9 (2011).

[5] M. P. J. Lavery, S. M. Barnett, F. C. Speirits, and M. J. Padgett, "Observation of the rotational Doppler shift of a white-light, orbital-angular-momentum-carrying beam backscattered from a rotating body," Optica **1**, 1–4 (2014).

[6] G. Nienhuis and L. Allen, "Paraxial wave optics and harmonic oscillators," Phys. Rev . A **48**, 656–665 (1993).

[7] L. Allen, M. W. Beijersbergen, R. J. C. Spreeuw, and J. P. Woerdman, "Orbital angular momentum of light and the transformation of Laguerre-Gaussian laser modes," Phys. Rev. A **45**, 8185 (1992).

[8] Y. R. Chemla, H. L. Grossman, T. S. Lee, J. Clarke, M. Adamkiewicz, and B. B. Buchanan, "A new study of bacterial motion: superconducting quantum interference device microscopy of magnetotactic bacteria," Biophys. J. **76**, 3323–3330 (1999).

[9] Y. Wang, B. Bower, J. Izatt, O.Tan, and D. Huang, "In vivo total retinal blood flow measurement by Fourier domain Doppler optical coherence tomography," J. Biomed. Opt. **12** (2007).

[10] M. P. J. Lavery, F. C. Speirits, S. M. Barnet, and M. J. Padgett, "Detection of Spinning Object Using Light's Orbital Angular Momentum," Science **341**, 537–540 (2013).

[11] A. Belmonte and J. P. Torres, "Optical Doppler shift with structured light," Opt. Lett. **36**, 4437–4439 (2011).

[12] C. Rosales-Guzmán, N. Hermosa, A. Belmonte, and J. P. Torres, "Experimental detection of transverse particle movement with structured light," Sci. Rep. **36**, 2815 (2013).

[13] G. E. Sommargren, "Up/down frequency shifter for optical heterodyne interferometry," J. Opt. Soc. Am. **65**, 960–961 (1975).

[14] W. H. Stevenson, "Optical Frequenfy Shifting by means of a rotating diffraction grating," Appl. Opt. **9**, 649–652 (1970).

[15] P. Gangding, H. Shangyuan, and L. Zonggi, "Application of electro-optic frequency shifters in heterodyne interferometric systems," Electron. Lett. **22**, 1215–1216 (1986).

[16] R. N. Shagam and J. C. Wyant, "Optical frequency shifter for heterodyne interferometers using multiple rotating polarization retarders," App. Opt. **17**, 3034–3035 (1978).

[17] C. Rosales-Guzmán, N. Hermosa, A. Belmonte, and J. P. Torres, "Direction-sensitive transverse velocity measurement by phase-modulated structured light beams," Opt. Lett. **18**, 5415–5418 (2014).

[18] J. Courtial, K. Dholakia, D. A. Robertson, L. Allen, and M. J. Padgett, "Measurement of the Rotational Frequency Shift Imparted to a Rotating Light Beam Possessing Orbital Angular Momentum," Phys. Rev. Lett. **80**, 3217–3219 (1998).

[19] L. Chen and W. She, "Sorting photons of different rotational Doppler shifts (RDS) by orbital angular momentum of single-photon with spin-orbit-RDS entanglement," Opt. Express **16**, 14629–14634 (2008).

[20] A. Bekshaev, M. Soskin, and M. Vasnetsov, "Angular momentum of a rotating light beam," Opt. Commun. **249**, 367–378 (2005).

[21] C. N. Alexeyev and M. A. Yavorsky, "Angular momentum of rotating paraxial light beams," J. Opt. A: Pure Appl. Opt. **7**, 416–421 (2005).

[22] M. Mirhosseini, O. S. Magana-Loaiza, C. Chen, B. Rodenburg, M. Malik, and R. Boyd, "Rapid generation of light beams carrying orbital angular momentum ," Opt. Express **21**, 30204–30211 (2013).

[23] I. R. Perch-Nielsen, P. J. Rodrigo, and J. Glückstad, “High-speed phase modulation using the RPC method with a digital micromirror-array device ,” Opt. Express **14**, 5588–5593 (2006).

[24] C. Rosales-Guzmán, N. Hermosa, A. Belmonte, and J. P. Torres, “Measuring the translational and rotational velocities of particles in helical motion using structured light,” Opt. Express **22**, 16504–16509 (2014).

[25] A. Guerrero, J. Carneiro, A. Pimentel, C. D. Wood, G. Corkidi, and A. Darszon, “Strategies for locating the female gamete: the importance of measuring sperm trajectories in three spatial dimensions,” Mol. Hum. Reprod. **17**, 511–523 (2011).

[26] R. N. Bearon, “Helical swimming can provide robust upwards transport for gravitactic single-cell algae; a mechanistic model,” J. Math. Biol. **66**, 1341–1359 (2013).

[27] H. C. Crenshaw, “A New Look at Locomotion in Microorganisms: Rotating and Translating,” Amer. Zool. **36**, 608–618 (1996).

[28] H. C. Crenshaw and L. Edelstein-Keshet, “Orientation by helical motion-II. Changing the direction of the axis of motion,” Bull. Math. Biol. **55**, 213–230 (1993).

[29] H. C. Crenshaw, “Orientyation by helical mtion-III. Microorganisms can orient to stimuly by changing the direction of their rotational velocity,” Bull. Math. Biol. **55**, 231–255 (1993).

[30] E. Lauga and T. R. Powers, “The hydrodynamics of swimming microorganisms,” Rep. Prog. Phys. **72**, 096601 (2009).

[31] G. S. Farley, “Helical nature of sperm swimming affects the fit of fertilization-kinetics models to empirical data,” Bio. Bull. **203**, 51–57 (2002).

[32] T. Su, I. Choi, J. Feng, K. Huang, E. McLeod, and A. Ozcan, “Sperm trajectories form chiral ribbons,” Sci. Rep. **36**, 1664 (2013).

[33] V. N. Thinh and S. Tanaka, “Speckle method for the measurement of helical motion of a rigid body,” Opt. acta **24**, 1171–1178 (1977).

[34] D. F. Katz and H. M. Dott, “Methods of measuring swimming speed of spermatozoa,” Reprod. Fertil. **45**, 263–272 (1975).

[35] E. Gurarie, D. Grünbaum, and M. T. Nishizaki, “Estimating 3D movements from 2D observations using a continuous model of helical swimming,” Bull. Math. Biol. **73**, 1358–1377 (2011).

[36] S. J. Lee, K. W. Seo, Y. S. Choi, and M. H. Sohn, “Three-dimensional motion measurements of free-swimming microorganisms using digital holographic microscopy,” Meas. Sci. Technol. **22**, 064004 (2011).

[37] T.-W. Su, L. Xue, and A. Ozcan, “High-throughput lensfree 3D tracking of human sperms reveals rare statistics of helical trajectories,” PNAS **109**, 1–5 (2012).

5

Nanostep height measurement via spatial mode projection

Contents

5.1 Common path interferometry 64
5.1.1 The quadrature condition 65
5.2 Spatial mode projection to measure layer thicknesses 66
5.3 Experimental demonstration 68
References 72

The search for new optical methods to measure thickness in the range of a few nanometers or even hundreds of picometers is a topic of great interest. This is fuelled not only by the desire to reach the limit of resolution on the use of light in the nanoworld, but also to develop new methods that can complement and/or substitute some well-established techniques, such as x-ray spectroscopy, atomic force microscopy, and ellipsometry [1]. Moreover, the continuous shrinking of all kinds of optical and electronic devices and the explosive growth of the exploration of the inner working of cells and molecular bio-machines demand detection techniques not only highly sensitive, but also noninvasive, faster, and easy to implement in different scenarios. These requirements can be met by photonics technologies.

Most of the time, high-resolution optical metrology is closely related to the evaluation of the phase of an electromagnetic field. In general, phases cannot be readily obtained and the desired information must be extracted indirectly by some other methods. The most widely used of these methods is interferometry. By looking at the intensity produced at the output port of an interferometer, the relative phase can be measured and consequently, the relative thickness of a layer. Phase differences up to 1×10^{-7} rad can be detected. The detection of small structures, such as a step [6], is more cumbersome since the reflected beam contains a spatially varying phase instead of a global phase that should be resolved. A major problem in interferometry is the presence of uncontrollable disturbances that can also introduce phase differences. This is especially critical when tiny phase changes are being measured. A way to circumvent this problem is by using a common path interferometer (CPI), described in the next section.

5.1 Common path interferometry

In CPI the reference beam and sample beams travel along the same path. Of particular interest are the self-referencing interferometers in which the reference wave is generated locally with respect to the signal wave so that the reference and signal waves experience common aberrations and path-length changes and thus maintain constant relative phase without the need for active stabilization of different light paths. This concept has been fully exploited in the compact disc technology [2]. In its more simplistic way, a compact disk is a collection of tracks of pits recessed from a surfaced called the land (positioned h= 1/4 of the wave-length higher than the pit). The information contained in the compact disk is read out in the far field by means of a focused laser with Gaussian profile,

$$u_i(\rho) = u(x,y) = \sqrt{\frac{2}{\pi W_0^2}} \exp\left[-\frac{\rho^2}{W_0^2}\right], \tag{5.1}$$

where W_0 is the beam waist. The Gaussian beam is focused with a lens such that half of the intensity straddles the pit and half the land. Without lose of generality, our analysis will be done using a ridge instead of a pit [Fig. 5.1(a)]. The ridge has wide W and, for practical purposes, is infinitely long in the "y" direction, so that we can neglect diffraction effects along this direction. In this way, the reflected beam acquires a phase of the form

$$\Phi_h(x) = \begin{cases} \exp\left[i4\pi \mathrm{h}/\lambda\right] & 0 \leq x \leq \mathrm{W} \\ 0 & 0 > x > \mathrm{W}, \end{cases} \tag{5.2}$$

so that the reflected beam has now the form

$$U_h(x,y) = \begin{cases} \sqrt{2/(\pi W_0)} \exp\left[-\rho^2/W_0^2\right] \exp\left[i4\pi \mathrm{h}/\lambda\right] & 0 \leq x \leq \mathrm{W} \\ \\ \sqrt{2/(\pi W_0)} \exp\left[-\rho^2/W_0^2\right] & 0 > x > \mathrm{W}. \end{cases} \tag{5.3}$$

Notice that when h= $\lambda/4$ we obtain $\Phi(x) = \pi$, this is, the phase of the field reflected from the ridge is π out of phase relative to the field reflected from the land. The far field interference pattern of this two fields is shown in figure Fig. 5.1(b). Notice that both fields interfere destructively at $\theta = 0$.

By plotting the far-field intensity along the beam optical axis as function of the ridge height h, we can see it follows a sinusoidal interferometric response [Fig. 5.2(a)]. This plot reveals that the

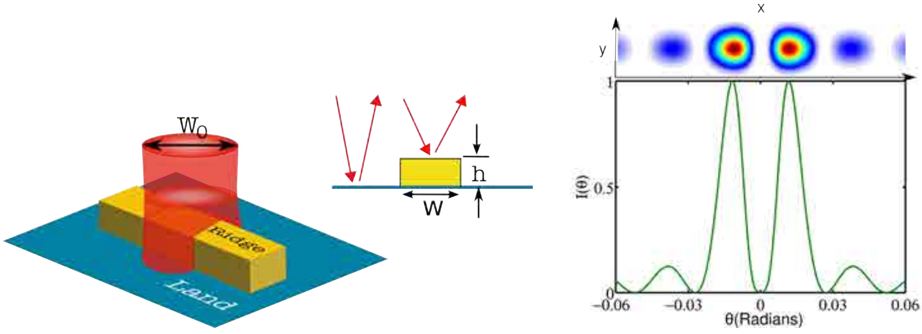

(a) (b)

Figure 5.1: (a) By carefully selecting the focusing lens, a Gaussian beam can be made to straddle a ridge with half of the intensity impinging on the ridge and half on the land. (b) Far field interference pattern for the case h= $\lambda/4$.

case h= $\lambda/4$ used in the compact disk, is almost insensitive to small phase changes, this is, small variations in the height, produce very little changes in the far file intensity. This is one of the reasons for the success of the compact disk technology. The case h=0 (no ridge) is also insensitive to small phase changes. The far field intensity as function of the angle of diffraction θ is plotted for three cases: h=0, h= $\lambda/8$ and h= $\lambda/4$ in Fig. 5.2(b). Maximum intensity changes to small phase changes occurs at h=$\lambda/8$ and h= $3\lambda/8$ which is known as the quadrature condition and will be discussed in the next section. This is of interest to us since we want to detect tiny phase changes.

5.1.1 The quadrature condition

The quadrature condition is reached when the land and pit signals are out of phase by $\pi/2$. This can be accomplished by setting the land 1/8 of the wavelength of light higher than the pit. At this condition, the far field intensity changes linearly with small phase changes. Hence, the addition of a thin layer on top of the ridge will produce the largest changes in intensity along the optical axis [Fig. 5.3(a)], the phase of the reflected beam will be slightly modified as

$$\Phi_{h+d}(x) = \begin{cases} 4\pi\,(\mathrm{h}+\mathrm{d})\,/\,\lambda & \text{-W} \le x \le \text{W} \\ 0 & \text{-W} > x > \text{W}. \end{cases} \tag{5.4}$$

Figure 5.3(b) shows the far field intensity for three different values of d: d= 0, d= 10nm and d= 40nm. In order to show that the largest intensity changes occur at the quadrature condition, we can compute the change of intensity ΔI given by

$$\Delta I = \frac{I_0 - I_d}{I_0} \tag{5.5}$$

where I_0 is the intensity without the layer and I_d is the intensity with the layer. This change of intensity can be observed in Fig. 5.4 where we have plotted ΔI for three cases: h=0, h= $\lambda/8$ and h= $\lambda/4$. As expected, ΔI is very large for h= $\lambda/8$ when compared to the other cases.

One successful application of CPI at quadrature condition is the so called spinning-disk interferometry (SDI), specifically in the Biological compact disc (Bio-compact disk) [3, 4, 5, 6, 7, 8]. The construction of a Bio-compact disk is accomplished by evaporating radial lines of gold (similar to a spoke) into a wafer compact disk, a bio-layer of micromolecules is attached on top of ridges for its

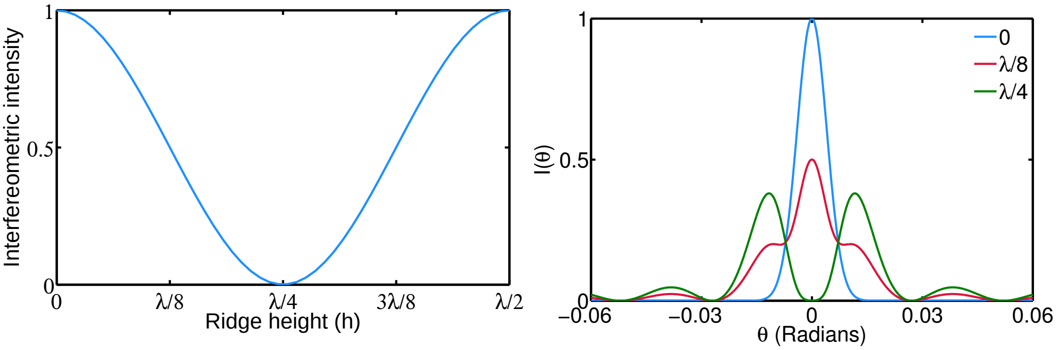

(a) (b)

Figure 5.2: (a) Far field intensity along the optical axis as function of the height h, a sinusoidal response can be observed. (b) Far field intensity for three specific heights: h= 0, h= $\lambda/8$ and h= $\lambda/4$.

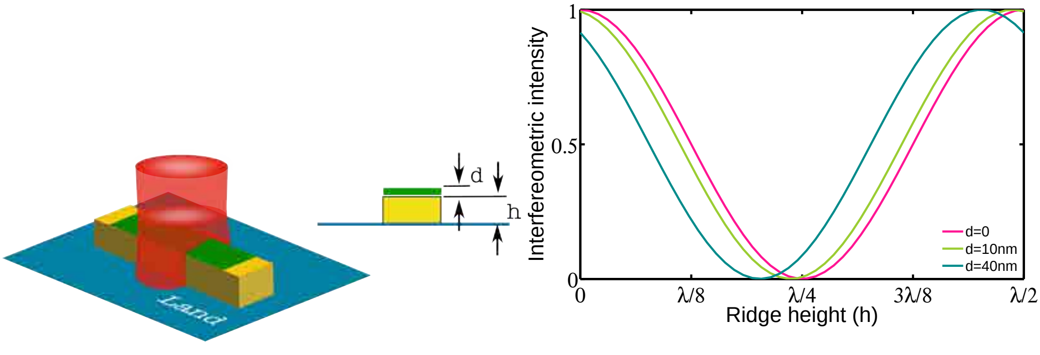

(a) (b)

Figure 5.3: (a) A sample of thickness d placed over a ridge of height h is illuminated with a Gaussian beam of waist W_0 for its analysis. (b) The far field intensity along the optical axis as function of the height h for three different values of d: d= 0, d= 10 and d= 40. As d increases, the sinusoidal intensity shifts to the right.

analysis. Unfortunately, the need to fulfill the quadrature condition may limit the use of SDI since the phase ultimately depends on the wavelength, the thickness, and the index of refraction of the substrate. Moreover, there are situations where the quadrature condition cannot be achieved easily, such as when the required wavelength is either not available or might damage the sample. In the next section, we put forward a novel way to circumvent this limitation based on mode projection.

5.2 Spatial mode projection to measure layer thicknesses

The quadrature condition establishes the ideal conditions under which CPI is hight sensitive to small phase changes. Hence in order to measure the height of tiny layer one would have to first construct a ridge of height h= $\lambda/8$ to place the layer to be measured. Notice the dependence of h on the wavelength, this is, the use of different wavelengths requires the construction of several ridges,

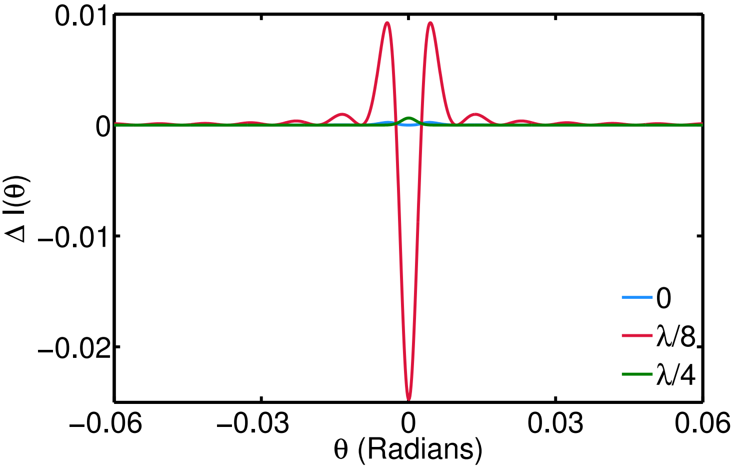

Figure 5.4: Change in intensity due to the addition of a layer of thickness d on top of the ridge. Three cases are shown: h= 0, h= $\lambda/8$ and h= $\lambda/4$. The highest intensity changes happens at h= $\lambda/8$.

one for each wavelength. In order to overcome this drawback, we propose a method in which the quadrature condition is imposed in the signal reflected from the sample. In this way, the sample does not need to be placed on top of a specifically engineered surface, with an specific height. Still we need to place the sample over a reflective surface as shown in Fig. 5.5.

The key point of our approach is to project the reflected light onto appropriately tailored spatial modes (spatial mode projection) before its power is measured. In this way, the quadrature condition is passed on to the mode projection detection system. Such projection can be efficiently made with diverse optical devices, such as computer-generated holograms in spatial light modulators (SLMs) or liquid crystal switchable plates. The selection of the mode to project onto the reflected light depends on the geometry of the sample. For simplicity, but without any loss of generality, in what follows we assume the sample has the from of a cliff (or step), this is, a sharp discontinuity of height d that introduces a phase of the form,

$$\Phi_d(x) = \begin{cases} \exp\left(i4\pi \mathrm{d}/\lambda\right) & x \leq 0 \\ 0 & x > 0 \end{cases} \tag{5.6}$$

so that the reflected beam has the form

$$U_r(x,y) = \begin{cases} \sqrt{2/(\pi W_0)}\exp\left(-\rho^2/W_0^2\right)\exp\left(i4\pi \mathrm{d}/\lambda\right) & x \leq 0 \\ \\ \sqrt{2/(\pi W_0)}\exp\left(-\rho^2/W_0^2\right) & x > 0 \end{cases} \tag{5.7}$$

The power of the projection can be computed as

$$|P|^2 = \int U_r(x,y)U_p^*(x,y)dxdy \tag{5.8}$$

where U_p is the mode we project onto. This can be engineered depending on the form of the sample to be measured. For the present case (a cliff of height d), it has the form,

$$U_p(x,y) = \begin{cases} \sqrt{2/(\pi W_0)}\exp\left(-\rho^2/W_0^2\right)\exp(i\Delta\varphi) & x \leq 0 \\ \\ \sqrt{2/(\pi W_0)}\exp\left(-\rho^2/W_0^2\right) & x > 0 \end{cases} \tag{5.9}$$

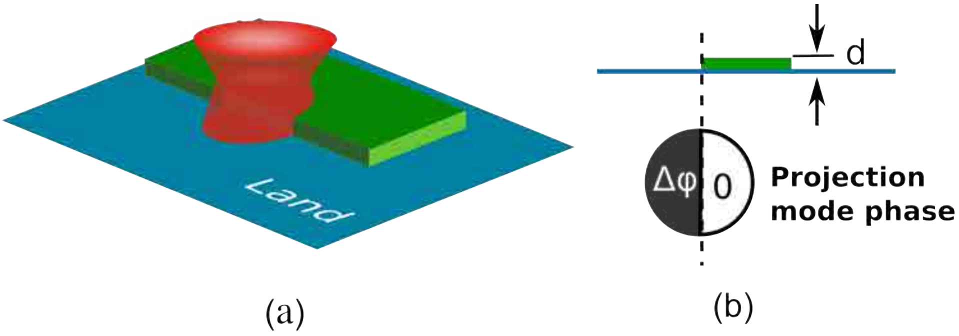

Figure 5.5: (a) The sample is illuminated with a Gaussian beam in such a way half of the intensity is reflected from the sample whereas the other half from the land. (b) The reflected light is then projected onto an appropriately engineered mode where the quadrature condition is imposed via a phase discontinuity tailored according to the form of the sample.The phase discontinuity introduced by the sample must coincide with the phase discontinuity of the projection mode.

After inserting Eqs. (5.7) and (5.9) into Eq. (5.8) we arrive to a normalized form of $|P|^2$ given by

$$|P_{\Delta\varphi|^2} = \frac{1}{2}[1 + \cos(\Delta\varphi - \delta)] \tag{5.10}$$

where $\delta = 4\pi d/\lambda$, the quadrature condition is achieved by setting $\Delta\varphi = \pi/2$. This equation is derived assuming the discontinuity in the projected phase coincides with the position of the cliff of the measured sample, as shown in Fig. 5.5.

5.3 Experimental demonstration

In order to show the feasibility of the mode projection, we carried out an experiment that has been reported in [9]. The experimental setup for the implementation of this technique is shown in Fig. 5.6. A He-Ne laser (λ=632.8 nm, W_0 1.1 mm) is incident on a sample with a step height d. Our samples are etched SiO2 on top of a Si wafer. We image the reflected light with a telescope onto a computer-controlled SLM in which we display the appropriate phase. This is done by using 8-bit gray level values. Each gray level corresponds to a particular value of phase that will be imposed onto the incident beam (reflected from the sample). Half of the beam acquires a phase of $\Delta\varphi$ with respect to its other half. The beam reflected from the SLM is sent to a photodector connected to a digital oscilloscope.

In a first experiment, we obtained the typical sinusoidal response similar to what is observed when the beam impinges directly onto a ridge. This was done by varying the phase $\Delta\varphi$ in the SLM from 0 to 2π and plotting the far field intensity as function of $\Delta\varphi$. This experiment was repeated for three different samples whose height was previously measured with a profilometer (Alpha-Step IQ Surface profilometer). In all cases we compared the experimental data with the theory predicted by Eq. (5.10). Figure 5.7(a) shows the case of a sample whose hight measured with the profilometer is d= 0 . As expected the intensity varies sinusoidally, with a maximum value a $\Delta\varphi = 0$ and a minimum at $\Delta\varphi = \phi$. Figure 5.7(b) shows the case of a sample of height d=8nm (again, when measured with the profilometer), the intensity change has the same shape as in the previous case, however, the

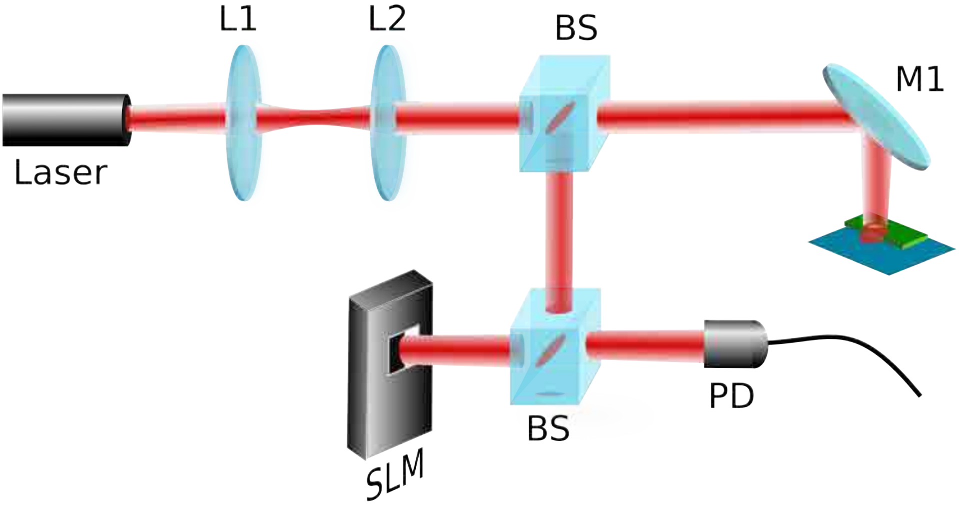

Figure 5.6: The experimental setup. A He-Ne laser beam impinges perpendicularly over the sample. The reflection from the sample is projected onto a SLM where a desired phase is encoded. The resulting beam intensity is measured with a photodectector.

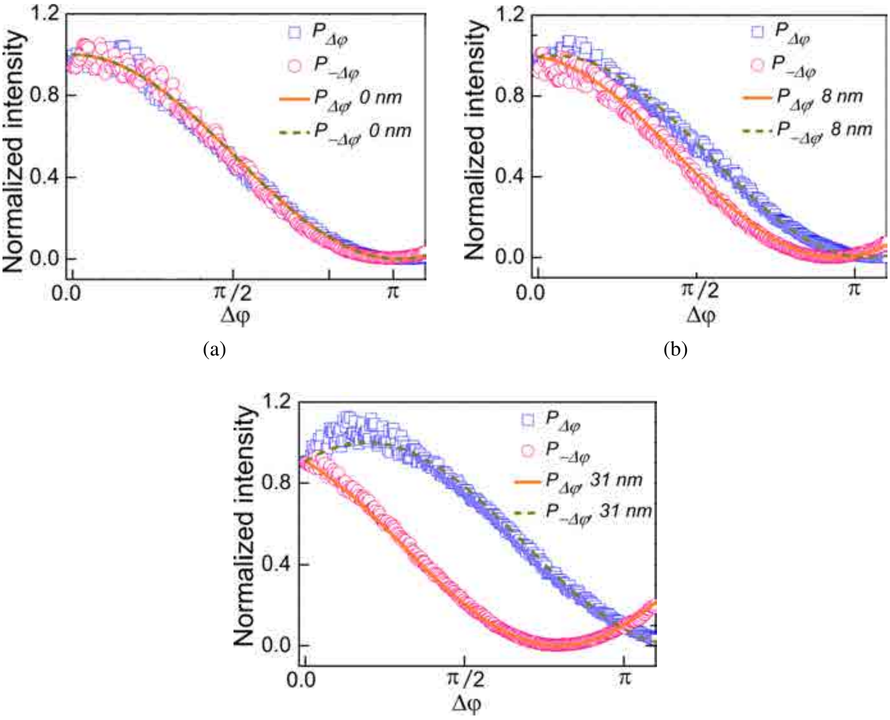

(a) (b)

(c)

Figure 5.7: Normalized intensities for P when projected onto a mode of phases $\Delta\varphi$ and $-\Delta\varphi$ for different heights: (a) sample 1 (1.9 nm measured height, 0 nm profilometry measurement), (b) sample 2 (9.7 nm measured height, 8 nm profilometry measurement), and (c) sample 3 (29.0 nm measured height, 31 nm profilometry measurement). All measurements have standard error of ~0.2 nm.

presence of the layer shifts the minimum either to the right or to the left depending on the sign of $\Delta\varphi$. The last figure [Fig. 5.7(c)] shows the case of a layer of thickness d= 31 nm, in this case the shift is more evident. These plots are very similar to those obtained in the case where the sample is placed over a ridge (see Fig 5.3b for comparison).

In order to quantify the height of the step from our measurements, we take the difference between $P_{\Delta\varphi}$ and $P_{-\Delta\varphi}$, which is given by

$$P_{\Delta\varphi} - P_{-\Delta\varphi} = \sin(\delta)\sin(\Delta\varphi) \tag{5.11}$$

The step height is obtained from $\sin(\delta)$ when ploting $P_{\Delta\varphi} - P_{-\Delta\varphi}$ as a function of $\sin(\Delta\varphi)$. The uncertainty in the measured height comes from the standard error of the slope of the plotted line.

Figure 5.8 is an example of the analysis done to the experimental data. The maximum amplitude happens at quadrature $\Delta\varphi = \pi/2$, as expected [Fig. 5.8(a)]. The measured thickness layers are summarized in Table 1. The uncertainty comes from the fact that the sample is not smooth as observed in the profilometer scans (not shown). Moreover, we ascribe the 1.9 nm off-set in our data to the existence of a nonlinear relationship between the gray level value and the phase introduced by the SLM near π, which we found during initial calibration of the SLM [see, for example, the difference in the line fit with the theoretical line in Fig. 5.8(b) near π].

As in the SDI, the maximum sensitivity in our scheme happens at the quadrature condition. The main difference, however, is the detection scheme. Consider, for example, a step geometry that

Table 5.1: Experimental Thickness Layer (in Nanometers)

Sample	Profilometry[a]	CPI with mode projection	Standar Error
Sample 1	0	1.89	0.23
Sample 2	8	9.72	0.27
Sample 3	31	29.01	0.21

[a] Alpha-Step IQ Surface profilometer. The standard error in the height obtained with the profilometer is in order of nanometers (1-2 nm) owing to the uneven surface of the sample.

fulfills the quadrature condition with a thin layer sample placed on top of the step. The system is illuminated by a Gaussian beam with beam waist W_0 and power P_0. The signal of interest is the normalized differential signal $P_1 - P_2$, where P_1 and P_2 are the power of the detected signal from the step with and without the thin layer. In the SDI, there is an optimum area of detection that gives the maximum value of $P_1 - P_2$. Increasing the area of detection decreases $P_1 - P_2$. In the mode projection scheme on the other hand, the total power of the projected signal is measured and hence, the power does not depend on the detection area. More importantly, given the proper choice of mode the SNR will be higher. In the step geometry considering shot-noise condition, the SNR ratio is enhanced by ≈ 2 dB compared to SDI when using spatial mode projection with $\Delta\varphi = 0$.

The importance of the quadrature condition is the large linear change in the differential signal produced by a tiny layer if the substrate is at quadrature. When the system is not at quadrature, the differential signal is diminished dramatically. This is not an issue in the scheme we present here as spatial modes can be easily engineered such that the linear dependence of the normalized differential signal $P_1 - P_2$ is preserved for any optical height h/λ. We show this for a thin layer on top of a flat substrate (inset Fig. 5.9). In this case, the SDI will not work since the thin layer is on top of a substrate that does not meet the quadrature condition. In our scheme we can reintroduce the quadrature condition on the mode. Figure 5.9 shows the differential signal when the reflected signals are projected onto Gaussian modes with different phase steps. Notice that at $\Delta\varphi = \pi/2$,

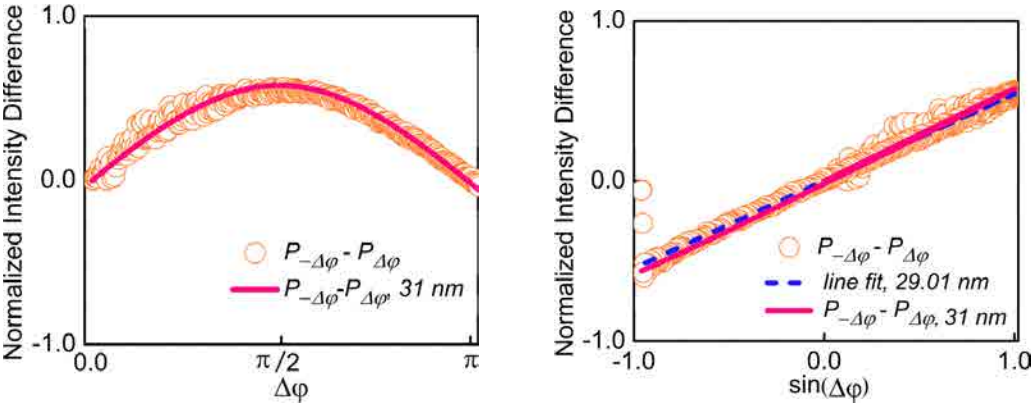

(a) (b)

Figure 5.8: Typical data for analysis. (a) Normalized power difference $P_{\Delta\varphi} - P_{-\Delta\varphi}$ as a function of $\Delta\varphi$. (b) The difference as a function of $\sin(\Delta\varphi)$ is linear as described by Eq. (5.11). Line fit is from the calculated height (dashed line) and from theoretical calculations (solid line). For all plots, the theoretical curve is calculated from a step height of 31 nm, which is independently measured with a profilometer.

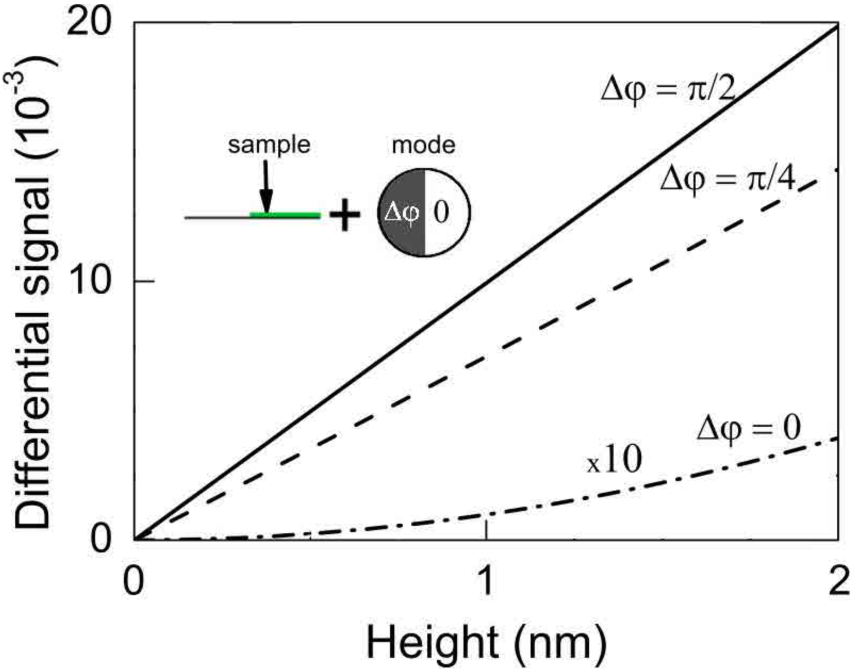

Figure 5.9: Normalized differential signal $(P_1 - P_2)/P_0$ as a function of the sample height when the reflected signal is projected onto a Gaussian mode with phase step $\Delta\varphi$. The solid, dashed, and dashed-dotted (×10) lines correspond to $\Delta\varphi = 0, \pi/2, \pi/4$ respectively.

the differential signal is linear with the height of the layer at the same time giving the maximum differential signal. On the contrary, $\Delta\varphi = \pi/4$ and $\Delta\varphi = 0$ do not give optimal differential signals. This is what we observed in our experiment [Fig. 5.8(a)]. We note, however, that similar to SDI, the lateral resolution of our technique is diffraction limited.

The measurement of subnanometric samples requires the detection of small power differences $P_1 - P_2$. In our scheme, a normalized height $h/\lambda \sim 10^{-4}$ and an initial laser power of 1 mW would give a differential signal of $\delta/2 \sim 600$ nW. In principle this signal can be detected, for example by using the method proposed by Freudiger and co-workers [10, 11] where a high-frequency detection scheme is used to get rid of lower-frequency laser noise, thus allowing the detection of fractional power losses of up to $\sim 10^{-7}$. The SNR is $S/N = \delta/2\sqrt{2\pi E_0\lambda/\hbar c} \sim 14$ dB in our scheme using the parameters above.

In conclusion, we have demonstrated that extremely small step heights can be measured without the need to impose stringent conditions on the substrate by using spatial mode projection in a CPI. We have measured a layer thickness as low as 9.7 nm with a standard error of 170 pm in our experiment. Moreover, we have shown that our scheme enhances the sensitivity of detection and hence can also be used for subnanometric step height measurements.

References

[1] Z. Lu, J. McCaffrey, B. Brar, G. Wilk, R. Wallace, L. Feldman, and S. Tay, “SiO2 film thickness metrology by x-ray photoelectron spectroscopy,” App. Phys. Lett **71**, 2764–2766 (1997).

[2] K. C. Polmann, *The compact Disc Handbook* (Oxford University Press Inc., 1992).

[3] X. Wang, M. Zhao, and D. D. Nolte, “Common-path interferometric detection of protein monolayer on the BioCD,” App. Opt. **46**, 7836 (2007).

[4] M. Zhao, W. Cho, F. Regnier, and D. Nolte, “Differential phase-contrast BioCD biosensor,” App. Opt. **46**, 6196 (2007).

[5] M. M. Varma, H. D. Inerowicz, F. E. Regnier, and D. D. Nolte, “High-speed label-free detection by spinning-disk micro-interferometry,” Biosensors and Bioelectronics **19**, 1371 (2004).

[6] M. M. Varma, D. D. Nolte, H. D. Inerowicz, and F. E. Regnier, “High-Speed Label-Free Multi-Analyte Detection through Microinterferometry,” Proceedings of SPIE **4966**, 58 (2003).

[7] D. D. Nolte, “High-Speed Spinning-Disk Interferometry on the BioCD for Human Diagnostic Applications,” Conf. Proc. IEEE Eng Med Biol Soc. p. 6368 (2009).

[8] D. D. Nolte, “Invited Review Article: Review of centrifugal microfluidic and bio-optical disks,” Rev. Sci. Instrum. **80**, 101101 (2009).

[9] C. R.-G. S. F. P. N. Hermosa and J. P. Torres, “Nanostep height measurement via spatial mode projection,” Opt. Lett. **39**, 299–302 (2014).

[10] C. W. Fraudiger, W. Min, B. Saar, S. Lu, G. R. Holtom, C. He, J. C. Tsai, J. X. Kang, and X. S. Xie, “Label-Free Biomedical Imaging with High Sensitivity by Stimulated Raman Scattering Microscopy,” Science **322**, 1857–1861 (2010).

[11] B. G. Saar, C. W. Freudiger, J. Reichman, C. M. Stanley, G. R. Holtom, and X. S. Xie, “ Select this article Video-Rate Molecular Imaging in Vivo with Stimulated Raman Scattering,” Science **330**, 1368–1370 (2010).

6

Optical Chirality

Contents

6.1 Polarization of light **73**

6.2 Chirality **74**

6.2.1 The role of circular polarization in chirality 74

6.2.2 Superchiral fields and optical chirality 75

6.3 The role of orbital angular momentum in chirality **77**

6.3.1 Derivation of the generalized dissymmetry factor 77

6.3.2 Dissymmetry factor for Bessel beams 79

6.3.3 Enhanced dissymmetry factor with Bessel beams 81

References **84**

This chapter is organized in three sections, the first section is a brief historical introduction about the concept of polarization in optical fields and the role it has played for the understanding of light-matter interactions. The second section is devoted to describe the concept of chirality, focusing our attention in chiral molecules and their interaction with circularly polarized light (CPL). In this section we also introduce the concept of super *chiral fields* and *optical chirality* (which has been used to quantify the chiral response of molecules to CPL). In the last section, we discuss the role that beams endowed with OAM can play for the discrimination of chiral molecules. In our approach we start from exact solutions to the Maxwell's equation.

6.1 Polarization of light

The discovery of polarization in 1670 is usually attributed to Erasmus Bartholinus, although he was not aware of the phenomenon. He observed for the first time, the splitting of a natural incident ray into two of equal intensity after passing through a calcite crystal. Two years later Huygens showed that these two beams consisted of two independent oppositely polarized rays. In 1803, Young showed that light vibrates in the plane perpendicular to the direction of propagation and associated the polarization phenomena to this transverse nature of light. Few years later, after many experiments with glass surfaces, Malus concluded that natural light consisted of two perpendicular polarizations. In 1812 Brewster discovered that when unpolarized light impinges on a glass surface at a certain angle, the reflected light is completely polarized, this angle was named after him as Brewster's angle. During the following years Arago and Biot performed fundamental investigation on rotatory polarization and were able to distinguish between left and right handed polarization. In 1822, Herschel discovered that the rotatory polarization in quartz originated from two different crystallographic structures: a phenomenon called enantiomorphism. A major contribution to polarization study was made by Augustin Jean Fresnel in 1823 by stating the famous formulas for reflection and transmission of a plane wave impinging on an interface between two dielectric isotropic media. He is credited also for recognized optical rotation as a phenomena arising from circular birefringence. Several years later, in 1848, Louis Pasteur discovered that molecular symmetry is responsible for the phenomenon of optical rotation. He was able to isolate two types of crystal from tartaric acid, each one being a mirror image of the other (enantiomorphs) and observed that solutions made out of these two types of crystals will cause the direction of polarization of linearly polarized light to rotate either clockwise or counterclockwise. This phenomenon that is at the basis of chiral asymmetry plays a fundamental role in the chemistry of life. Soon after, in 1852 Stokes would set the basis for the modern description of polarization. He introduced four measurable quantities to describe mathematically any state of polarization, known as Stokes parameters. The first parameter represents the total intensity of the field and the three others describe the state of polarization. In 1892 Poincaré published a novel mathematical approach to the understanding of light's polarization. He, more that any other, saw the physical implications of geometry in polarization and provided an intuitively geometric way of representing any polarization state. By using a stereographic projection each point on the plane is mapped into a sphere (Poincaré sphere) whose points are in one-to-one correspondence with all the possible states of polarization. The upper and lower poles represent left and right circularly polarized light and points on the equator corresponds to linear polarization. Diametrically opposite points on the equator correspond to horizontal and vertically polarized light. The rest of the points represents elliptic polarization. By the end of the nineteen century, the ideas about polarized electromagnetic fields was well understood and supported by Maxwell Electromagnetic theory. In the next section, we discus the role of circular polarization when light interacts with matter. In particular for the discrimination of chiral molecules.

6.2 Chirality

The world *chirality* meaning handed was introduced in 1904 by Lord Kelvin. His definition of chirality reads "I call any geometrical figure or group of points 'chiral', and say it has 'chirality', if its image in a plane mirror, ideally realized, cannot be brought into coincidence with itself" [1]. According to this definition, an object is chiral if it cannot be superimposed with its own mirror image (Fig.6.1). A pair of molecules that exhibit this property are termed enantiomers and they are identical in most regards, it is only in their interaction with other chiral objects that they become distinguishable [2].

6.2.1 The role of circular polarization in chirality

Chirality plays a crucial role in life, since most of the important molecular building blocks of life, aminoacids and sugars, come in left- or right-handed varieties. One of the most striking features of life is why most of these molecules present a specific chirality at all, since many chemical processes performed in the lab to obtain these substances give no preference for any specific form of chirality [3]. It is relevant the fact that human bodies make amino acids and sugars using only the left-handed enantiomers, the right-handed being ignored by our cells. This specificity is of great interest in the drug industry, since for instance two enantiomers can have very different physiological effects [4]. Historically, CPL has been always associated to molecular chirality since it has played a crucial role in the study of optical chiral effects. One example is optical rotation, a phenomenon in which the plane of polarization of a linearly polarized beam rotates after propagation in a chiral medium.

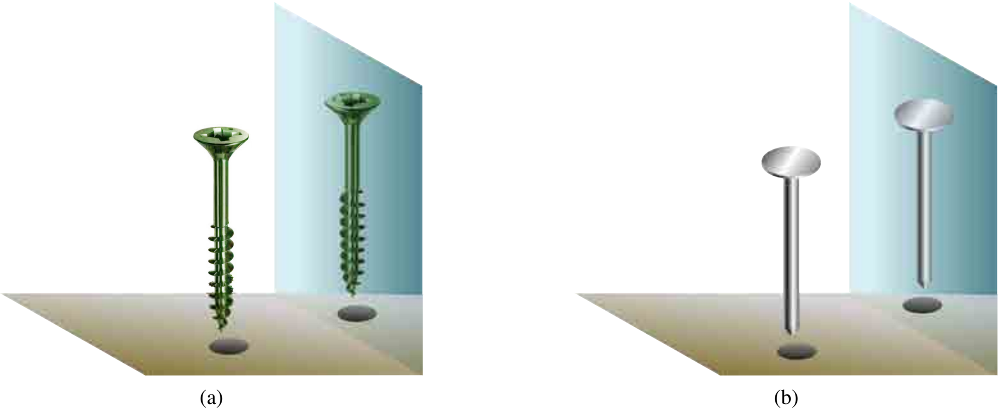
(a) (b)

Figure 6.1: (a) The mirror image of a chiral object can not be brought into coincidence with itself. (b) A non-chiral object and its mirror image are exactly the same.

Optical rotation can be described in terms of different refractive indices for the two types of CPL. Another example is circular dichroism (CD), the different absorption rate of left- and right-circularly polarized light by chiral molecules (Fig. 6.2). CD is quantified by the Dissymmetry Factor g, defined as

$$g \equiv \frac{2\left[A^{(+)} - A^{(-)}\right]}{A^{(+)} + A^{(-)}}, \tag{6.1}$$

where $A^{(\pm)}$ is the absorption rate in left or right CPL. Explicitly, the dissymmetry factor has the form

$$g_{CPL} = -\frac{4G''}{c\alpha''}, \tag{6.2}$$

where G'' (electric-magnetic polarizability) and α'' (electric polarizability) are associated only to intrinsic chemical properties of the molecules. Explicit definitions of G'' and α'' are given in Section 6.3.1

Although the basis of circular dichroism and optical rotation have been settled, its study is still challenging since most molecules are small compared to the wavelength of light. Therefore, the different rates of absorption of a chiral medium when illuminated by the two forms of CPL are generally small, making its detection rather demanding in some cases. Several efforts along this direction have been made in order to enhance the chirooptical response of molecules, for example, by inserting an achiral molecule in a chiral system [5] or by using planar chiral nanostructures [6, 7]. There has been also contributions from nonlinear spectroscopy [8, 9] and coherent control [10, 11].

6.2.2 Superchiral fields and optical chirality

The form of Eq. (6.2) suggest that the different response of chiral materials to CPL depended only on intrinsic properties of the chiral medium. However, very recently a new quantity termed “Optical Chirality” and denoted as C has changed this perspective. Optical chirality was introduced originally in 1964 by Lipkin [12] and rediscovered recently by Yiqiao *et. al* [13]. This quantity does not depend on the properties of matter but rather is an intrinsic property of chiral fields. It captures the degree to which the electric and magnetic fields $\mathbb{E}(\mathbf{r}, t)$ and $\mathbb{B}(\mathbf{r}, t)$ wrap around a helical axis at each point in space. In general, the amount of chiral response generated by an arbitrarily-shaped optical field can

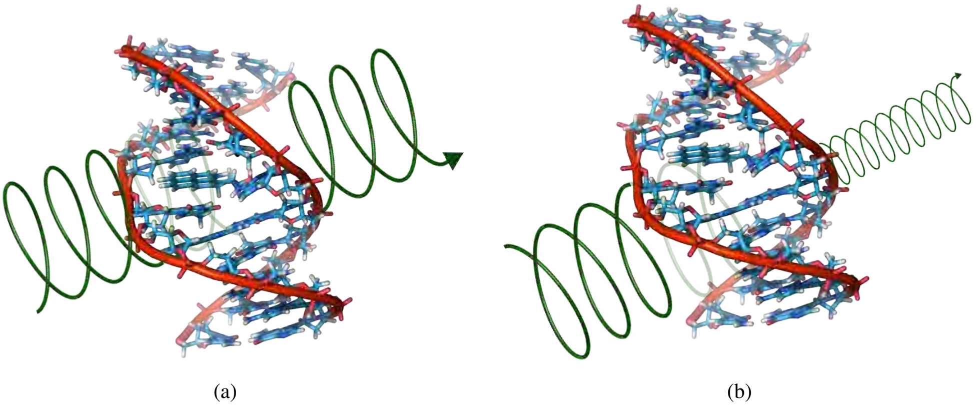
(a) (b)

Figure 6.2: Representation of the interaction of (a) right- and (b) left-CPL with chiral molecules. The absorption in the amount of CPL by chiral molecules depends on the direction of rotation of CPL, in (b) the absorption is considerably higher compared to (b).

be computed as [13, 14, 15]

$$C \equiv \frac{\epsilon_0}{2}\mathbb{E}(\mathbf{r},t)\cdot\nabla\times\mathbb{E}(\mathbf{r},t) + \frac{1}{2\mu_0}\mathbb{B}(\mathbf{r},t)\cdot\nabla\times\mathbb{B}(\mathbf{r},t), \tag{6.3}$$

where ϵ_0 and μ_0 are the permittivity and permeability of free space respectively. Crucially, the inspection of this quantity shows that it should be possible to generate *superchiral fields*: electromagnetic fields that when interact with chiral molecules produce an enhancement of the amount of circular dichroism detected [13, 16]. This opens a whole new scenario for the detection of optical chirality, where now the shape of the optical field plays a crucial role to enhance the chiral response. A mathematical formulation to include the effects produced by the shape of the optical field was given by Yiquio and co-workers in the form of a generalized dissymmetry factor, which has the form,

$$g = g_{CPL}\left(\frac{cC}{2\omega U_e}\right), \tag{6.4}$$

with c the speed of light, ω its frequency, C the optical chirality and U_e the local electric energy density. This new generalized dissymmetry factor combines both the effect of the molecule (g_{CPL}) and the effects produced by the electromagnetic field ($cC/2\omega U_e$). For the special case of a chiral molecule subjected to a circularly polarized monochromatic electromagnetic field the optical chirality reduces to $C = \pm 2U_e/c$ (positive chirality corresponding to left CPL) and the dissymmetry factor reduces to

$$g = -\frac{4G''}{c\alpha''} = g_{CPL}. \tag{6.5}$$

Thus, for a given molecule even though g_{CPL} is fixed, the dissymmetry factor, g, can be manipulated by appropriately tailoring the electromagnetic field. One way to produce this type of electromagnetic fields comprises the use of a "superchiral" standing wave, which is constructed from two counterpropagating CPL plane waves of opposite handedness and slightly different amplitudes. Experimentally this can be achieved by using CPL impinging on a partially reflective mirror at normal incidence. Part of this light is reflected back from the mirror with the opposite polarization and interferes with the incoming light giving as result a super chiral fields. If a chiral molecule is placed at a node in a superchiral wave, the dissymmetry actor will be

$$g = g_{CPL}\frac{1+\sqrt{R}}{1-\sqrt{R}}, \tag{6.6}$$

where R is the reflectivity of the mirror with values in the range $0 < R < 1$. Superchiral field have been also generated in the near field by the optical excitation of plasmonic planar chiral metamaterials [16]

6.3 The role of orbital angular momentum in chirality

In section 2.3.2 we showed that helical beams, *i.e.* beams with a phase of the form $\exp i\ell\phi$, carry an amount $\ell\hbar$ of orbital angular momentum per photon, being ℓ an integer number. Helical beams are also chiral objects in the sense that the phase of two beams with opposite ℓ values, rotate in the opposite direction, in a similar way to CPL (see Fig. 6.3). Therefore, it seems naturally to ask if whether or not, chiral molecules will show any response when interrogated by helical beams endowed with OAM.

Previous theoretical investigations on the interaction of beams with OAM and molecules have yielded seemingly contradictory results. Within the electronic dipole approximation for diatomic molecules and in the paraxial approximation, it was argued that the internal "electronic-type" motion does not participate in any OAM exchange [17]. Also, under the paraxial approximation, it was established that OAM cannot be engaged with the chirality of a molecular system [19]. Later on, the inclusion of electronic, rotational, vibrational and center-of-mass motion variables, seemed to demonstrate that the OAM can couple to the rotational and electronic motion [18]. In turn, careful experiments aimed at detecting a chiral response of molecules making use of optical beams with OAM have not succeeded [20, 21], apparently supporting the theoretical predictions made in [17] and [19]. We will show now that in considering exact solutions to the Maxwell equation's endowed with OAM, more precisely, Bessel light beams [22], it is possible to unveil some important features not easily shown in the paraxial framework.

6.3.1 Derivation of the generalized dissymmetry factor

Our goal is to find if chiral molecules can be distinguished upon illumination with helical beams of opposite winding numbers. For this, we need to compute the dissymmetry factor g_e and compute the

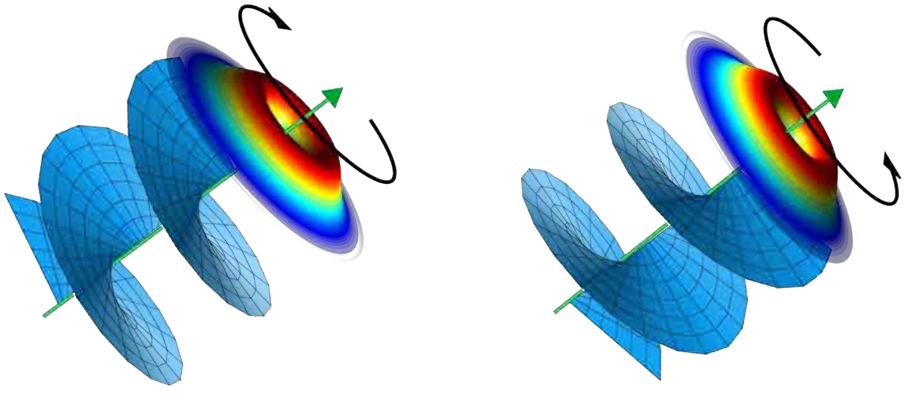

(a) (b)

Figure 6.3: The helicoidal phase of two beams with opposite winding numbers (a) $\ell = -1$ and (b) $\ell = +1$ rotates in opposite direction, in a similar way to CPL.

absorption rate $A^{(\pm\ell)}$, related to direction of rotation of the helical phase front given by the sign of ℓ (Fig. 6.4). This is, we need to compute

$$g_\ell = \frac{2\left[A^{(+\ell)} - A^{(-\ell)}\right]}{A^{(+\ell)} + A^{(-\ell)}}, \tag{6.7}$$

Two ingredients are essential in our investigation. The first is to consider a form of light-matter interaction that couples the electric and magnetic fields of the optical beam to the electric and magnetic dipole moments of a chiral molecule, $\tilde{\mathbf{p}}$ and $\tilde{\mathbf{m}}$ respectively, [2, 23], this is,

$$\tilde{\mathbf{p}} = \tilde{\mu}_E\tilde{\mathbb{E}} + i\tilde{G}\tilde{\mathbb{B}} \tag{6.8}$$

$$\tilde{\mathbf{m}} = \tilde{\mu}_B\tilde{\mathbb{B}} - i\tilde{G}\tilde{\mathbb{E}}, \tag{6.9}$$

where $\tilde{\mu}_E = \alpha' + i\alpha''$, $\tilde{\mu}_B = \beta' + i\beta''$ are the electric and magnetic polarizabilities respectively and $\tilde{G} = G' + iG''$ is the isotropic mixed electric-magnetic dipole polarizabilities. Even though higher order multipoles can also contribute for light beams with general spatial shapes [24], we assume here that these contributions are sufficiently small so they can be safely neglected. The second ingredient is the use of solutions that departs from the paraxial approximation, more precisely, Bessel beams.

We proceed now with the derivation of g_ℓ, which appeared in [24] and will be repeated here for the sake of clarity. Since we intent to relate it to the winding number ℓ we have labeled it asg_ℓ. The rate of excitation of a molecule in the presence of a monochromatic EM field averaged in time is given by

$$A^{(\pm)} = \langle \mathbb{E} \cdot \frac{\partial \mathbf{p}}{\partial t} + \mathbb{B} \cdot \frac{\partial \mathbf{m}}{\partial t} \rangle = \frac{\omega}{2}\mathrm{Im}(\tilde{\mathbb{E}}^* \cdot \tilde{\mathbf{p}} + \tilde{\mathbb{B}}^* \cdot \tilde{\mathbf{m}}). \tag{6.10}$$

Insertion of Eqs. (6.8) and (6.9) into Eq. (6.10) yields

$$A^{(\pm)} = \frac{\omega}{2}(\alpha''\tilde{\mathbb{E}}\tilde{\mathbb{E}}^* + \beta''\tilde{\mathbb{B}}\tilde{\mathbb{B}}^*) \pm G''\omega\mathrm{Im}(\mathbb{E}^* \cdot \mathbb{B}). \tag{6.11}$$

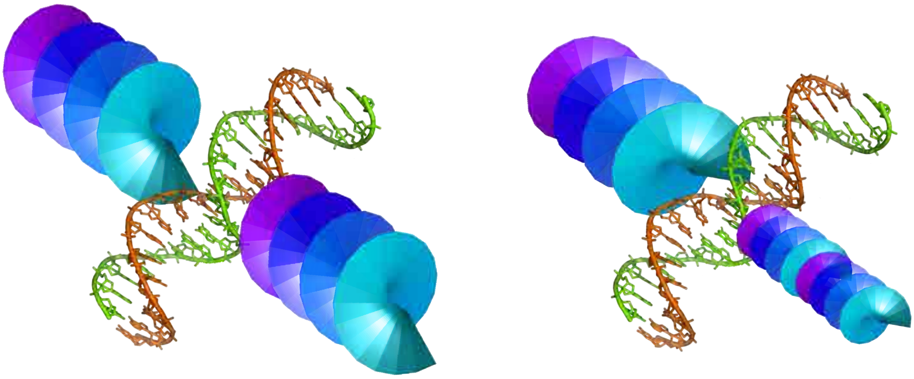

(a) (b)

Figure 6.4: Illustration of the expected response from chiral molecules upon interaction with an OAM beam with winding number (a) $\ell = 1$ and (b) $\ell = +1$. In (a) the transmitted intensity of the helical beam remains the same whereas in (b) part of it is absorbed by the molecule resulting in a decreasing of the transmitted intensity.

The term involving β'' can be dropped since for most molecules it is negligibly small. Therefore,

$$A^{(\pm)} = \frac{\omega}{2}\alpha''\tilde{\mathbb{E}}\tilde{\mathbb{E}}^* \pm G''\omega\mathrm{Im}(\tilde{\mathbb{E}}^* \cdot \tilde{\mathbb{B}}). \tag{6.12}$$

After substituting Eq. (6.12) into Eq. (6.7) we arrive to an expression for the dissymmetry factor that combines the properties of the molecule and the properties of the electromagnetic field, this is,

$$g_\ell = 2\frac{G''\mathrm{Im}(\tilde{\mathbb{E}}^* \cdot \tilde{\mathbb{B}})}{\alpha''\tilde{\mathbb{E}}^*\tilde{\mathbb{E}}}. \tag{6.13}$$

Up to now, we haven't assume any specific form of the electromagnetic field, *i.e.*, this relation holds independently of the state of polarization. By using Faraday's law and Ampere's in free space (Eqs. 2.3b and 2.3d) and the identity

$$\omega\mathrm{Im}(\tilde{\mathbb{E}}^* \cdot \tilde{\mathbb{B}}) = \mathbb{E} \cdot \frac{\partial \mathbb{B}}{\partial t} - \mathbb{B} \cdot \frac{\partial \mathbb{E}}{\partial t}, \tag{6.14}$$

where it has been assumed that $\mathbb{E}(\mathbf{r}, t) = \mathbf{E}(\mathbf{r})\exp(-i\omega t)$ and $\mathbb{B}(\mathbf{r}, t) = \mathbf{B}(\mathbf{r})\exp(-i\omega t)$, expression 6.13 can be written in terms of the optical chirality as

$$\mathrm{Im}(\tilde{\mathbb{E}}^* \cdot \tilde{\mathbb{B}}) = -\frac{1}{\omega}\mathbb{E} \cdot \nabla \times \mathbb{E} - \frac{1}{\omega\epsilon_0\mu_0}\mathbb{B} \cdot \nabla \times \mathbb{B} = -\frac{2C}{\epsilon_0\omega}, \tag{6.15}$$

Incidentally, equation (6.15) provides with a simpler formula to compute the optical chirality given by

$$C = -\frac{\epsilon_0\omega}{2}\mathrm{Im}(\tilde{\mathbb{E}}^* \cdot \tilde{\mathbb{B}}). \tag{6.16}$$

The term in the denominator is related to the time-averaged electric energy density as

$$U_e = \frac{\epsilon_0}{4}\tilde{\mathbb{E}}^*\tilde{\mathbb{E}}. \tag{6.17}$$

By substituting Eqs. (6.15) and (6.17) into Eq. (6.13) we arrive to

$$g_\ell = \frac{2G''}{\alpha''}\frac{C}{\omega U_e} = g_{CPL}\frac{cC}{2\omega U_e}, \tag{6.18}$$

which is equation 6.4.

6.3.2 Dissymmetry factor for Bessel beams

In this section we will compute the dissymmetry factor explicitly. We use the most general form the electric field of a Bessel beam, which propagates along the z direction [22],

$$\mathbb{E}(\mathbf{r}, t) = E_0\left\{\hat{\mathbf{n}}\psi_l + i\frac{k_t}{2k_z}[(\alpha + i\beta)\psi_{l-1} - (\alpha - i\beta)\psi_{l+1}]\hat{\mathbf{z}}\right\} \tag{6.19}$$

where $\psi_\ell = J_\ell(k_t\rho)\exp[i(\ell\phi + ik_z z - \omega t)]$. J_ℓ is the ℓth-order Bessel function, $\hat{\mathbf{n}} = \alpha\hat{\mathbf{x}} + \beta\hat{\mathbf{y}}$ is again a unitary complex vector that indicates the polarization state in the transversal plane, (ρ, ϕ) are the radial and azimuthal variables in cylindrical coordinates, ℓ is the winding number related to the OAM of the Bessel beams and k_t and k_z are the transversal and longitudinal components of the wave vector respectively, satisfying $k^2 = k_t^2 + k_z^2$. The magnetic field $\mathbb{B}$ can be computed using the relation $\mathbb{B} = -i\omega\nabla \times \mathbb{E}$, this is, Ampere's law. After some algebra we arrive to

$$\mathbb{B} = \frac{E_0 k_z}{\omega}\left\{ \hat{\mathbf{z}} \times \hat{\mathbf{n}}\psi_l - \frac{k_t}{2k_z}\left[(\alpha + i\beta)\psi_{l-1} + (\alpha - i\beta)\psi_{l+1}\right]\hat{\mathbf{z}} \right.$$
$$\left. + i\left(\frac{k_t}{2k_z}\right)^2 \left[(\alpha + i\beta)(\hat{\mathbf{x}} + i\hat{\mathbf{y}})\psi_{l-2} - (\alpha - i\beta)(\hat{\mathbf{x}} - i\hat{\mathbf{y}})\psi_{l+2} - 2i\,\hat{\mathbf{z}} \times \hat{\mathbf{n}}\psi_l\right] \right\}. \quad (6.20)$$

In order to discard the effects produced by polarized beams, we will consider only linear polarization, restricting to the case $\alpha = 1$ and $\beta = 0$. With these simplifications, the electric and magnetic fields [Eqs. (6.19) and (6.20) respectively] reduces to

$$\mathbb{E}(\mathbf{r}, t) = E_0 \left\{ \hat{\mathbf{x}}\psi_l + i\frac{a}{2}[\psi_{l-1} - \psi_{l+1}]\hat{\mathbf{z}} \right\} \quad (6.21)$$

and

$$\mathbb{B} = \frac{E_0 k_z}{\omega}\left\{ \left[i\frac{a^2}{2}[\psi_{l-2} - \psi_{l+2}) \right]\hat{\mathbf{x}} + \left[\psi_l - \frac{a^2}{4}(\psi_{l-2} + \psi_{l+2} - 2\psi_l) \right]\hat{\mathbf{y}} - \left[\frac{a^2}{4}(\psi_{l-1} + \psi_{l+1}) \right]\hat{\mathbf{z}} \right\} \quad (6.22)$$

here $a = k_t/k_z$. Upon substitution of the above equations into the optical chirality (Eq. 6.16) we obtain

$$C_B^+ = \frac{\epsilon_0 E_0^2 \ell J_\ell}{2k_z\rho^4}[x^2 k_t\rho(J_{\ell+1} - J_{\ell-1}) + (x^2 - y^2)J_\ell] \qquad \text{for} \qquad \ell > 0 \quad (6.23)$$

and

$$C_B^- = -\frac{\epsilon_0 E_0^2 \ell J_\ell}{2k_z\rho^4}[x^2 k_t\rho(J_{\ell+1} - J_{\ell-1}) + (x^2 - y^2)J_\ell] \qquad \text{for}\ell \qquad < 0 \quad (6.24)$$

Notice that $C_B^+ = C_B^-$.

The time-average electric energy density U_e can be computed by inserting Eq. (6.21) into Eq. (6.17) giving as result,

$$U_e = \frac{\epsilon_0 E_0^2}{4\rho^2 k_z^2}\left\{ J_\ell^2[k_z^2\rho^2 + \ell^2] - k_t^2 x^2 J_{\ell-1}J_{\ell+1} \right\}. \quad (6.25)$$

Hence, a general expression for the relative to CPL dissymmetry factor of a Bessel beam takes the form

$$G_\ell = \frac{g_\ell}{g_{CPL}} = \pm\frac{k_z \ell J_\ell}{k\rho^2}\left[\frac{x^2 k_t\rho(J_{\ell+1} - J_{\ell-1}) + (x^2 - y^2)J_\ell}{J_\ell^2[k_z^2\rho^2 + \ell^2] - k_t^2 x^2 J_{\ell+1}J_{\ell-1}} \right]. \quad (6.26)$$

The optical chirality does not generally vanish at the center of the beam ($\rho = 0$) for $\ell = \pm 1$ which is no true for different values of ℓ. This restricts our analysis to the case $\ell = \pm 1$. Equation (6.26) after substitution of $\ell = 1$ becomes

$$G_{\ell=1} = \frac{k_z J_1}{k\rho^2}\left[\frac{x^2 k_t\rho(J_2 - J_0) + (x^2 - y^2)J_1}{J_1^2[k_z^2\rho^2 + 1] - k_t^2 x^2 J_2 J_0} \right]. \quad (6.27)$$

Figure 6.5 shows a plot of $g_{\ell=1}/g_{CPL}$ as function ρ, for a value of $k_t/k_z = 0.1$. As we can see, at the centre of the beam $g_{\ell=1} \neq$ where it reaches its maximum value. Even though these are vortex beams possessing OAM, the total electric and magnetic fields at the center do not vanish, only the transverse components does whereas the longitudinal components survive.

The maximum value of $G_{\ell=1}$ can be obtained by explicit substitution of J_0, J_1 and J_2. These can be obtained from a Taylor series expansion around $x = 0$ that has the general form

$$J_n(x) = \sum_{s=0}^{\infty} \frac{(-1)^s}{s!(n+s)!} \left(\frac{x}{2}\right)^{n+2s} = \frac{x^n}{2^n n!} - \frac{x^{n+2}}{2^{n+2}(n+1)!}. \tag{6.28}$$

In fact, the first term of the series alone will suffice for an approximation within the 1% of accuracy [25]. Hence,

$$J_0(k_t\rho) = 1, \qquad J_1(k_t\rho) = \frac{k_t\rho}{2} \qquad \text{and} \qquad J_2(k_t\rho) = \frac{k_t^2\rho^2}{8} \tag{6.29}$$

After explicit substitution of Eq. (6.29), into Eq. (6.27) we arrive to

$$G_{\ell=1} = \frac{k_z}{2k}\left[\frac{x^2k_t^2 - 4}{k_z^2\rho^2 - x^2k_t^2 + 2}\right], \tag{6.30}$$

so in the limit when $\rho \to 0$

$$G_{\ell=1} = -\frac{k_z}{k}. \tag{6.31}$$

Therefore, in principle chiral molecules are sensitive to Bessel beams endowed with OAM when $\ell = 1$. In the next section we will discuss the conditions to achieve an enhancement of the dissymmetry factor, based on the results of this section.

6.3.3 Enhanced dissymmetry factor with Bessel beams

An enhancement of the chiral response of molecules illuminated with Bessel beams endowed with OAM is possible via a coherent superposition of two OAM optical beams with indices $\ell = +1$ and $\ell = -1$. Both beams exhibit equal linear polarizations given by $\cos(\phi)\hat{\mathbf{x}} + \sin(\phi)\hat{\mathbf{y}}$ [26]. Following the result of the previous section, we will restrict to the case $\ell = \pm 1$ and analyze the dissymmetry factor at the center of the beam, this is, $\rho \sim 0$. With this consideration, the electric and magnetic fields at the center write

$$\begin{aligned} \mathbf{E}(0) &= i\frac{E_0k_t}{2k_z}\left[A\exp(i\phi) - B\exp(-i\phi)\right]\hat{\mathbf{z}}, \\ \mathbf{B}(0) &= -\frac{E_0k_t}{2\omega}\left[A\exp(i\phi) + B\exp(-i\phi)\right]\hat{\mathbf{z}}, \end{aligned} \tag{6.32}$$

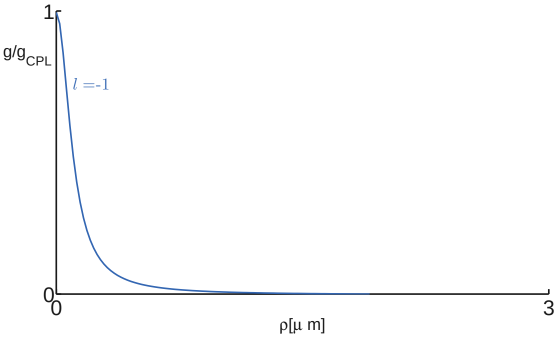

Figure 6.5: Dissymmetry factor.

where A and B are complex amplitudes. Inserting the expressions of $\mathbf{E}(0)$ and $\mathbf{B}(0)$ into Eqs. (6.15) and (6.17), the energy density U_e and the optical chirality C read

$$U_e = \frac{\epsilon_0 k_t^2 |E_0|^2}{16 k_z^2}\left[|A|^2 + |B|^2 - 2|A||B|\cos(2\phi - \xi)\right], \tag{6.33}$$

$$C = -\frac{\epsilon_0 k_t^2 |E_0|^2}{8 k_z}\left(|A|^2 - |B|^2\right), \tag{6.34}$$

where $\xi = \arg(B/A)$ is the phase difference between A and B. The structure of the electric and magnetic fields which bear optical chirality is radically different from the usual form of CPL. The fields at the center of the beam contain a single component of the field (along the direction of propagation $\hat{z}$), while in the case of CPL there are two orthogonal components, $\hat{x}$ and $\hat{y}$, perpendicular to the direction of propagation. For instance, for $\phi = 0$ and A and B real numbers, Eq. (6.32) shows that there is a $\pi/2$ phase difference between the electric and magnetic fields, which is responsible for the non-zero value of the chirality. This $\pi/2$ phase difference is also typical of CPL.

For a molecule located at the center of the superposition of these two Bessel beam, the dissymmetry factor takes now the form,

$$\frac{g}{g_{CPL}} = -\frac{k_z}{k}\frac{|A|^2 - |B|^2}{|A|^2 + |B|^2 - 2|A||B|\cos(2\phi - \xi)}. \tag{6.35}$$

Eq. (6.35) shows that when $|A| = 0$ or $|B| = 0$ (only one beam is present), the dissymmetry factor for paraxial beams ($k_z \sim k$) is nearly that of circularly polarized light, i.e. $|g/g_{CPL}| \sim 1$, which is Eq. (6.31). Moreover, by choosing appropriate values of A and B, so that the electric energy density at the center of the beam is close to zero, one can enhance the dissymmetry factor, i.e. $|g/g_{CPL}| \gg 1$ (see Fig. 6.6), the key towards observing an enhanced chiral response [24].

Fig. 6.7 shows the relative dissymmetry factor as a function of the polarization angle ($\phi = 0$ corresponds to polarization along $\hat{x}$, while $\phi = 90^o$ along $\hat{y}$), for some selected values of the angle ξ and the ratio $r = |B|/|A|$. For $r = 0.95$, one obtains $g/g_{CPL} < 0$, while for $r = 1.05$, one has $g/g_{CPL} > 0$. Eq. (6.35) shows that an enhanced chiral response requires $|A| \sim |B|$, and $\phi = \xi/2$, so that the relative dissymmetry factor reach the maximum value of

$$\frac{g}{g_{CPL}} = \frac{k_z}{k}\frac{|A| + |B|}{|B| - |A|}. \tag{6.36}$$

The case $|A| = |B|$ would generate a null of the total electric field at the center.

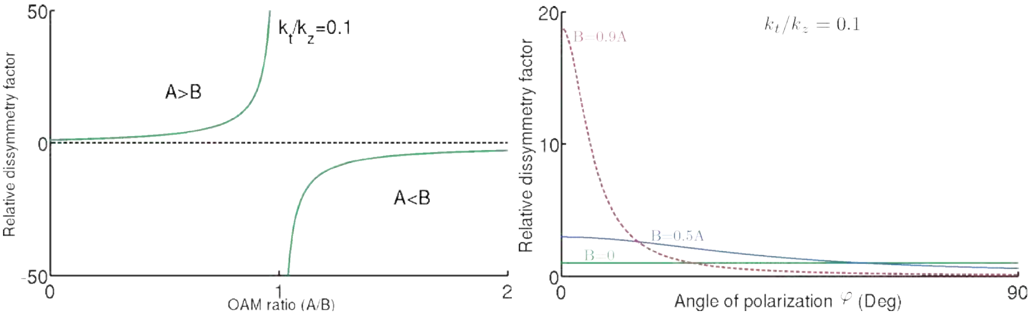

(a) (b)

Figure 6.6: Relative dissymmetry factor as function of the amplitude of the superimposed beams (A and B), for the case $k_t/k_z = 0.1$.

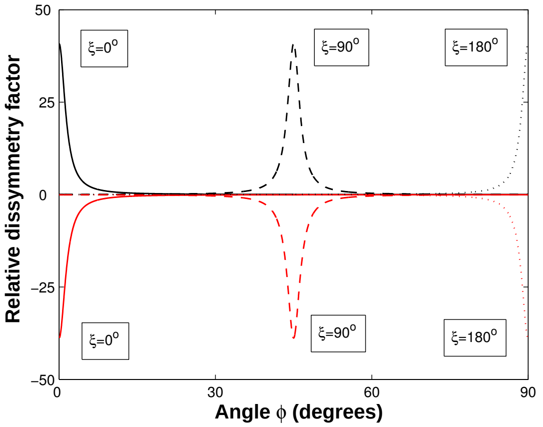

Figure 6.7: Relative dissymmetry factor as a function of the polarization angle ϕ for two values of the ratio $r = |B|/|A|$: $r = 0.95$ (red lines) and $r = 1.05$ (black lines), and three values of the angle ξ: 0^o (solid), 90^o (dashed) and 180^o (dotted). In all cases $k_t/k_z = 0.1$.

Two important conclusions can be drawn from Eq. (6.35). Firstly, we can detect, in principle, the circular dichroism induced by a chiral molecule located at the center of a Bessel beam with winding numbers $\ell = \pm 1$. This is somehow unexpected, since the optical field at the center of the beam contains a single component of the electric and magnetic fields and the transverse fields vanish. Second, the circular dichroism can even be largely enhanced when compared with the case of circularly-polarized light, similarly to the effects observed in [24] with counter-propagating circularly polarized beams. However, the superposition proposed here involves two co-propagating fields, whose centers coincide along the propagation axis, avoiding the experimental problem of locating the sample at one node of an standing wave [24].

The circular dichroism considered here could be experimentally observed by using as probe a single molecule with a fixed absorption dipole moment parallel to the beam axis [27] or a chiral solid microsphere[28] located at the center of the beam. The fluorescence of the single molecule can probe the local field intensity before and after the interaction of the light beam with the chiral medium. The probe particle can be trapped at the center of the Bessel beam by means of an auxiliary Gaussian-like beam (*optical tweezer*) or by direct optical trapping with the Bessel beam itself. It is worth mentioning that very recently the longitudinal component of the electric field for the case of circularly polarized vortices with $\ell = \pm 1$ -which plays a fundamental role in the phenomenon discussed here- has been not only detected but used for laser ablation [29].

We would like to end this chapter by stressing the fact that we have unveiled a new type of light-matter interaction to obtain an enhanced chiral response. It makes use of light beams with OAM, where surprisingly the electric and magnetic fields do not present the usual form corresponding to circular polarized light. Notice that in the interaction of a molecule with the electric and magnetic fields, only the local fields at the position of the molecule are of interest. When the total optical chirality of the beam, integrated over the whole beam is also considered [30, 19], it yields the global unbalance of the two spin ($\sigma = \pm 1$) angular momentum components.

References

[1] K. H. Georg, "From chiral molecules to chiral phases: Comments on the chirality of liquid crystaline phases," Liquid Crystals **9**, 1–8 (1999).

[2] L. Barron, *Molecular light scattering and optical activity* (Cambridge University Press, 2004).

[3] P. W. Anderson, "More is different," Science **177**, 393–396 (1972).

[4] E. Francotte and W. Lindner, eds., *Chirality In Drug Resaerch* (Widley-VCH, 2006).

[5] E. Gorecka, M. Čepič, J. Mieczkowski, M. Nakata, H. Takezoe, and B. Žekš., "Enhanced chirality by adding achiral molecules into the chiral system," Phys. Rev . E **67**, 061704 (2003).

[6] M. Kuwata-Gonokami, N. Saito, Y. Ino, M. Kauranen, K. Jefimovs, T. Vallius, J. Turunen, and Y. Svirko, "Giant Optical Activity in Quasi-Two-Dimensional Planar Nanostructures," Phys. Rev . Lett. **95**, 227401 (2005).

[7] A. S. Schwanecke, A. Krasavin, D. Bagnall, and A. Potts, "Broken Time Reversal of Light Interaction with Planar Chiral Nanostructures," Phys. Rev . Lett. **91**, 247404 (2003).

[8] K. Hoki, L. González, and Y. Fujimura, "Control of molecular handedness using pump-dump laser pulses," J. Chem. Phys **116**, 2443 (2001).

[9] K. Hoki, L. González, , and Y. Fujimura, "Quantum control of molecular handedness in a randomly oriented racemic mixture using three polarization components of electric fields," J. Chem. Phys **116**, 8799 (2002).

[10] M. Shapiro and P. Brumer, "Coherent control of molecular dynamics," Rep. Prog. Phys. **66**, 859 (2003).

[11] P. Brumer, E. Frishman, and M. Shapiro, "Principles of electric-dipole allowed optical control of molecular chirality," Phys. Rev . A **65**, 015401 (2001).

[12] D. M. Lipkin, "Existence of a New Conservation Law in Electromagnetic Theory," Journal of Mathematical Physics **5**, 696 (1964).

[13] Y. Tang and A. E. Cohen, "Optical Chirality and its interactions with matter," Phys. Rev . Lett. **104**, 163901 (2010).

[14] Y. Tang and A. E. Cohen, "Enhanced enantioselectivity in excitation of chiral molecules by superchiral light," Science **332**, 333–336 (2011).

[15] N. Yang, T. Yiqiao, and A. E. Cohen, "Spectroscopy in sculpted fields," Nano Today **4**, 269–279 (2009).

[16] E. Hendry, T. Carpy, J. Johnston, M. Popland, R. V. Mikhaylovskiy, A. J. Lapthorn, S. M. Kelly, L. D. Barron, N. Gadegaard, and M. Kadodwala, "Ultrasensitive detection and characterization of biomolecules using superchiral fields," Nature nanotechnology **5**, 783–787 (2010).

[17] M. Babiker, C. R. Bennett, D. L. Andrews, and L. C. Dávila Romero, "Orbital angular momentum exchange in the interaction of twisted light with molecules," Phys. Rev . Lett. **89**, 143601 (2002).

[18] A. Alexandrescu, D. Cojoc, and E. Di Fabrizio, "Mechanism of angular momentum exchange between molecules and Laguerre-Gauss beams," Phys. Rev . Lett. **96**, 243001 (2006).

[19] D. L. Andrews, L. C. Dávila Romero, and M. Babiker, "On optical vortex interactions with chiral matter," Opt. Commun. **237**, 133–139 (2004).

[20] F. Araoka, T. Verbiest, K. Clays, and A. Persoons, "Interactions of twisted light with chiral molecules: An experimental investigation," Phys. Rev . A **71** (2005).

[21] W. Löffler, D. J. Broer, and J. P. Woerdman, "Circular dichroism of cholesteric polymers and the orbital angular momentum of light," Phys. Rev . A **83** (2011).

[22] K. Volke-Sepulveda, V. Garcés-Cháaves, S. Cháavez-Cerda, J. Arlt, and K. Dholakia, "Orbital angular momentum of a high-order Bessel light beam," Journal of Optics B: Quantum and semiclasical optics **4**, S82–S89 (2002).

[23] D. P. Craig and T. Thirunamachandran, *Molecular quantum electrodynamics* (Dover Publications Inc., 1984).

[24] N. Yang and A. E. Cohen, “Local geometry of electromagnetic fields and its role in molecular multipole transitions,” J. Phys. Chem. B **115** (2011).

[25] G. B. Arfken and H. J. Weber, *Mathemathical Methods for physicists* (Elsevier Academic Press, 2005), p. Pag. 676, sixth edition ed.

[26] C. Rosales-Guzmán, K. Volke-Sepulveda, and J. P. Torres, “Light with enhanced optical chirality,” Opt. Lett. **37**, 3486–3488 (2012).

[27] L. Novotny, M. R. Beversluis, K. S. Youngworth, and T. G. Brown, “Longitudinal field modes probed by single molecules,” Phys. Rev . Lett. **86**, 5251 (2001).

[28] G. Cipparrone, A. Mazulla, A. Pane, R. J. Hernandez, and R. Bartolino, “Chiral sefl-assembly solid microspheres: A novel multifunctional device,” Adv. Mater **237**, 7753 (2011).

[29] C. Hnatovsky, V. Shvedov, N. Shostka, A. Rode, and W. Krolikowski, “Polarization-dependent ablation of silicon using tightly focused femtosecond laser vortex pulses,” Opt. Lett. **37**, 226 (2012).

[30] K. Y. Bliokh and F. Nori, “Characterizing optical chrality,” Phys. Rev. A **83**, 021803 (2011).

7

Conclusions

The use of structured light beams offers the possibility to explore new applications where commonly used Gaussian light beams have encountered physical limitations. In this thesis we have explored some of the exotic properties of structured light beams in the search for new applications. In Chapter 2 we discussed about the Angular momentum of Light (AM). We started by rewriting Maxwell equations, from which we derived the Helmholtz equation and its paraxial approximation. Then we presented some of the solutions to the paraxial wave equation, Gaussian, Hermite-Gaussian, Laguerre-Gaussian and Bessel beams. The conditions for this type of solutions to carry angular momentum were also discussed in this chapter. We distinguished between two types of angular momentum, spin angular momentum (associated to the polarization of light) and orbital angular momentum (associated to its phase structure). In general these two forms of angular momentum cannot be separated, but within the paraxial approximation this separation becomes possible. Finally, at the end of this chapter, we reviewed the different techniques in which structured light beams can be generated. Cylindrical lens mode converters, spiral phase plates, holograms, q-plates and Spatial Light Modulators (SLMs) are among the most known techniques. The SLM is one of the most flexible, since it allows to switch on demand in an easy and prompt manner between different modes.

In Chapter 3 we delved into one of the most fascinating features of some structured light beams, the self-healing property. If we block part of the intensity profile of any beam, it is hard to believe that upon propagation this can be recovered. However, this property has been observed and studied in many beams, for example Bessel, Airy and Pearcy beams, among many others. This property is of great interest because it broadens the applications of structured light beams. For example, self-healing beams can be used in turbulent media. The dynamics involved in the self-healing process is still under study. It is believed that the energy flux plays a crucial role, since experimental observations demonstrates the energy flows from non-blocked parts of the beam towards blocked parts to reconstruct the beam's initial intensity profile. Along these line, we analyzed the Helico-Conical (HC) beam, unique in the sense that both its intensity and phase are helicoidal. HC beams are of special interest because they have promising applications in quantum optics and optical tweezers. Interestingly these beams feature also self-healing properties. We demonstrated this experimentally and reinforced our observations with theoretical simulations, which suggested that the energy flux is indeed responsible for the self-healing.

In Chapter 4 we introduced a novel technique to measure directly the transverse component of the velocity. In the context of laser remote sensing, the Doppler shift is widely used to measure the longitudinal component of the velocity. However, these systems do not allow us to measure the transverse component, at least not in a direct way. In order to measure this component, some techniques rely on the use of many lasers pointing at different directions, or systems capable to change very rapidly the direction of the laser beam. The method presented here comprises the use of structured light beams. The basic idea consist in illuminating the moving target with an appropriated structured phase. In this way, when small objects are illuminated with such beams, the light scattered back from them carries information about their velocity. This information can be extracted by interfering this beam with a reference one (that for simplicity can be a Gaussian beam). From this interference a beating signal is produced, whose Fourier transform can be used to determine the transverse velocity. In principle, we can employ any structured light beam to extract the transverse component of the velocity, however previous information about the motion could help us to chose a phase that best adapt to it. For example, for a rotational motion an azimuthal varying phase would greatly simplify the mathematics involved. In this chapter, we also presented a novel way to retrieve information about the direction of motion involving the use of dynamic structured phases. In essence, if we actively change the phase in the transverse plane in a controlled manner, the moving particle will produce a beating signal, whose frequency depends on both the modulation of the phase and the particle's velocity. For example, for a particle rotating clockwise, a helical phase rotating in the opposite direction would produce a beating signal with a higher frequency, compared to the case of a static helical phase. If they rotate in the same direction, the frequency will be lower. Hence, since we know the sense of rotation of the phase, the sense of rotation of the particle can be deduced by comparing the detected frequencies. The rotation of the phase can be performed with the same device used to create the structured beam. The technique presented in this chapter could be added to current existing Doppler systems to expand their capabilities. For example, one can envision a two laser system that measures at once both the longitudinal and the transverse components of velocity. This possibility was explored in the last section of this chapter, where we analyzed the helical motion. This movement can be decomposed into a translation along the direction of propagation of the beam and a rotation in the perpendicular plane. Experimentally, the use of an SLM allow us to switch very rapidly from a Gaussian to a Laguerre-Gaussian beam. In this way, with the Gaussian beam we extract the longitudinal component and with the Laguerre-Gaussian beam the transversal component, this is we were able to characterize the full 3D movement.

In Chapter 5 we presented another application related to high resolution optical metrology. For this, two ingredients were essential: the concept of mode projection and and the use of common path interferometers, more precisely, a self-referencing type. In this technique, both reference and signal beams are generated locally, hence the two beams experience common aberrations and path-length changes, maintaining their relative phase constant. This concept is the basis of compact disc technology, in which, information is encoded in a series of tracks of pits recessed from a surfaced called the land. Compact disks are operated by positioning the land h= 1/4 of the wavelength higher than the pit. In this way, when a compact disk is illuminated with a laser beam of appropriated dimensions, half of the beam straddles the land (reference) and half straddles the pit (signal). A phase difference of $\pi/2$ is produced between both beams producing a characteristic interference pattern which is read out in the far field. In this case the system is insensitive to small phase changes. For example, the addition of thick layers on top of the land will produce an almost unnoticeable effect. However, at the quadrature condition, when both the reference and the signal beams are $\pi/4$ out of phase, this system becomes highly sensitive to small phase differences. In order to met this requirement, the land should be $\lambda/8$ higher than the pit. This restriction is the basis for the Bio-compact disk technology, in which biological information is stored into specially designed compact disks. These are made by evaporating radial lines of gold (similar to a spoke) into a wafer compact disk. Bio-layers of molecules are placed on top of such gold ridges for their analysis. In this way, the quadrature condition establishes the ideal framework under which CPI is highly sensitive to small phase changes. Hence, in order to measure the height of thin layer one would have to first construct a ridge of height h= $\lambda/8$ on top of which we should place the layer to be measured. The dependence of the optimal value for h on the wavelength is a significant drawback, since we need a specially designed ridge for each wavelength. In this chapter we explored a way to overcome this. The main idea is to impose the quadrature condition to the light reflected from the sample rather than using a ridge. In this way, the sample does not need to be placed on top of a specifically engineered surface only on a plane reflective surface.

Finally, in chapter 6 we investigated the use of OAM to enhance the chiral response of chiral molecules. The word chirality is used to refer to objects whose image mirror cannot be superimposed with itself by rotations and translations alone. A pair of such molecules are called enantiomers. Chirality is of great interest because it plays a crucial role in life, since, for example, aminoacids and sugars (some of the building blocks of molecules) come in left- or right-handed varieties. It is relevant the fact that human bodies make aminoacids and sugars using only the left-handed enantiomers, the right-handed being ignored by our cells. This specificity is of great interest in the drug industry since two enantiomers can have very different physiological effects. Enantiomers are identical in most regards and it is only in their interaction with other chiral objects that they become distinguishable. Here, Circularly Polarized Light (CPL) has played a crucial role since chiral molecules distinguish left handed from right handed polarized light by absorbing them at different rates, a phenomenon knows as circular dichroism. However, most molecules are small compared to the wavelength of light. Therefore, the different rates of absorption of a chiral molecule are generally small, making its detection rather difficult in some cases. Several efforts to enhance the chiral response of molecules have been made, for example by inserting an achiral molecule in a chiral system or by using planar chiral nanostructures. Contributions also from nonlinear spectroscopy and coherent control have been also reported. Perhaps one of the most interesting is based on the use of the Optical Chirality (OC), a pseudoscalar quantity that captures the degree to which the electric and magnetic fields wrap around a helical axis at each point in space and is an intrinsic property of chiral fields. It has been shown that, by properly engineering chiral fields, it is possible to enhance several times the chiral response of enantiomers. In this first approach, the chiral field consisted in the superposition of two counter-propagating waves, in such a way the molecules located at the nodes of the chiral field showed an enhanced chiral response. In this context, we explored theoretically the role of twisted beams in circular dichroism. Previous theoretical investigations on the interaction of beams with OAM and molecules have yielded seemingly contradictory results within the paraxial approximation. Hence, we abandoned this approximation and considered exact solutions to the Maxwell equation's, more precisely high-order Bessel beams endowed with OAM. This approach allowed us to unveil some important features not easily shown in the paraxial framework. First we observed that, similar to CPL, these beams with nonzero value of chirality induce a chiral response, on chiral molecules located at the center of the beam. We also observed that the structure of the electric and magnetic fields, which bear optical chirality, is radically different from the usual form of CPL. The fields at the center of the beam contain a single component of the field (along the direction of propagation), while in the case of CPL there are two orthogonal components perpendicular to the direction of propagation. A $\pi/2$ phase difference between the electric and magnetic fields, which is typical of CPL, is responsible for the nonzero value of the chirality. An enhancement on this chiral response can be done by a coaxial superposition of two high-order Bessel beams with opposite winding number $\ell = \pm 1$ and slightly different intensities. The experimental detection of this chiral response could be observed by using as probe a single molecule with a fixed absorption dipole moment parallel to the beam axis or a chiral solid microsphere located at the center of the beam. The probe particle can be trapped at the center of the Bessel beam by means of an auxiliary Gaussian-like beam (*optical tweezer*) or by direct optical trapping with the Bessel beam itself.

In this thesis we put forward novel techniques that expands the range of applications of structured light. We explored fields as diverse as optical metrology, remote sensing and molecular chirality. We also did significant contributions to fundamental aspects of light by showing experimentally that Helico-Conical beams features self-healing properties.

List of publications

This thesis is based on the following publications:

- **C. Rosales-Guzmán**, K. Volke-Sepulveda, and J. P. Torres, “Light with enhanced optical chirality," Opt. Lett. **37**, 3486-3488 (2012).
- N. Hermosa, **C. Rosales-Guzmán**, and J. P. Torres, “Helico-conical optical beams self-heal,” Opt. Lett. **3**, 383-385 (2013).
- **C. Rosales-Guzmán**, N. Hermosa, A. Belmonte, and J. P. Torres, “Experimental detection of transverse particle movement with structured light,” Sci. Rep. **36**, 2815 (2013).
- **C. Rosales-Guzmán**, N. Hermosa, A. Belmonte, and J. P. Torres, “Direction-sensitive transverse velocity measurement by phase-modulated structured light beams,” Opt. Lett. **18**, 5415-5418 (2014).
- **C. Rosales-Guzmán**, N. Hermosa, A. Belmonte, and J. P. Torres, “Measuring the translational and rotational velocities of particles in helical motion using structured light,” Opt. Express **22**, 16504-16509 (2014).
- N. Hermosa, **C. Rosales-Guzmán**, S. F. Pereira, and J. P. Torres, “Nanostep height measurement via spatial mode projection", Opt. Lett. **39**, 299-302 (2014).